Lise Fagnan

Evaluation and Quantification of the Impact of Soaking on the Mechanical Properties of KNN

Master thesis in Materials Technology
Supervisor: Prof. Julia Glaum
Co-supervisor: Caitlin Guzzo

June 2022

Master's thesis

2022

Lise Fagnan

Master's thesis

NTNU
Norwegian University of
Science and Technology
Faculty of Natural Sciences
Department of Materials Science and Engineering

◼ NTNU
Norwegian University of
Science and Technology

NTNU
**Norwegian University of
Science and Technology**

Evaluation and Quantification of the Impact of Soaking on the Mechanical Properties of KNN

Lise Fagnan

ABSTRACT

This thesis aims to evaluate the effect of soaking on the mechanical properties of $K_{1-x}Na_xNbO_3$ (KNN) to contribute to the general effort of improving KNN-based implants in bone replacement.

The samples were processed by solid-state synthesis using K_2CO_3, Na_2CO_3 and Nb_2O_5 as precursors. Calcination and sintering were performed at respectively 825°C and 1125°C. The resulting samples were pellets of stoichiometric KNN presenting an average 93.6% relative density. Secondary phases composed of layered tungsten-bronze type $K_4Nb_6O_{17}$ and tungsten-bronze type $K_2Nb_4O_{11}$ were reported. A 12-hour soaking took place in three liquids: ultra-pure water, deionized water and saline solution. The saline solution was also used to perform 6-hour, 24-hour and 72-hour soakings. The mechanical properties were evaluated with nanoindentation using 8000 μN maximum load and microindentation using a Vickers hardness test. The hardness before soaking was 12.28 GPa on average with the nanoindentation and 3.48 GPa on average for the Vickers hardness. The chemical properties were evaluated using Raman spectroscopy, X-Ray Diffraction, Grazing Incident X-Ray Diffraction and Scanning Electron Microscopy with Energy Dispersive X-Ray Spectroscopy.

Independently of the soaking conditions, the soaking resulted in a release of potassium into the solution and in a decrease in hardness of several orders of magnitude in the secondary phases. An uneven Nb-rich crust formed on samples presenting secondary phases and on samples soaked for 6h in saline solution. The Vickers hardness presented variations in the results: increases and decreases that were a function of the amount of secondary phases and not of the soaking conditions. The hygroscopicity of the secondary phases was highlighted and explained. It was concluded that, based on the absence of hygroscopic behavior in the stoichiometric KNN, samples without secondary phases are able to sustain soaking up to 72h in saline solution.

SAMMENDRAG

Denne masteroppgaven har som mål å evaluere effekten av væske på de mekaniske egenskapene til $K_{1-x}Na_xNbO_3$ (KNN) for å bidra til utviklingen av bedre KNN baserte ortopediske implantater.

Prøvene ble prosessert gjennom konvensjonell faststoff syntese med K_2CO_3, Na_2CO_3 og Nb_2O_5 som utgangsstoff. Kalsinering og sintring ble gjennomført på henholdsvis 825°C og 1125°C, som resulterte i støkiometriske KNN pelleter men 93.6% relativ tetthet. Sekundærfaser i pelletene oppstod i form av wolfram-bronse struktur med enten komposisjonen $K_4Nb_6O_{17}$ eller $K_2Nb_4O_{11}$. Prøver ble lagt i tre forskjellige væsker over en tolvtimers periode, væskene var utrarent vann, deionisert vann og saltløsning. Saltløsningen ble valgt til å utføre ytterligere forsøk hvor prøvene var i kontakt med løsningen over en periode på 6, 24 og 72 timer. Mekaniske egenskaper ble evaluert ved bruk av nanofordypning med 8000 μm maksimum belastning og mikrofordypning i samspill med en Vickers hardhetstest. Hardheten før kontakt med væske var i gjennomsnitt 12.28GPa for nanofordypning og 3.48 GPa for Vickers hardhet. Kjemiske egenskaper ble etterforsket gjennom Raman spektroskopi, røntgen diffraksjon, «Grazing Incident» rønten diffraksjon, skannende elektronmikroskopi og «Energy Dispersive» røntgen spektroskopi.

Kontakt med væske resulterte i frigjøring av kalium fra prøvene til væsken uavhengig av typen væske og kontakttid, dette medførte også en sterk reduksjon i hardhet for sekundærfasene. En ujevn niob-rik skorpe oppstod på prøver som innehold sekundærfaser og på prøver som hadde vært i saltløsning i seks timer. Vickers hardhetsmålingene var variable, med økning eller reduksjon i hardhet som et resultat av mengden sekundærfase. Mekanismen bak denne effekten foreslås å være delvis basert på introduksjonen av sprekker/defekter fra volumendringer i sekundærfasene når de kommer i kontakt med væske da de er hygroskopiske. Hardheten var uavhengig av hvor lenge prøvene var i kontakt med væske over seks timer. Det konkluderes at støkiometrisk KNN uten hygroskopiske sekundærfaser tåler forlenget kontakt med væske opptil 72 timer uten signifikante reduksjoner i mekaniske egenskaper.

PREFACE

This thesis is written in the context of the course *TMT4920 - Materials Technology, Master's thesis* at the Norwegian University of Science and Technology. It concludes the five years program of Biomedical Engineering at the University of Liège. This work was supervised by Prof. Julia Glaum.

The experimental work was conducted from January to June 2022 in the Department of Materials Science and Engineering by the author. An exception is the EDX measurement, performed under the supervision of Caitlin Guzzo.

Trondheim, June 9, 2022

Lise Fagnan

ACKNOWLEDGEMENTS

My deepest gratitude goes to Prof. Julia GLAUM for her precious guidance, advice and feedbacks during the past months and for the opportunity to work on an exciting subject. I would like to express sincere thanks to PhD candidate Caitlin GUZZO for answering each and every one of my questions, no matter the time, for her patience in the lab and for her help in all the steps of my project.

I'm also grateful to the Functional biomed group and the FACET group for their interesting interventions during the weekly meetings and notably to Marcus BENTZEN for translating the abstract into Norwegian. Thank you to the technical staff of the *K-II* building for their training. I wish to acknowledge the University of Liège (Belgium) who gave me, during five years, the keys to conduct this master thesis and for offering me the chance to be part of NTNU for one semester.

Even with the distance in between us, I felt the support of my family, this was of great help, *Merci !* Thanks should also go to Pauline and Catherine and their encouragement along my studies and this thesis. A special thanks goes to Joachim for his proof-reading and especially his endless support.

CONTENTS

LIST OF FIGURES

LIST OF TABLES

CHAPTER

$$1$$

INTRODUCTION

This chapter introduces the topic of bone implants and presents a brief history of piezoelectric materials for biomedical applications. The aims of this work are given and justified. Ultimately the structure of the different chapters is shown.

1.1 Background and motivation

Different reasons may lead to the need of bone implants. It can be due to accidents, malformations or diseases. A common cause is osteoporosis where bone density decreases and induces a weakening of bones. Bone cancer, spine fracture, hip replacement, dental surgery, all of these medical interventions require bone implants. The orthopedic implants market is in constant growth and is expected to keep this trend in the following years mainly because of the ageing of the population and lifestyle-related concerns [73].

Earliest traces of bone implants go back to Hindu, Egyptian, and Greek civilizations. Over the years, different techniques were developed. One of the first is the implantation of mineral salts of calcium and potassium which can be traced back to the late 19th century with the goal to improve bone regeneration. Later, in 1963, a first bioceramic composed of aluminate ceramic and epoxy resin was developed to act as bone substitute and revealed a strong attachment to the surrounding bones. As the technology improved, more materials, with more complex and active interactions with bones could be tested [84], with for example: $CaO \cdot Al_2O_3$ and $CaO \cdot TiO_2$, etc.

All these attempts share one common goal: to mimic the human body's functioning, or at least to get as close as possible to its original properties. In bone replacement, ceramics are often used and serve as load bearing materials. As they present a high hardness and low friction coefficient, they avoid the abrasion of the material which could lead to inflammation.

Bones are active organs: throughout their lives they grow, regenerate and heal. Since the 1960s, it is known that bones present piezoelectric properties, and since then this piezoelectricity is believed to be an important factor in their regeneration by activating cells that regulate their behavior. Piezoelectric materials are therefore preferred for implants. A third parameter is of importance for implants: biocompatibility. A biocompatible material can be defined as a material that doesn't produce any immunological, inflammatory or allergic response, or any other undesirable reaction when in contact with the body [19]. These three requirements (ceramic, piezoelectricity and biocompatibility) lead to several options: $Na_{0.5}BiO_{0.5}TiO_3$, $BaTiO_3$ and $K_{0.5}Na_{0.5}NbO_3$ are examples. A final prerequisite for implants is their long-term reliability. A surgical operation, with all that it implies in terms of resources and rehabilitation, is required for the implantation. The material therefore has to be reliable, with stable properties in time to avoid another operation, or to, at least, postpone it as late as possible.

In early research, KNN, the abbreviation of $K_{0.5}Na_{0.5}NbO_3$, showed attractive results thanks to its high Curie temperature, structure and biocompatibility [82] but exhibited poor piezoelectric properties. It is in 2004, when a study on KNN reported a high piezoelectric coefficient of 416 pC/N, this material became extensively studied [66]. One of the drawbacks of KNN was its porosity, but in bone replacement porosity is an advantage as it gives bone some space for tissue integration.

The community generally agrees that KNN will not replace PZT, a widely used piezoceramic, because the KNN ceramic will not reach as good piezoelectric properties as the lead-based compound. Nevertheless, in the biomedical world, prominent piezoelectric properties are not needed as the voltages required to activate cells are low. This makes KNN a promising candidate for this type of application.

1.2 Aim of this work

This work aims to contribute to the general effort of developing KNN-based materials for biomedical applications by evaluating their long-term reliability. It focuses on the evolution of the mechanical properties of the ceramic during soaking in different liquids, starting with a simple solution (ultra-pure water) and then increasing the chemical complexity to approach the composition of the liquid present in the body (saline solution).

Different characterization techniques were followed to qualify and quantify the changes in the mechanical and chemical properties of stoichiometric solid-bulk KNN during soaking in ultra-pure water, deionized water and saline solution for 12h and in saline solution for different periods of time: 6h, 24h and 72h. The samples were obtained through solid-state synthesis before being soaked and charac-

terized. As stated earlier, hardness is an important factor in ceramic implants. Its evolution was measured through nanoindentation and microindentation to obtain information on both the bulk and the surface of the samples. X-ray diffraction was used to appraise changes in crystalline structure of the samples and was also performed both on the bulk and the surface. Raman spectroscopy allowed to investigate the chemical structure. Finally, scanning electron microscopy and energy-dispersive X-ray spectroscopy were used to explore the chemical composition and appearance of the samples.

1.3   Structure

The present thesis is structured as follows. Chapter 2 provides a description of bones by highlighting their relevant properties with respect to this work and state of the art on KNN. Chapter 3 describes in detail the methodology applied and introduces the different characterization techniques used. Chapter 4 presents the raw results obtained. Chapter 5 discusses the results and compares them. Finally, Chapter 6 summarizes and concludes the work.

CHAPTER

2

LITERATURE REVIEW

This chapter intends to provide the reader with state of the art concerning KNN for biomedical applications. As this work is part of the general effort to make KNN-based bone implants, it starts with an introduction on bones, their composition and noteworthy properties. It is then followed by the presentation of KNN and an explanation of why this material is a suitable candidate for bone replacement. A summary of the most recent studies on KNN is also provided.

2.1 Bones

Bones are part of the human skeleton, among cartilages, tendons and ligaments. Their purpose is mainly to endure loads without undergoing extensive deformation to either be a shield for other organs or a load bearer for the whole body [12, 79].

Bones appear in various sizes and shapes with variation in composition depending on their location in the body and the function they intend to fulfill. This variability is related to their ability to adapt. Indeed, the biology of a bone i.e. the composition and structure, is shaped by its mechanical demand [80, 35].

2.1.1 Structure and composition

Bones possess a complex structure, summarized in Figure 2.1. At different scales, bones present composite material reinforced with fiber [80].

On the macroscale, bones fall into two categories: spongy or compact. The difference between these two types of bone lies in the density. Compact bones, as their name suggests, have a higher density with only 5-10% porosity whereas spongy bones present a porosity of 75-95% [80]. In this blending, the strength-to-mass

ratio is optimized [35].
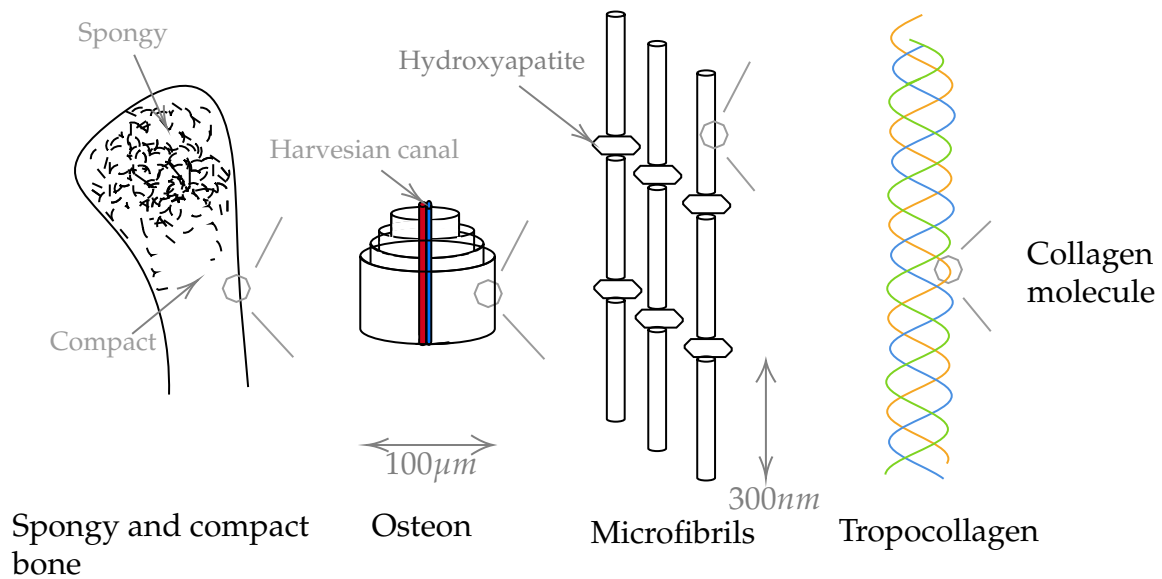
Figure 2.1: Bone structure at different scales. Adapted from [21].

The microstructure is composed of osteons. These Harvesian systems, named after the Harvesian canal containing blood vessels and nerves in the center, are part of the structural unit of bones [92].

Continuing zooming into the structure of bones, arrives the nanoscale. The bone matrix has both organic and inorganic components. The organic part is mainly made of collagen. These proteins form tropocollagen that aggregate into fibrils. This aggregation follows a precise structure and presents gap regions every 67 nm that are filled by hydroxyapatite. Hydroxyapatite is associated to the inorganic crystalline part of the matrix that serves two main functions: providing stiffness and being a warehouse of ions for the body [92, 35].

Hydroxyapatite is a major constituent of bones as it accounts for 65% of the elemental composition of bones. Its chemical formula is $Ca_{10}(OH)_2(PO_4)_6$. It is present both around the collagen fibrils and inside. This inorganic ceramic presents a hexagonal structure [83, 35].

2.1.2 The bone as an active organ

The human skeleton undergoes small as well as big changes on a continuous basis, and for different purposes. Bone remodeling is a process in which the bone is renewed. The human body replaces old bones by new ones to avoid accumulation of microcracks, to adjust to the mechanical stress it undergoes [38, 35] or to control the concentration in minerals [100]. This process highly depends on the

type of bone and the turnover may vary from 4 to 33.7% each year [38, 100]. This process can be simplified by the three main steps shown in Figure 2.2:

- *Resorption*: the activated osteoclast are linked to the bone surface,

- *Reversal*: cells occupy the site,

- *Formation*: osteoblast are enrolled to synthesize the bone matrix that will later be mineralized [38, 100].
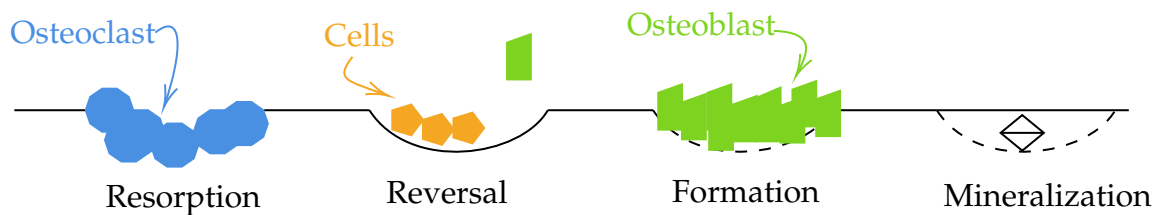
Figure 2.2: Main steps of bone remodeling. Adapted from [11].

Due to their function, osteoblasts can be called bone resorption cells and osteoclasts bone formation cells [39].

2.1.3 Piezoelectric behavior

Before presenting the piezoelectric properties of natural tissue such as bones, let's start with a definition of piezoeletricity and a commentary on its functioning.
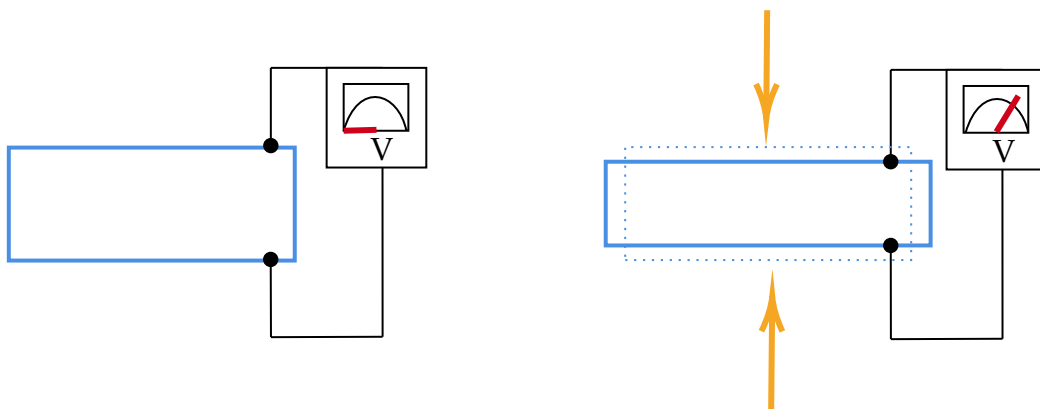
Figure 2.3: Piezoelectric effect. Adapted from [93].

The piezoelectric effect, depicted in Figure 2.3, relies on the capability of given crystalline materials to engender voltage as a response to mechanical stress. This

reversible effect, discovered in 1880, can be explained by the distribution of charge inside the material. When the crystal does not undergo mechanical stress or electrical stimulation, the positive and negative charges balance themselves. This is also the case for non-piezoelectric materials. As exhibited in Figure 2.4, when a piezeoelectric material is compressed, the charges will glide and move their center, which eventually creates a dipole [88]. This effect can be quantified with the piezoelectric coefficient, d_{33}, expressed in Coulomb per Newton, [C/N]. PZT, known for its superior piezoelectric properties, has a piezoelectric coefficient around 600 pC/N [74].
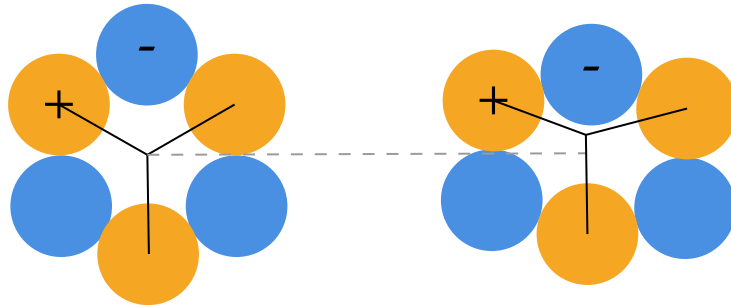
Figure 2.4: Creation of a dipole in a piezoelectric crystal. Adapted from [93].

The materials able to exhibit a piezoelectric effect have to be dielectric. This translates to being a poor conductor with an efficient preservation of electrostatic field and therefore a material able to store energy by an electrostatic field [22]. As illustrated in Figure 2.5 some piezoelectric materials have other significant properties. Pyroelectric materials exhibit spontaneous polarization. The smallest category includes the ferroelectric: their dipole orientation can be re-oriented in space, which gives rise to a hysteric behavior of polarization and strain.
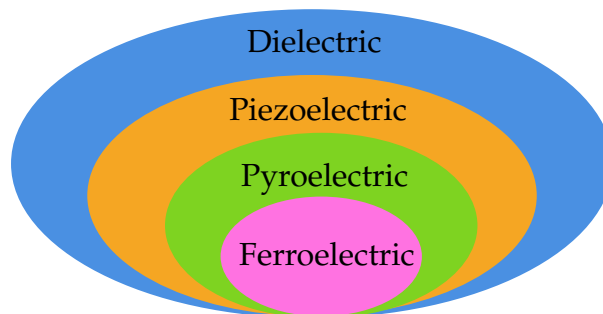
Figure 2.5: Relationship between dielectric, piezoelectric, pyroelectric and ferroelectric materials.

The piezoelectric behavior of bone was first characterized in the mid-fifties by highlighting a linear correlation between stress and polarization and between

electric field and strain [32]. Shamos et al. stated that, in order to exhibit piezo-electric behavior, living tissue needed *"the presence of a well ordered asymmetric fibrous molecule, cross-linked to form a uniaxial system which can be polarized by a shearing stress."* [78]. As stated earlier, collagen in bone in arranged in oriented fibrils, which explains why collagen is the origin of the piezoelectric behavior of bones. Other tissues indicate presence of piezoelectric effect, wood for example with its cellulose [78, 45].

Still today, the role of the piezeoelectricity of bones is subject to debate. It is believed to impact the regulation of several metabolic activities such as bone re-modeling, growth, fracture healing, but to also influence cell metabolism by im-pacting proliferation, differentiation, motility along with others [49]. Indeed, in this theory, a compression (or tension) will create a dipole as shown in Figure 2.4, that will result in a more electronegative or electropositive surface. Osteoclasts are activated in positively polarized regions whereas osteoblasts are activated in negatively polarized regions [39]. When walking for example, the bones will be sometimes compressed, sometimes stretched. Hence some piezoelectric potential is generated and will help the self-renewal activity of bones. This phenomenon can be highlighted on astronauts after a long period of weightlessness. A loss of bone mass can be observed and is linked to the absence of stimulation. The fracture site of a bone will also become more electronegatively charged, which as mentioned above activates the bone forming cells [39].

Orders of magnitude are a must when presenting a behavior. In the case of piezo-electricity in bones some numbers can be given. The piezoelectric response in a human tibia when walking is around 300 μV [45]. The piezoelectric strain coeffi-cient of human bone is of around 7.5 to 9 pC/N [49].

This previous section can be summarized by the fact that piezoelectricity is a sig-nificant property of bones for healing and remodeling. Some studies suggested that, in the case of impaired tissues, piezoelectric scaffolds lead to a faster recon-struction of the tissue [49, 96]. Hence, both for biomimicry and utility reasons, piezoelectric materials should be investigated for implants.

2.2 KNN

2.2.1 Crystallographic structure

Potassium sodium niobate, whose stoichiometric form is $K_{0.5}Na_{0.5}NbO_3$, is com-monly called KNN. This ceramic is composed of a crystalline structure called perovskite. A perovskite has a general formula of ABX_3 in which A and B are cations and X anions. For KNN, A sites are occupied by K^+ or Na^+, B sites by Nb^{5+} and finally X sites by O^{2-} as shown in Figure 2.6. The crystalline lattice is

composed of $KNbO_3$ and $NaNbO_3$ with a molar ratio of 1:1 [18].
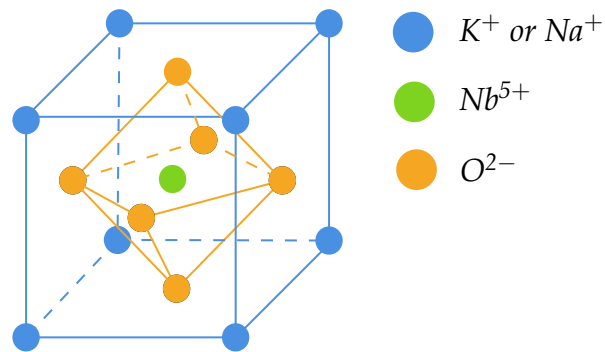
Figure 2.6: Perovskite structure of KNN. Adapted from [18].

Perovskite are highly represented in solid-state chemistry because of their flexibility. Indeed, these structures are able to sustain distortions and structural deformations. A substantial amount of ions can assemble into this perovskite structure [6].

The crystallographic plane occupied by KNN can be investigated by X-ray diffraction. A typical pattern for KNN is shown in Figure 2.7. One peak corresponds to a crystal plane. Crystal planes are defined by the Miller indices. These three numbers aim to indicate the orientation of a plane of atoms [25]. An example is shown in Figure 2.8.
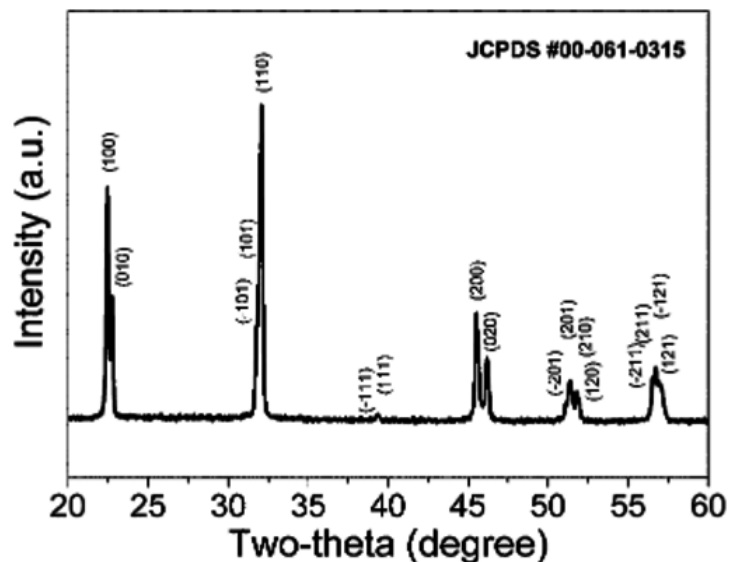
Figure 2.7: XRD pattern of the $K_{0.5}Na_{0.5}NbO_3$ powders calcined at 850°C for 2h. Monophasic KNN powders were obtained [23].
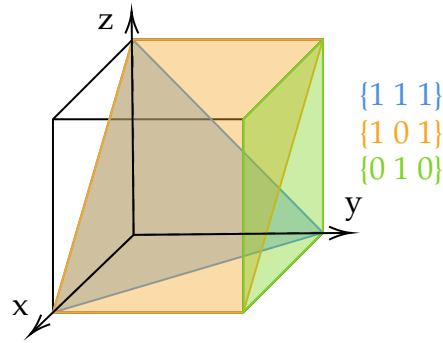
Figure 2.8: Example of crystallographic planes and corresponding Miller indices.

As just mentioned, in the perovskite structure of KNN, a NbO_6^- octahedra is present. This structure can be highlighted by Raman spectroscopy as it is responsible for the main vibration [68]. Typical spectra for KNN are shown in Figure 2.9. The peak positions v_5, v_1 and $v_1 + v_5$ are located at a wavenumber of respectively 255, 611 and 858 cm^{-1} [27]. The active mode v_1 corresponds to a stretching of the NbO_6 octahedra while the v_5 corresponds to a bending of this same octahedra [27]. At the shoulder of v_1, another active mode can be found, v_2, and corresponds to the stretching of NbO_6^-.
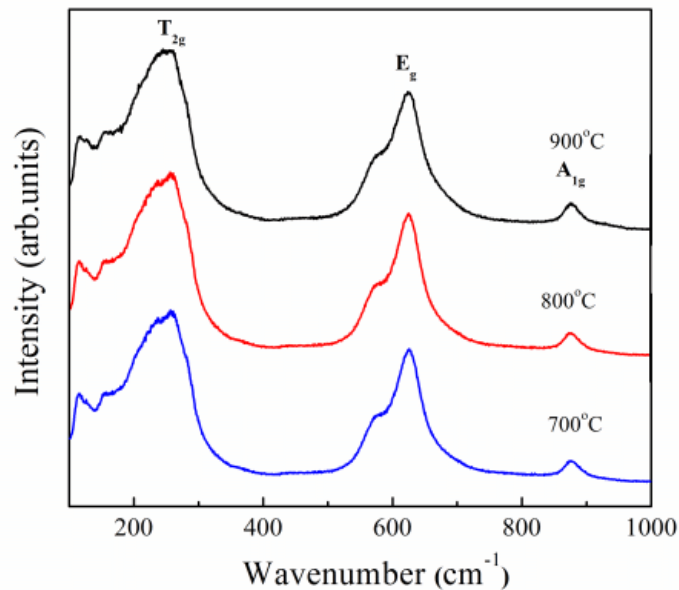
Figure 2.9: Raman spectra for the KNN ceramics calcined at different temperatures and sintered at 1000°C for 5 hours [64].

The relative density of bulk ceramic samples of KNN is provided to be around 94% [96]. However this value can vary according to the processing method.

2.2.2 Phase diagram

KNN exhibits polymorphic phase boundaries, i.e. regions where structural phase transitions are temperature-driven. An increase of temperature for KNN will modify the structure as indicated in Figure 2.10: at low temperature the structure is rhombohedral, meaning that the three axes of the crystals have an equal length but are not perpendicular to one another. Near 100°C, this structure becomes orthorhombic: the three axes have unequal length but are perpendicular to one another. Around 200°C the material undergoes a transition to tetragonal structure, in which two out of the three axes have an equal length. Near the Curie temperature of KNN, the ceramic undergoes a cubic transition [81] and all three axes have the same length and are perpendicular. The Curie temperature is a parameter often highlighted in the literature as it represents the temperature at which the modification of the structure of the material is such as it loses its piezoelectric properties. Values may vary according to the literature: 217-307°C [42], 410°C [81], 418°C [14, 65].
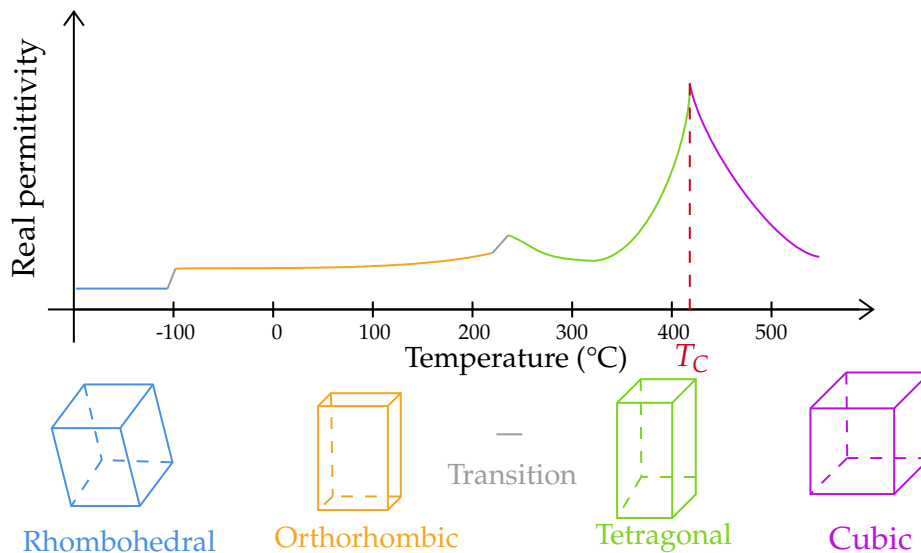
Figure 2.10: Schematic representation of temperature dependence of real permittivity on unmodified KNN. Adapted from [33, 26].

2.2.3 Piezoelectric behavior

In undoped and stoichiometric KNN, the piezoelectric coefficient d_{33} is bounded between 78 and 98 pC/N [42], some studies reported a slightly lower coefficient of 43 ± 28 pC/N [74]. Other studies reported higher values (up to 300 or 400 pC/N) by improving KNN [99]. These values, considered to be too low for a multitude of applications, are surpassing the value of human bones by at least

one order of magnitude.

The dielectric behavior can be quantified with polarization hysteresis loops. These hysteresis loops are visible when plotting the polarization as a function of the electric field. The piezoelectric behavior is quantified by plotting the strain as a function of the electric field. Typical graphs are exhibited in Figure 2.11.
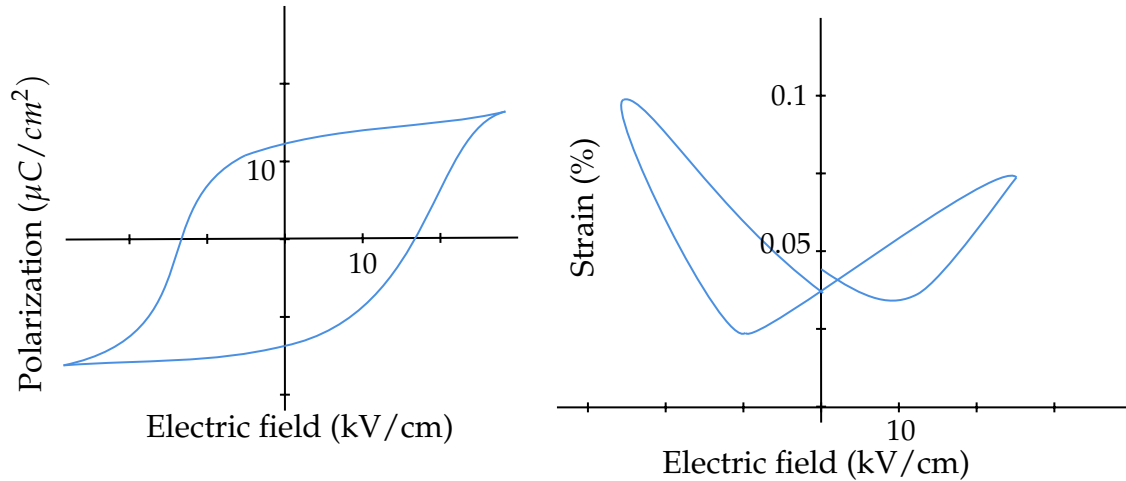
Figure 2.11: Typical P-E hysteresis loops for KNN at 10 Hz and typical bipolar strain curves. Adapted from [97].

The piezoelectric response is influenced by the crystallographic structure. The presence of the phase boundaries, presented in Figure 2.10, increases the piezo-electric response as they contain phases with different polarization orientations [33]. The polarization rotation was determined to be an important factor in the piezoelectric properties and to be linked with the lattice strain [56, 29].

The drawback is that the piezoelectric properties of KNN are temperature-dependent [33]. This is not an issue for biomedical applications where temperature is stable over time.

A noteworthy improvement for piezoelectric properties of KNN is the stabilization of the rhombohedral–tetragonal phase boundary. This deviates the transitions rhombohedral–orthorhombic and orthorhombic–tetragonal to be around room temperature [33].

2.2.4 Biocompatibility

When keeping in mind the final application of KNN, an important question to be raised is the one of biocompatibility. As stated in the introduction (section

1.1), a biocompatible material is a material that doesn't produce any undesirable reaction when in contact with the body. Several parameters can influence the biocompatibility of a material with a given surface: the composition of the implant, its structural properties, the presence of toxins or blood, the properties of the implanted surface, etc. [19].

A way to quantify biocompatibility is by calculating the cell viability, this means the percentage of cells that survived after being in contact with the implant. This is done by measuring the cell density of the sample and dividing it by the cell density of the negative control:

$$\text{Cell viability} = \frac{\text{Mean cell density of sample}}{\text{Mean cell density of negative control}} \cdot 100\%. \qquad (2.1)$$

The negative control is the sample containing cells but not the implant to be able to account for unexplored variables.

The cytotoxicity of KNN was calculated notably in 2012 by incubating cells with a solution in which powder KNN (made by solid-state synthesis) was soaked. The results showed a low cytotoxicity with a cell viability of 84% [96]. The cell viability of human lung carcinoma cell line was shown to not be impacted by the presence of KNN powder [42]. This endorses the relevance of KNN in biomedical applications. A patent was even attributed to KNN ($Na_xK_yNbO_3$, wherein $0 \leq x \leq 0.8$, $0.2 \leq y \leq 1$, and $x + y = 1$ more specifically) in 2003 as biocompatible material for implants [61].

2.2.5 Processing

One of the first characteristics standing out when working on KNN-based systems is their poor reproductability. Indeed, the processing can be influenced by many factors that may lead to a low density as well as the presence of secondary phases [7].

Solid-state synthesis

A common processing route is the solid-state synthesis. This low-priced and straightforward method, also called the ceramic method, consists in mixing solid materials and achieving a chemical reaction leading to the formation of a new solid:

$$K_2CO_{3(s)} + Na_2CO_{3(s)} + 2\,Nb_2O_{5(s)} \longrightarrow 4\,K_{0.5}Na_{0.5}NbO_{3(s)} + 2\,CO_{2(g)} \qquad (2.2)$$
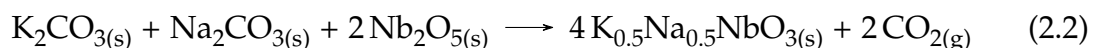
The reaction is induced by the heating of the material under the melting point [87]. The sintering builds upon three steps during which the pores change and

the material is solidified. This process is driven by diffusion [10] and reduction of the surface free energy [7, 10]:

- *Initial stage.* During this stage diffusion will occur from high chemical potential regions (the contact region) to low chemical potential regions. These potential differences can be explained by the difference in the curvature, convex or concave. Two transformations will occur: densification resulting from grain boundary diffusion and coarsening resulting from surface diffusion, evaporation from the surface and condensation in the neck region. This stage is illustrated in Figure 2.12.

- *Intermediate stage.* The densification is accelerating and tubular pores, lying on the particles junctions, will shrink. This will lead to the determination of the closed porosity.

- *Final stage.* The tubular pores being to shrink, they become unstable and break to leave only isolated pores at the grain boundaries [10]. These pores can generate two behaviors: disappear from shrinking more or grow from merging.
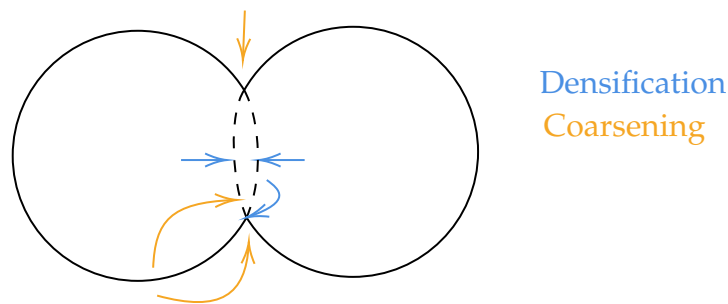
Figure 2.12: Schematic of the initial stage of sintering. Adapted from [10].

Pore entrapment may occur if pores are trapped inside a grain. This can not be reversed and is the result of a too rapid sintering because of abnormal grain growth. A normal grain growth is a growth in which *"the average grain size of the material increases continuously and without changes in the grain-size distribution"* [7] according the definition of Malič et al.

For KNN specifically, some adversities need to be taken into account. The main issue is the emergence of secondary phases during the sintering and the calcination due to alkali losses [42, 96]. Na_2O and K_2O volatilize because of their high vapor pressure [96, 51]. Finding the optimal sintering temperature is therefore the subject of many studies [36, 63]. The precursors tend to react with the humidity present in the air. Therefore they need to be dried before being used and to be kept dry. Indeed, when weighing them, they can humidify again and lead to a

imprecise value and therefore a wrong stoichiometry. Small variations in the stoichiometry can cause the appearance of secondary phases. For example $KNbO_3$ is stable but with a small excess in potassium leads to hygroscopic phases [51]. Hygroscopicity defines the behavior of a material to absorb water, it can lead to a swelling of the material and to some modified properties [40]. The precursors commonly used in the solid-state synthesis are the carbonates (K_2CO_3 and Na_2CO_3) and these alkalines present a high hygroscopicity [51].

Sustainability

On sustainability, even if KNN is lead-free and presented as *environmental-friendly* in a large amount of papers, it was shown, through a life cycle assessment, to be more hazardous to the environment than PZT, in the early stage of life at least.

This is mainly due to the mining of Nb_2O_5, one of the precursors. This mining leads to discharges such as arsenic or nitrates that can impact aquatic life. It may also severely cause a loss of biodiversity and impact air quality. Solutions exist to reduce their impact on the environment but their economical cost often prevents them from being applied [42, 43].

Alternative processes

Alternatives to the solid-state synthesis have been proposed such as hydrothermal reaction [65]. The authors reported non-stoichiometric KNN with potassium excess after 6h of reaction. The grains were dodecahedra-shaped after 3h and the characteristic cubic shape of KNN started to appear after 6h, to finish after 12h with irregularly shaped aggregates of cubic grains. The main advantage of this technique is the possibility to apply moderate temperature and therefore limit the volatilization of the different compounds. However the difficulty to obtain stoichiometric KNN was highlighted. Moreover, this method requires expensive autoclaves [75].

Sol-gel reaction, with the same advantage of using lower temperature, was also successfully performed. The authors reported a large amount of secondary phases at 400°C which tend to disappear at 500°C to only show some polyniobate: $K_3Nb_6O_{17}$. At 500°C, the particles sizes were in the order of 50 nm and dropped to only 20 nm at 600°C. However the large cost of niobium alkoxides, forced the authors to start with chelated Nb_2O_5. This additional step and the 54% weight loss reported constitute non-negligible drawbacks of this technique [70].

The essence of these alternative processing routes is the search for a new, low-temperature, cost- and time-effective method to create reliable KNN [86].

2.2.6 Secondary phases

As just explained in section 2.2.5, secondary phases are an important factor in the final quality of KNN. During the formation of the perovskite structure, the following reactions occur:

$$2\,Nb_2O_5 + 2\,A^+ + O_2^- \longrightarrow A_2Nb_4O_{11} \tag{2.3}$$
$$A_2Nb_4O_4 + 2\,A^+ + O_2^- \longrightarrow 4\,ANbO_3 \tag{2.4}$$
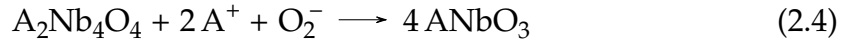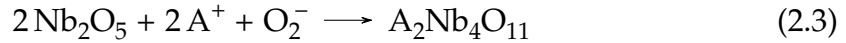
with A = K, Na. The wanted perovskite is then obtained at the interface of $(K,Na)_2Nb_4O_{11}$ and the carbonates. However, the different diffusion rates of the cations K^+ and Na^+ or the heterogeneity in the carbonate distribution are believed to be responsible for the presence of secondary phases [50]. When due to alkali losses, these secondary phases were reported to present a tungsten-bronze structure inside the matrix and consist of $K_6Nb_{10.66}O_{30}$ or $K_2Nb_4O_{11}$ [7]. The latter is consistent with Equation 2.3 and suggests a lack of potassium cations to continue the reaction. Malič et al. [7] reported a white aspect for these tungsten-bronze phases by taking a SEM backscattered electrons image, presented in Figure 2.13.
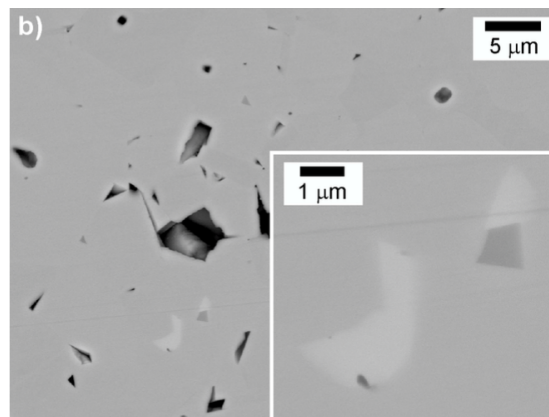
Figure 2.13: SEM image - white secondary tungsten-bronze type phase [7].

These white and sodium-deficient secondary phases were also reported by Jenko et al. [47]. Their XRD pattern didn't show the presence of these secondary phases and they exposed two hypothesis: either the amount of these secondary phases was too small to be detected or the secondary phases present the same structure as the main matrix but with a different composition [47].

Another well known secondary phase is the polyniobate $K_4Nb_6O_{17}$. Malič et al. [50] stated that the reaction between the couples K_2CO_3/Nb_2O_5 and between $(K_2CO_3 + Na_2CO_3)/Nb_2O_5$ produces more than one product and occurs at a speed lower, by one order of magnitude, than the reaction between Na_2CO_3/Nb_2O_5. This difference of rate could explain why most of the secondary phases are sodium-deficient.

These secondary phases are to be avoided as they lead to unreproducible functional properties by affecting the grain boundary mobility [53].

2.2.7 Chemical stability

Two main types of dissolution of a solid into an aqueous medium can occur: congruent and incongruent dissolution. In the first case, the solid transitions to a liquid of the same composition [16], therefore dissolves completely. While in the second case the solid transitions to a solid with another phase [44], by leakage of some species from the surface.

The reaction of cation release from a perovskite structure can be expressed with the following equations:

$$ABX_3 + H^+ \longrightarrow A^+ + BX(s) + H_2O \tag{2.5}$$
$$ABX_3 + H_2O \longrightarrow A^+ + BX(s) + OH^- \tag{2.6}$$
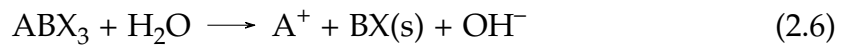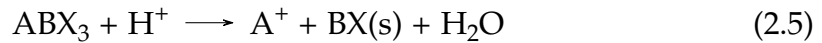
Out of these, one may conclude that for this perovskite structure, the dissolution is incongruent, A-site cations are released and a B-rich layer is formed over the core [63].

The analysis of cation release after soaking, plotted in Figure 2.14, shows that the release of K^+ is larger than the one of Na^+ by 2 or 3 times. The release of niobium is the smallest [63, 96]. This can be correlated with the ionic field strength. The ionic field is defined as the ratio of the valence ion to the ionic radius. An ionic field is therefore high when the charge is high but the radius is small. A study advanced a correlation between this ionic field (Z/r^2) and the corrosion rate of glass powders [15]. This paper showed that for a low field strength, cations had a negative Gibbs free energy of hydration (ΔG_{hyd}), implying a tendency to corrode and therefore deterioration of the material; while it is positive for a higher field strength. In the case of KNN, the relationship of the different ionic field strengths are as follows [63]:

$$K^+_{FS} < Na^+_{FS} < Nb^{5+}_{FS} \tag{2.7}$$

The Goldschmidt tolerance factor, t, indicating the stability of perovskite structure, is used to link the correlation between Z/r^2 and the corrosion with the enthalpy of formation. A high t represents a high surface energy and therefore less stability in an aqueous environment. t is function of the radii of the ions present in the structure as expressed by the relationship

$$t = \frac{R_A + R_O}{\sqrt{2}(R_B + R_O)} \tag{2.8}$$

where R_A is the radius of the cation A, R_B the radius of the cation B and R_O the one of the oxygen [6, 63]. In case of KNN, $t_{KN} > t_{NN}$ [63] which is correlated
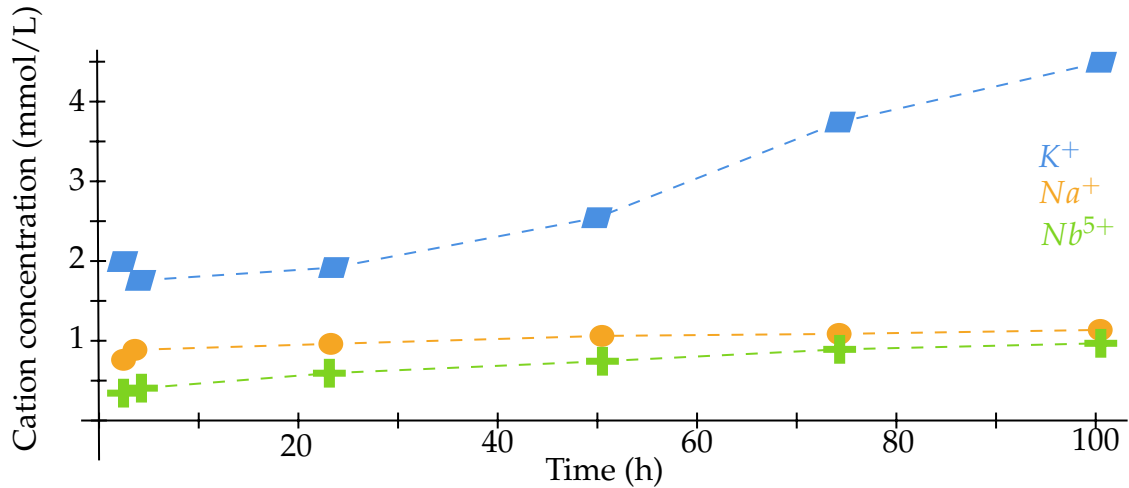
Figure 2.14: Released cation concentration of 0.5wt% aqueous fine KNN suspensions. Adapted from [63]

with the more exothermic formation enthalpy of KN (-207 kJ/mol) compared to NN (-141 kJ/mol). Ozmen et al. [63] formulated therefore the hypothesis that lowering the surface energy is done by the leaching of A-site cations to obtain a more stable B-rich surface.

The rate of dissolution is a function of the alkalinity of the soaking media. Niobium's dissolution is promoted by the amount of OH^- present in solution. This was confirmed by experimental data: when the pH of the diluting solution increases, the amount of Nb^{5+} released increases. The A-site cations have a higher dissolution rate when the media is acidic [63].

2.2.8 Mechanical stability

Mechanical properties are of fundamental importance when keeping in mind the final biomedical application of KNN. The hardness needs to be high for the ceramic to serve as a load-bearing material and to ensure the longevity of the implants. These mechanical properties have to be controlled upon soaking.

Table 2.1 shows the evolution of the biaxial strength of KNN upon soaking in normal saline measured with one-ball-on-three-ball testing. The same authors performed another soaking study on KNN one year later and observed the same drop of 20% in strength after 7 days of soaking [96].

In the following paragraphs, mechanical properties of pure KNN and KNN-based piezoceramics are presented.

	0 days	7 days	14 days	28 days
Biaxial strength (MPa)	161± 6	132± 6	131 ± 2	128 ± 12

Table 2.1: Change of biaxial strength of KNN after soaking in normal saline. Adapted from [95]

The Young's Modulus of KNN was reported to be 104 GPa [60] and is of the same order of magnitude as the value reported for KNL-NTS: 101.9 ± 18.1 GPa [69] from a Vickers hardness test. This method was also used to determine the hardness of pure-KNN as 3.55 GPa [55] and varying from 1.4 to 3.8 GPa for Mn-KNN as a function of the sintering temperature [98]. The hardness of KNL-NTS was shown to be 6.4 ± 1.8 GPa [69].

Another paper investigated the evolution of the fracture toughness (K_{IC}) on KNN according to different dopings. The fracture toughness is a parameter with different definitions but its goal is to characterize the cracks formation in a material [46]. This fracture toughness is affected by the hardness: a higher hardness is empirically correlated with a lower fracture toughness. The values were obtained with the single-edge-V-notched beam (SEVNB). K_{IC} was determined as varying from 0.48 to 1.06 MPa m$^{1/2}$ when doped with lithium or LiTaSb [94]. K_{IC} of KNL-NTS was determined as 0.65 ± 0.087 MPa m$^{1/2}$ [69] and the one of KNN-BLT-6BZ as 0.95 MPa m$^{1/2}$ (also with a SEVNB technique) [54]. Table 2.2 presents these values in a more visual form.

Nanoindentation was often used to characterize thin films, a hardness of 4.5 GPa was reported [13].

During Vickers hardness test, some authors reported cracks leaving from the edges of the impress left by the indenter [98]. The lengths of these cracks were used to measure the fracture toughness of materials, however, this method was abandoned because different materials presented too different deformations [28] and more reliable techniques such as SEVNB were used instead.

	E [GPa]	$K_{IC}[MPam^{1/2}]$	H (Vickers)[GPa]	Citation
KNN	104		3.55	[60, 55]
KNL-NTS	101.9 ± 18.1		6.4 ±1.8	[69]
Mn-KNN			1.4 - 3.8	[98]
KNN-Li		0.48		[94]
KNN-LiTaSb		1.06		[94]
KNN-BLT-6BZ		0.95		[54]

Table 2.2: Mechanical characterization of KNN-based piezoceramics.

2.3 Measurement methods

2.3.1 Nanoindentation

Nanoindentation was first used in 1992 [62]. This technique is mainly applied to determine the hardness and the elastic modulus of materials [77] even if other characteristics can also be obtained [101, 77]. A known load is applied with an indenter on the material, the corresponding displacement is measured and a load displacement curve is obtained. Different indenters exist with different geometrical parameters. A typical resulting curve can be seen in Figure 2.15. As highlighted by this Figure, the loading step consists of both elastic and plastic deformation. Upon unloading and accordingly to plastic deformation's definition, only the elastic deformation is recovered and an indentation with a depth of h_r remains visible on the surface [101].
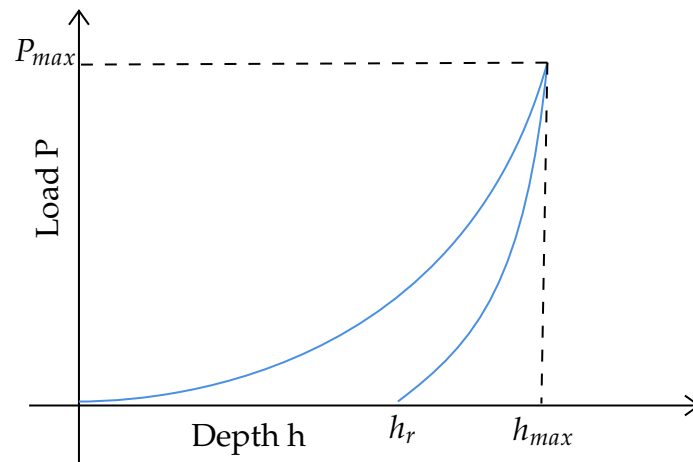
Figure 2.15: Typical load-displacement curve. Adapted from [101]

The two parameters of interest in this work are the hardness H and the elastic modulus E. With the Oliver and Pharr method, they are defined as:

$$H = \frac{P_{max}}{A} \tag{2.9}$$

$$E_r = \frac{S\sqrt{\pi}}{2\beta\sqrt{A}} \tag{2.10}$$

where A is the projected contact area, S the contact stiffness (that depends on the slope of the unloading at maximum displacement) and β a parameter which depends on the type of indenter [85].

The elastic modulus of the sample can be determined by using the calculated reduced modulus, E_r, that combines the elastic behavior of both the sample and

the indenter thanks to the formula

$$\frac{1}{E_r} = \frac{1 - \nu^2}{E} + \frac{1 - \nu_i^2}{E_i} \tag{2.11}$$

where ν_i is the Poisson's ratio of the indenter, E_i its Young modulus, ν the Poisson's ratio of the sample being tested, and E its Young modulus.

The area function is approached by a polynomial:

$$A = C_0 h_c^2 + C_1 h_c + C_2 h_c^{1/2} + C_3 h_c^{1/4} + C_4 h_c^{1/8} + C_5 h_c^{1/16} \tag{2.12}$$

The parameters of this equation can be determined empirically, by performing a set of indents at different loads on fused quartz, a sample whose properties are known [41].

2.3.2 Microindentation

Microindentation is equivalent to a Vickers hardness test: an indent of a given geometry applies a known load and leaves an imprint on the surface which depends on the depth of penetration. This is shown in Figure 2.16 where the dimensions of the indent are also illustrated.
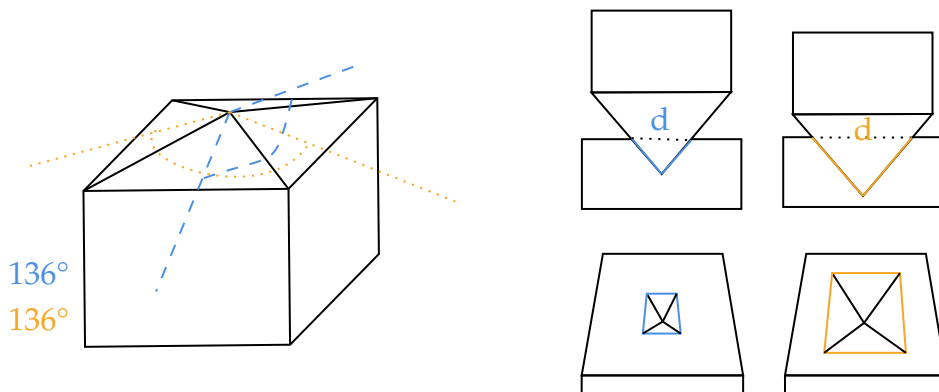
Figure 2.16: Vickers indenter (left) and influence of the depth on the size of the indent (right). Adapted from [90]

The Vickers Pyramid Number (HV) is obtained by the formula

$$HV = \frac{F}{A} \tag{2.13}$$

where F is the force applied and A the surface. This Vickers Pyramid Number is expressed in kgf/mm^2, a unit not part of the SI. The value therefore has to be multiplied by $9.807 \cdot 10^{-3}$ in order to be converted to GPa.

The surface can be obtained by calculating the projected area of the indent. In the next formula, α is the angle between two opposite faces of the indenter.

$$\text{Projected area} = \int_A \cos\alpha \, dA \tag{2.14}$$

$$= A \cdot \sin\left(\frac{\alpha}{2}\right) \tag{2.15}$$

From the geometry of the indent the expression

$$\text{Projected area} = \frac{d^2}{2} \tag{2.16}$$

is verified. In this equation, d is the diameter of the indent. It can be obtained by measuring the diagonals as shown in Figure 2.17. These two diagonals are measured on the microscope of the indenter.

$$d = \frac{d1 + d2}{2}$$
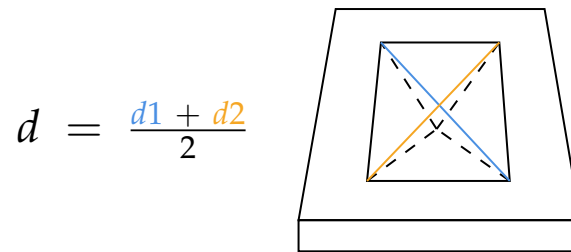
Figure 2.17: Diameter of the Vickers indent.

By equating equations 2.15 and 2.16 and considering $\alpha = 136°$ based on the geometry of the indenter, the following equation of the surface A is obtained and can be used in the Equation 2.13.

$$A = \frac{d^2}{2\sin\left(\frac{136°}{2}\right)} \tag{2.17}$$

CHAPTER

3

METHODOLOGY

This chapter aspires to provide the methodology applied during this work. It starts with the solid-state synthesis, continues with a presentation of the characterization method and finally provides the sample preparation and the soaking procedure.

3.1 Chemicals and apparatus

The chemicals used for this work are listed in Table 3.1 while the apparatus can be seen in Table 3.2.

Chemicals	Manufacturer	Purity
Na_2CO_3	Aldrich	99.999%
K_2CO_3	Aldrich	99.995%
Nb_2O_5	Aldrich	99.99%
Absolute ethanol	vwr	100%
Isopropanol	Supelco	100%
NaCl	Aldrich	99.5%

Table 3.1: Chemicals used for the experimental work.

3.2 Sample synthesis

The procedure to produce the samples is based on the previous work of Angelica Marie Maza Larsen [52]. This solid-state synthesis relies on four main steps, illustrated in Figure 3.1 :

- milling of the precursors,

- heat treatment (calcination),

- milling,

- heat treatment (sintering).

Apparatus	Model	Purpose
Drying oven	Termaks TS 8056	Drying of precursors and samples
Planetary ball mill	RETSCH - PM 100	Milling
Rotary evaporator	BUCHI - R-210	Evaporating the solvent
Mortar	VWR Mortar with Pestle agate	Grinding of the powder
Oven	Nabertherm muffle furnace	Heat treatments
Digital caliper	Cocraft 0-150mm	Measuring samples
Hydraulic press	c-press	Pressing the pellets
Uniaxial press	Mäder pressen 25kN	Pressing the pellets
CIP	Autoclave Engineers	Pressing the pellets
Digital indicator	Burster Digilow	Measuring the pressure applied to samples
Analytical scale	Sartorius Entris	Weighting precursor and samples
Ultrasonic cleaner	Branson Bransonic 3800	Cleaning of samples
Environmental chamber	Termaks	Ccontrol environment during soaking
Raman spectrometer	WITec Alpha 300R	Raman spectroscopy
X-ray Diffractometer	Bruker D8 ADVANCE DaVinci	XRD analysis
X-ray Diffractometer	Bruker D8 ADVANCE DaVinci	GIXRD analysis
Indenter	TI 950 TriboIndenter	Nanoindentation
Indenter	Leica VMH MOT Vickers	Microindentation
SEM	Zeiss ULTRA 55	SEM imaging
pH-meter	Mettler-Toledo	pH measurement
Carbon-coated	Cressington 208 carbon	Sample coating

Table 3.2: Apparatus used for the experimental work.

The procedure described in the following section resulted in around 3.5 g of final product and was repeated three times. The three precursors are Na_2CO_3, K_2CO_3 and Nb_2O_5. Respectively 2.3114 g, 3.0141 g and 11.5936 g are needed. The exact amount used per batch is presented in appendix A. Because these precursors tend
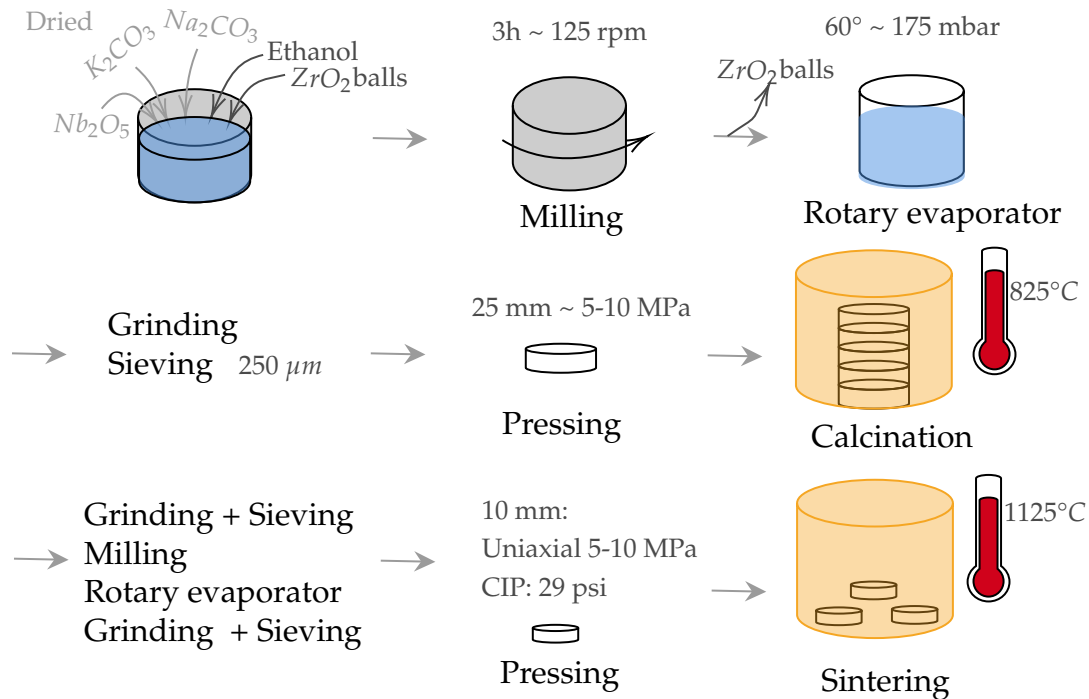
Figure 3.1: Illustration of the different steps of the solid-state synthesis.

to react with humidity they are dried overnight in a drying oven (around 110°C) before being weighed. They are then put in a milling jar of 250 mL with 190 g of grinding balls (composed of ZrO_2) and 80 g of ethanol absolute. The mixture is then put in a planetary ball mill for 3 hours at a speed of 125 rpm with an inversion time of 10 min and a break time of 30 seconds. This mixture is quickly recovered when the milling is done and sieved. The sieve has only one goal: to recover the grinding balls.

The liquid is put to dry in a rotary evaporator with the following parameters: bath temperature: 60°C, solvent: ethanol, rotation speed: 2. The needed pressure is calculated by the device and equals 175 mbar. The mixture stays in the evaporator until it is fully evaporated (it took between 45 minutes and 1 hour). The dried powder is then grinded in a mortar and sieved in a 250 μm sieve.

This powder is pressed with a uniaxial press and a pressing die of 25 mm diameter using 5-10 MPa for 15 seconds. 3 g of powder are used per pellet. The five pellets obtained are then put in an alumina crucible on top of each other with some sacrificial powder on the bottom and on top to limit volatilization. The crucible is closed at 85% by an alumina lid and put in an oven for calcination. The temperature profile is depicted in Figure 3.2. The calcination follows an increase temperature of 3°C/min until 825°C, a 4-hour plateau and a decrease of 10°C/min.
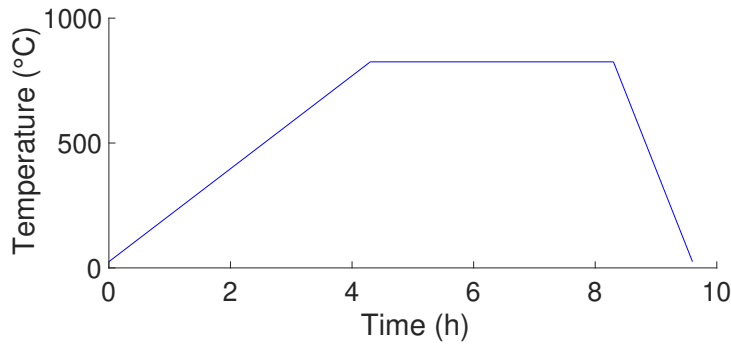
Figure 3.2: Temperature evolution over time for calcination.

Once the calcination has finished, the pellets are grinded in a mortar and sieved in a 250 μm sieve then mixed with 190 g of grinding balls and 80 g of absolute ethanol. The treatment in the planetary ball mill lasts for 3 hours with the same parameters as the first passage before calcination. The mixture is recovered and placed into a rotary evaporator, once again with the same parameters as the passage before calcination. Once the powder is dry, it is recovered, grinded and sieved (250 μm). Finally the powder is pressed in its final form: a pellet of around 0.3 g with a diameter of 10 mm. Two different presses are used one after the other. First the pellets are pressed using a uniaxial press by applying again a load of 5-10 MPa for around 15 seconds. Then these pellets go to a cold isostatic press up to 29 psi (1.99948 bar) for 2 minutes. The pellets from the batch c were pressed with a different uniaxial pressed. One with a more precise measurement system and also with a lower pressure of 4 MPa because the first results showed some defects that could be pressing defects; this will be explained in section 4.2. The pellets are, three by three and with sacrificial powder, sintered. The temperature profile is shown in Figure 3.3: an increase in temperature of 5°C/min until 1125°C, a 2-hour plateau, and a decrease of 10°C/min. As explained in the literature review (section 2.2.5), sintering comes with a densification of the material. Some mass losses are expected because of the volatilization. Figure 3.4 plots the mass lost during sintering for the different pellets. Between all the different steps, the samples are placed in a desiccator.

3.3 Sample preparation

Before undergoing the different characterization methods, the samples need to be polished. Three grinding papers and two polishing cloths were used, the grid of which gradually decreases until it reaches a quarter of a micron.

The procedure was the following. Ethanol absolute is poured on a grinding paper, composed of SiC and with a size of 1200 (corresponding to 15 μm). By maintaining the pellet with two fingers on the paper, the infinity symbols is drawn
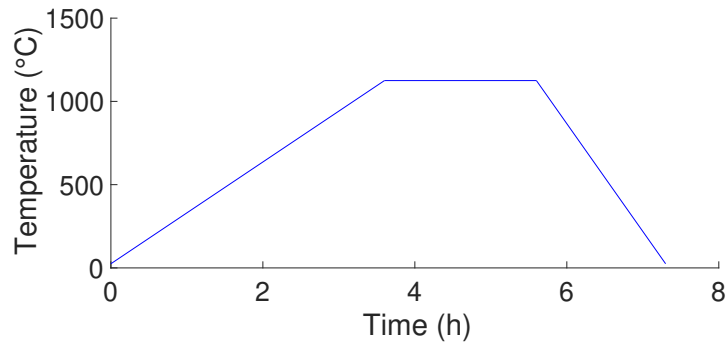
Figure 3.3: Temperature curve for sintering
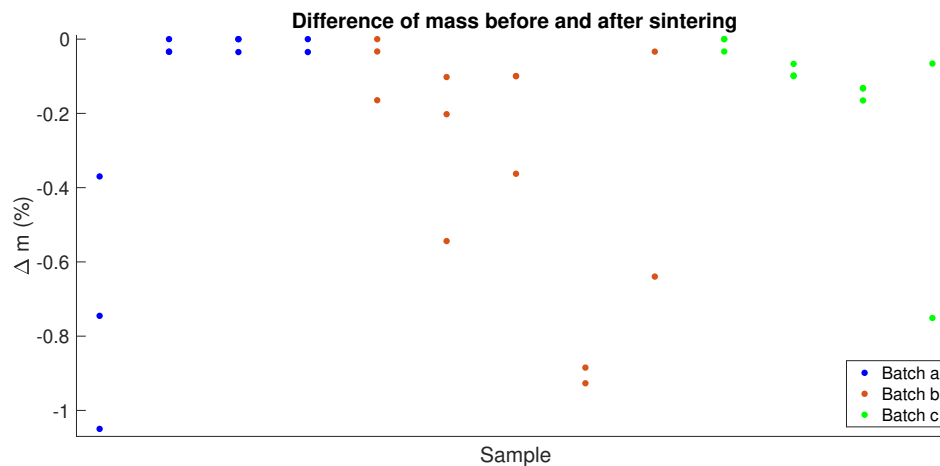
Figure 3.4: Mass loss from sintering. Each column corresponds to three samples that were sintered together. For some columns only two samples are present as the mass of the third sample could not be measured after sintering.

around thirty times in each direction and on each side of the pellet. The sample is then cleaned in absolute ethanol by using sonication before being visually inspected by an optical microscope. If the result isn't satisfying, the step is repeated. If the result is satisfying, a grinding paper of size 2000 (10.3 μm, also SiC) is used with the same procedure followed with a 4000 (5 μm) grinding paper of SiC. For the next step, using a 1 μm cloth with diamond paste, the procedure is the same except that ethanol isn't used on the paper but with a special spray composed of polycrystalline diamonds and the amount of infinity symbols is increased to forty. The last passage is performed with a 0.25 μm cloth and another spray containing polycrystalline diamonds.

3.3.1 Thermal etching

Before undergoing Scanning Electron Microscopy, a polished sample needs to be thermally etched. The setup can be seen in Figure 3.5. This treatment consists in heating the sample for 7 minutes at 1070°C, a slightly lower temperature than the sintering temperature, with a heating and cooling rate of 600°C/h.

Figure 3.5: Setup for thermal etching

3.4 Characterization methods

Different characterization methods were applied during this work in order to understand both the structure and the mechanical behavior of the samples after soaking. The order in which they were applied was determined from the least to the most destructive. The nanoindentation is placed before the microindentation as the latter presents a higher chance of fracturing the sample. The SEM is the last characterization method performed to be able to see the indentation and because of the carbon coating. Figure 3.6 schematizes the typical route followed by the samples.

3.4.1 Density measurement

Two different methods were applied to determine the density: geometrical and Archimedes measurements. This was performed only before the soaking.

Geometrical measurement

The first method, applied to all samples, uses the fundamental definition of density: the mass per unit of volume. The pellets are weighed and this mass is di-
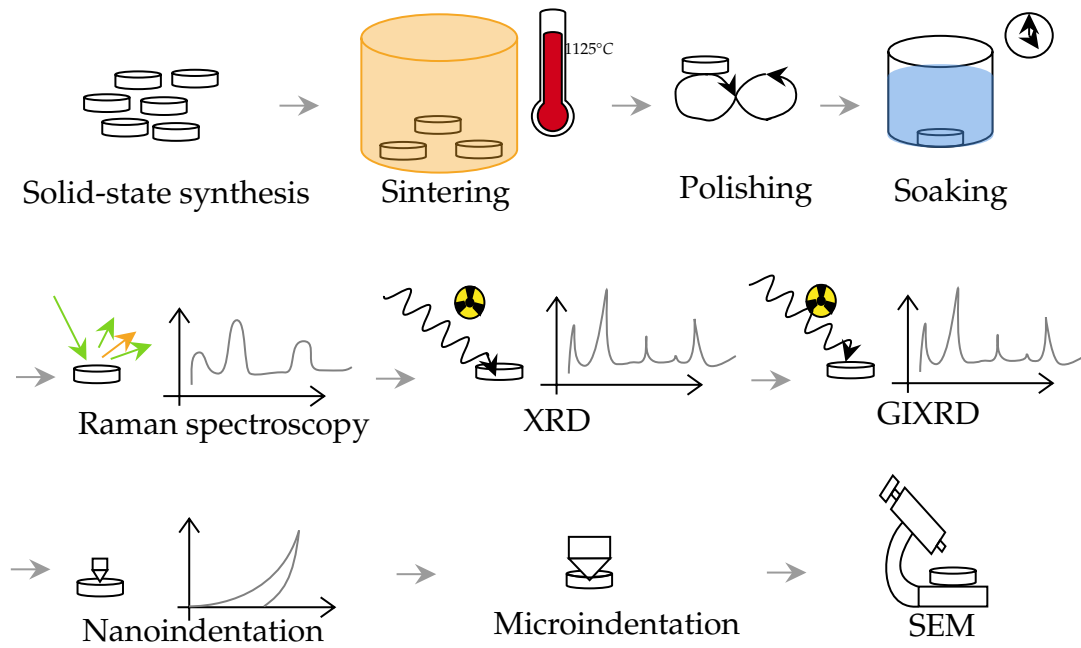
Figure 3.6: Schematic of the typical route followed by samples.

vided by the volume. The density ρ is calculated as

$$\rho = \frac{m}{\pi r^2 t} \tag{3.1}$$

where m is the mass, r the radius and t the thickness.

The diameter and the thickness were obtained by using a digital caliper and averaging 4 measurements.

The relative density was then obtained by dividing this density by the theoretical density of KNN. This theoretical density is equal to 4.51 g/cm^3 [14].

This method deems the pellet to be a flawless cylinder and underestimates the actual density. Indeed, the sample is porous so its volume is bigger than it would be if it were dense. Therefore, in Equation 3.1, the denominator is overestimated which makes the density underestimated.

Archimedes measurement

This method is known to be robust and precise but also time consuming.

The bulk density ρ_b is expressed as

$$\rho_b = \frac{m_1}{m_3 - m_2} \cdot \rho_{liq} \tag{3.2}$$
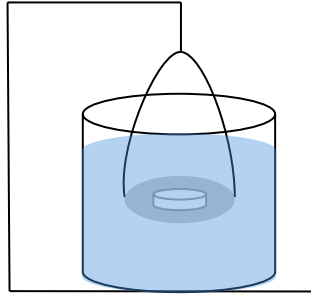
Figure 3.7: Schematic representation of the measurement of m_2 for the Archimedes method.

where the density of the liquid (ρ_{liq}) follows the density-temperature correlation

$$\rho_{liq} = -0.0009 \cdot T + 0.8018 \tag{3.3}$$

and m_1, m_2 and m_3 are the masses of the sample at different stages that are explained in the following paragraphs.

The samples need to be dried overnight in a drying oven. m_1 is the mass of the dried sample.

The aim of the next stage is to fill all the pores with isopropanol. This alcohol is chosen because of its non-reactivity with respect to KNN and its low volatility compared to ethanol. The first step is to place the sample in a desiccator in which the air is pumped out to obtain vacuum and maintain it for 20 min. The goal of this step is to take all the air out of the pores of the sample. Isopropanol is then added in this container (without breaking the vacuum) and the samples are let to soak for 30 min. m_2 can be obtained by measuring the mass of the sample still immersed. The setup can be seen in Figure 3.7. A basket is immersed in the liquid and attached to the scale and the sample is placed on the basket without leaving the liquid. At this stage, the temperature of the immersion liquid is measured.

The last mass to measure, m_3, is the one of the samples sponged with a wet tissue impregnated by isopropanol so that all the pores are still filled by the liquid while making sure there is no excess of liquid around the sample.

3.4.2 Raman spectroscopy

The goal of a Raman spectroscopy is to measure the vibrational structure of a sample and therefore to retrieve information about its composition. The bond between atoms inside a molecule are elastic and can be represented as springs. Upon any perturbation, these bonds will oscillate at a given frequency that depends on the molecule [30]. The set of molecular vibrations represents the chemical fingerprint of a molecule and this fingerprint is what Raman spectroscopy

aims to obtain as it allows to identify which functional groups are present [5, 58].

The purpose of Raman spectroscopy in this work is to locally measure the fingerprints of structures that are present before and appearing after soaking.

The result of a Raman spectroscopy is a spectrum of the intensity of the scattered light as function of the Raman shift which is the energy difference between the incident beam and the scattered one. The Raman shift can be expressed as a wavelength or as a *wavenumber* defined as the inverse of the wavelength. The intensity of a Raman band will increase with the polarity of the bond. The bands can be qualified as strong, medium or weak depending on the intensity and qualified as broad or sharp depending on the broadness on the x-axis [58].

During this work the samples were analyzed using the following parameters: the laser had a 532 nm wavelength, and 66 mW power. The latter value was determined as a trade-off: the higher the power, the higher the signal but also the higher the risk to burn the sample. With these parameters, the depth of measurement equals 0.7 μm [3].

Two types of measurement were performed using the optical microscope with an objective of 50x:

- Local scan to focus on a visible defect, where the integration time was 1 second,

- Large area scan to average the measurement on a larger surface. The integration time was 0.5 seconds. 25 points were measured per line and 25 lines per image on a 25x25 μm^2 surface.

This was kept consistent for every sample.

3.4.3   X-ray diffraction

Two different types of X-ray diffraction measurements were performed to analyze both the bulk and the surface of the samples. These techniques are non-destructive.

X-ray diffraction

The goal of XRD is to analyze the bulk atomic or molecular structure of a material. The sample to analyze is irradiated with X-rays that will scatter. An XRD analysis results in a pattern representing the intensity of these scattered X-rays as a function of the scattering angle [48]. A peak on the XRD pattern reflects the presence

of a certain type of crystalline structure as presented in the previous chapter, section 2.2.1. Comparing the present crystal plane to a database containing reference patterns will allow to identify the composition of the sample analyzed.

During this work the samples were analyzed with the angle between the transmitted and reflected beam, 2θ, ranging from 15 to 75 degrees. Each of the 4512 steps lasted 1.52 seconds. This was kept consistent for every sample.

Grazing incidence X-ray diffraction

The second X-ray diffraction method, grazing incident X-ray diffraction, GIXRD for short, uses the same principle as XRD but with a fixed grazing angle of incidence of the X-ray beam with aim to restrain penetration within the bulk. It therefore serves as a surface-sensitive characterization method. The principle is schematized in Figure 3.8 where α is kept constant. In the XRD, the angle between the sample and the scattered beam was equal to θ, for the grazing incident XRD, this angle equals $2\theta - \alpha$ [9].
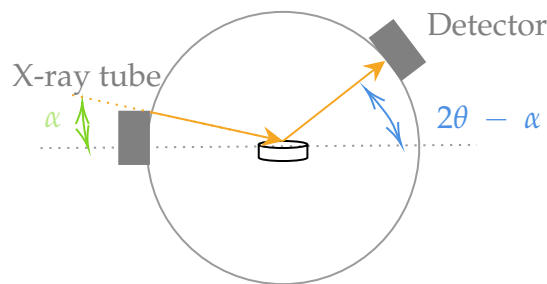
Figure 3.8: Configuration of the GIXRD. Adapted from [9].

During this work the samples were analyzed using the following parameters: two-theta scan type between $20°$ and $78°$ with 2901 steps each lasting 4 seconds. The incident angle is set to $0.5°$, the lowest possible to ensure that the sample is seen and without having to determine the critical angle of the material. This was kept consistent for every sample.

The depth of penetration of the beam in the sample depends on several parameters and it was determined with a specific software from Bruker, *AbsorbDX*. Considering a composition of $K_{0.5}Na_{0.5}NbO_3$, a density of $4.51 \, g/cm^3$ (the theoretical density of KNN), the incident angle of $0.5°$ and the parameter of the anode, the depth was determined to vary from $0.436 \, \mu m$ to $0.443 \, \mu m$ for 2θ varying from $20°$ to $78°$.

3.4.4 Nanoindentation

In the scope of this work, a calibration was performed once on a fused quartz sample, following the methodology found in the user manual [41] in order to obtain the area function and therefore the hardness as presented in the literature review (section 2.3.1). The load function had a load time of 5 seconds followed by a hold time of 3 seconds and then a 5-second unload time. The range of load increased from 100 μN to 10000 μN on a 7-by-7 array (therefore 49 indents). No outlier curves were observed during this calibration. The area function was approached with 3 parameters as it gave a satisfying fit for the curve.

A Berkovich indenter was used as this geometry (Figure 3.9) is the best fit for the measurement of hardness and elastic modulus [101], ideal for ceramics and hard materials [41] and that other geometries such as cylinder and wedge-shape are best suited for soft materials [101]. The load function has a maximum peak value of 8000 μN with a rate of 800 μN/s (both for the loading and unloading) and a total of 4000 data points. This was kept consistent for all the measurements. The instrument was placed in a lab equipped with ground vibration reduction to ensure isolation from surrounding noise.
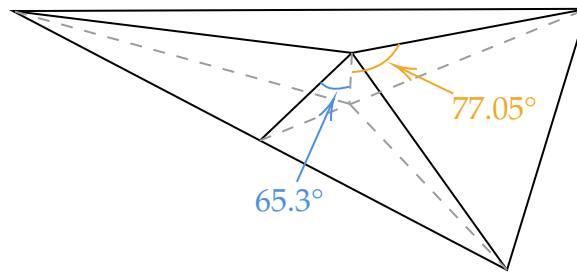
Figure 3.9: Berkovich indenter. Adapted from [101], not at scale.

3.4.5 Microindentation

The goal of this characterization technique is to measure the bulk hardness. As presented in the literature review, section 2.3.2, it consists of a Vickers hardness measurement. The load, chosen between 500 g and 2 kg, was maintained for 10 seconds.

This technique presents some limitations as the measurement of the diameter is made manually and depends on the person performing the measurement. This drawback can be scaled down by having the same operator performing the measurement every time and measuring several times one indent.

3.4.6 SEM/EDX

SEM stands for Scanning Electron Microscope and EDX for Energy Dispersive X-ray spectroscopy. This high spatial resolution microscope ($\sim$ 1 nm) uses the interaction between an incident beam of electrons and the sample to determine the morphology, topography and grain orientation of the sample. The incident beam of electron is accelerated with a voltage that can be setup to 30 kV. EDX can be performed on an area and gives a map, or on a line, or on a specific point. This technique is semi-quantitative [89].

Samples need to be prepared to undergo SEM analysis. They need to be placed on a carbon tape and recovered with a conductive layer to avoid overcharging [4]. In this work the samples were carbon-coated using 2 rounds of 8 seconds at 4.8 V.

When observed with SEM, KNN exhibits cubic grains. Intragranular grains are repeatedly observed and can be linked to abnormal grain growth.

Two different SEM were used: Zeiss ULTRA 55 for imaging and the one from the NTNU NanoLab for the EDX measurements.

3.5 Soaking

The soaking was performed following the ISO 23317 international standard about the in vitro evaluation for apatite-forming ability of implant materials [1].

The volume of liquid V_s required for the soaking was calculated based on the international standard:

$$V_s = 100 \cdot S_a \tag{3.4}$$

where S_a is the apparent surface of the specimen. As the samples used in this work are pellets, the apparent surface can be calculated using:

$$S_a = 2\pi \cdot (r^2 + rt) \tag{3.5}$$

with r the radius and t the thickness of the sample. These measurements were obtained by averaging four measurements obtained with a digital caliper.

The samples were placed in a plastic bottle as shown in the picture of Figure 3.10. It was then placed into a environmental chamber with a controlled temperature fixed at 37°C. A thermometer was used to monitor the temperature.

After the soaking the samples were recovered with plastic tweezers and rinsed with the liquid they were soaked in. They were wiped with virgin fiber tissue wipers, put in a glass container and placed in a desiccator overnight.
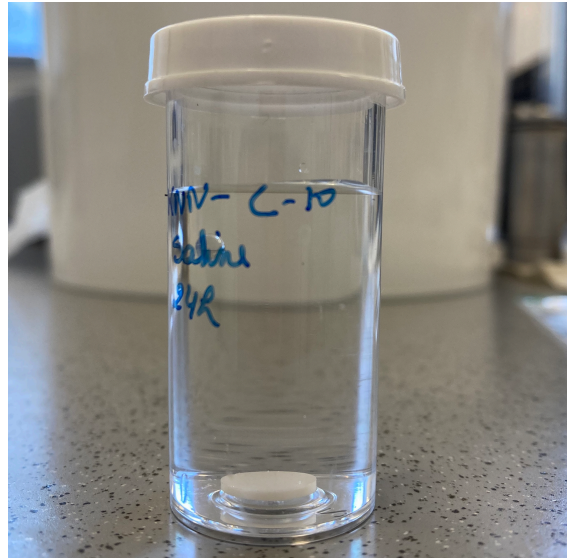
Figure 3.10: Setup for soaking

Liquids used

The different liquids used are:

- Ultra pure water.

- Deionized water.

- Saline solution which was obtained by mixing sodium chloride and water. A concentration of 0.9% NaCl was used as it represents a widely used standard.

They were used to improve the complexity and the presence of ions in the solution step by step and study their impact on the properties of the samples.

For each liquid, the samples were soaked for 12h. This decision was based on the first results observed. For saline solution, samples were also soaked for 6, 24 and 72h. In order to retrieve more information about the mechanism in place during soaking, the mass of the samples was measured before and after soaking, in both cases after a night in a desiccator. As presented in Figure 3.11, the pH of the solution in which the samples were soaked was also measured and compared to a control solution: the same saline solution also present in the environmental chamber but without any samples soaked in it in order to account for the evolution of the pH with the air. This was done for the soaking in saline solution for 6, 24 and 72h.

Four samples were used for each soaking condition. This number was determined as a trade-off between a reasonable amount of experiments to conduct and a sufficiently large dataset.
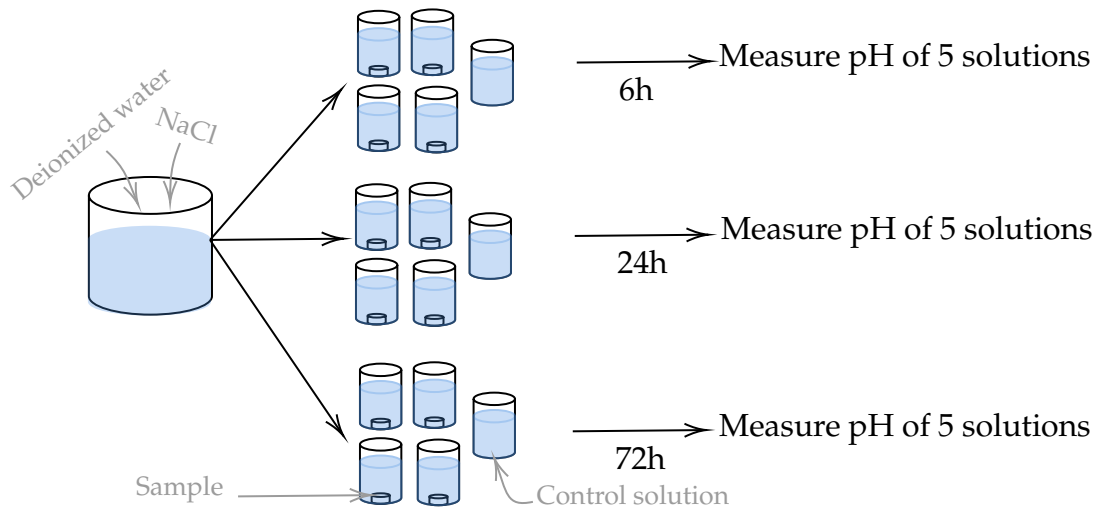
Figure 3.11: Illustration of the methodology applied for the pH measurement after soaking in saline solution.

3.6 Sample tracker

Table 3.3 summarizes the treatment that every sample went through. Orange corresponds to the characterization before soaking while blue corresponds to the method applied after soaking. The letter in the name of the sample corresponds to the batch in which it was produced (a, b or c for the three batches).

	Raman	XRD	GIXRD	Nanoind	Microind	SEM	Soaking media	Time
a-01						✓		
a-02				✓	✓			
a-03	✓		✓	✓				
a-04	✓	✓		✓✓	✓	✓	Ultra pure water	12h
a-05	✓	✓	✓	✓✓	✓	✓	Ultra pure water	12h
a-06	✓	✓✓	✓	✓✓	✓		Ultra pure water	12h
a-07	✓	✓		✓✓	✓		Ultra pure water	12h
a-08	✓	✓	✓	✓✓	✓	✓	Deionized water	12h
a-09	✓	✓		✓✓	✓	✓	Deionized water	12h
a-10	✓	✓	✓	✓✓	✓		Saline solution	12h
a-11	✓	✓		✓✓	✓	✓	Saline solution	12h
a-12	✓	✓		✓	✓			
a-13								
a-14	✓	✓		✓	✓			
b-02	✓	✓	✓	✓	✓			
b-03	✓	✓		✓✓	✓	✓	Saline solution	6h
b-04	✓	✓	✓	✓✓	✓	✓	Saline solution	72h
b-06	✓	✓	✓	✓✓	✓		Saline solution	24h
b-07	✓	✓		✓✓	✓	✓	Saline solution	24h
b-08	✓	✓	✓	✓✓	✓		Saline solution	6h
b-11	✓	✓		✓✓	✓		Saline solution	72h
b-12	✓	✓		✓	✓	✓		
c-01	✓	✓	✓	✓✓	✓	✓	Deionized water	12h
c-02	✓	✓		✓✓	✓		Deionized water	12h
c-03	✓	✓	✓✓	✓✓	✓		Saline solution	6h
c-04	✓	✓		✓	✓	✓	Saline solution	12h
c-05	✓	✓	✓	✓	✓		Saline solution	12h
c-06	✓	✓			✓	✓		
c-07				✓	✓			
c-08	✓	✓		✓✓	✓	✓	Saline solution	6h
c-09	✓	✓	✓	✓✓	✓	✓	Saline solution	24h
c-10	✓	✓		✓	✓		Saline solution	24h
c-11	✓	✓	✓	✓	✓		Saline solution	72h
c-12	✓	✓		✓	✓		Saline solution	72h

Table 3.3: Sample tracker

CHAPTER

4

RESULTS

This chapter exhibits the raw results obtained for the different characterization methods presented in section 3.4. For each of these methods, the results are displayed and compared. To ease the understanding of the reader and to highlight the different soaking conditions, a color code was followed for all the Figures containing data after soaking. It is given in Figure 4.1: 12h in ultra-pure water is represented in blue, 12h in deionized water in pink, green for 12h in saline solution, black for 6h in saline solution, purple for the 24h soaking and finally yellow for the 72h soaking. Four shades are used per soaking condition as it represents the amount of samples soaked.
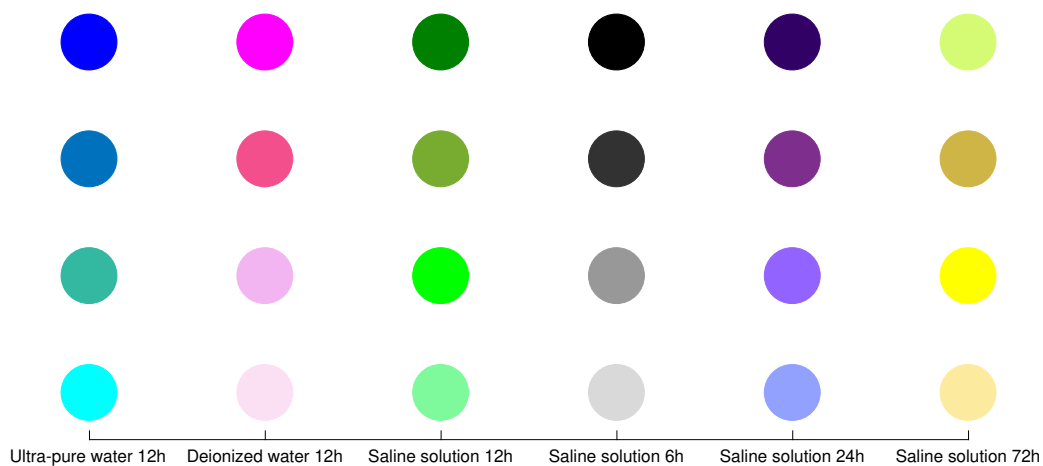
Figure 4.1: Colors used in the different Figures according to the soaking media and the soaking time.

4.1 Density measurement

4.1.1 Geometrical measurement

Figure 4.2 contains the density of the different samples measured with the geometrical method as presented in section 3.4.1. Note that the full dots correspond to samples with a small chip on corner. The method is less precise for them and the relative density could be underestimated. The corners were not highly chipped and this shouldn't lead to big differences in relative density. The different measurements for the dimensions are presented in Appendix B. The average relative densities are 93.22%, 92.18% and 95.60% for respectively batch a, b and c.
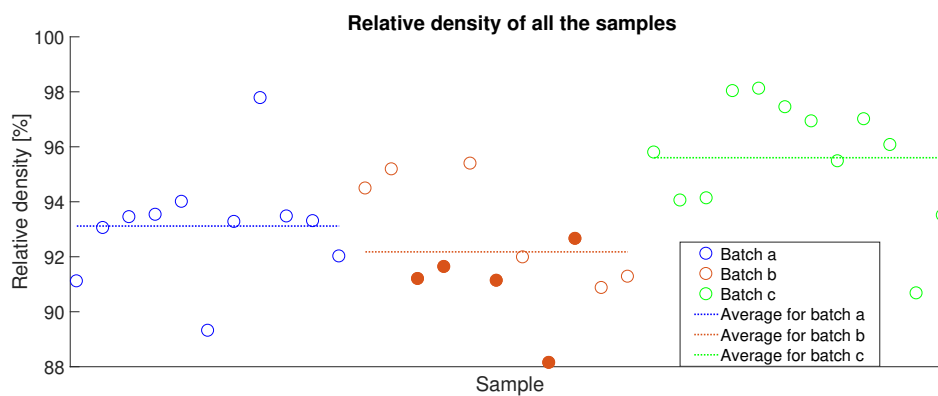
Figure 4.2: Relative density of the samples calculated with geometrical measurement

4.1.2 Archimedes measurement

This method was applied on eight samples, with the procedure described in section 3.4.1. The results are presented in Table 4.1 and compared to the value obtained by the geometrical measurement method. The values obtained with Archimedes are sometimes bigger and sometimes smaller. Some values are questionable, for example the one of 82% that is low compared to the rest and the value of 101% which is surprising. These results are discussed in the next chapter (5.1.1).

	a-05	a-10	a-12	a-14	b-02	b-09	b-11	c-03
Geometrical [%]	93.05	93.27	93.47	92.02	94.49	88.15	90.87	94.13
Archimedes [%]	89.93	91.11	82.25	101.31	95.64	91.67	93.04	92.93

Table 4.1: Comparison between the relative densities calculated by geometrical measurement and the ones obtained using Archimedes measurement.

4.2 Observation after soaking

4.2.1 After 12h soaking

Table 4.2 presents the visual appearance of all samples after 12h of soaking in the different solutions.

It can be seen that for soaking in ultra pure water, the samples exhibited different behaviors. Sample a-04 broke during soaking but the rest of its surface seemed untouched. Samples a-05 and a-07 presented a big crack and a shiny surface. The last sample, a-06, presented a normal-looking surface with the presence of dots evenly distributed.

After soaking in deionized water, sample a-08 exhibited several cracks and the same shiny surface as for some samples soaked in ultra-pure water. The second sample from batch a, a-09, presented a normal-looking surface with the presence of dots evenly distributed on the surface. Samples c-01 and c-02 from batch c seemed flawless.

The soaking on saline solution also presented two different behaviors based on the batch the samples originated from. Samples a-10 and a-11 broke and one of the pieces exhibited a shiny surface while no flaws could be observed on samples c-04 and c-05.

4.2.2 After different periods of time in saline solution

After soaking for 6h and 24h in saline solution, the eight samples appeared flawless. On some samples soaked for 72h in saline solution, some defects could be spotted: c-11 presented a shallow crack on the edge, b-04 presented dots distributed on the surface and b-11 presented an embossed area. One out of the four sample appeared flawless. They can be seen in Table 4.2.
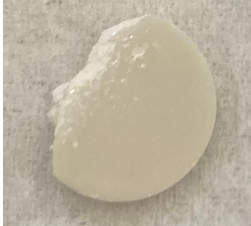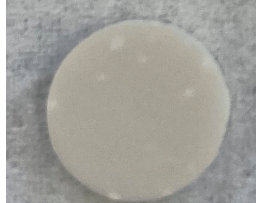
Ultra-pure water	Deionized water	12h Saline solution	72h Saline solution
a-04	a-08	a-10	c-11
a-05	a-09	a-11	c-12
a-06	c-01	c-04	b-04
a-07	c-02	c-05	b-11

Table 4.2: Visual aspect of the samples after soaking

The evolution of the mass and the pH upon soaking is presented in Figure 4.3. The first observation is that all samples from batch c present either a small loss in mass in the order of 0.1% or no changes. For batch b, the samples soaked for 24h presented the same behavior as batch c. The samples soaked for 6 and 72h however presented an increase in mass between 0.1% and 0.3%.

Looking at the pH, the one of the control solution increases with time. For the samples soaked for 6h, their corresponding pH increased compared to the control solution. Samples from batch c, even if they presented less change in the mass differences, showed a larger increase of the pH. Regarding samples soaked for 24h, the pH increased with soaking but this increase is larger for samples from

batch b than for batch c. The pH of samples soaked for 72h is steady, although a slight decrease can be observed for samples from batch c. One will notice that samples from batch b soaked for 6 an increase in mass while the ones soaked 24h presented either an increase or no change. They, however, both presented an increase in pH. The same can be observed with samples from batch c soaked for 6 and 72h, the first one presenting a decrease in mass but an increase in pH while the second presented the same decrease in mass but with an decrease in pH.
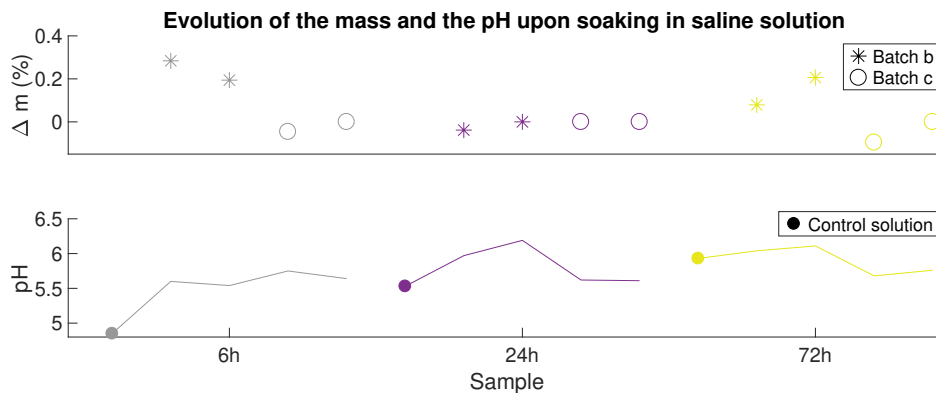
Figure 4.3: Evolution of the mass and the pH upon soaking in saline solution for 6, 24 and 72h.

When left in contact with air and because of the CO_2 present, the pH of the solutions is expected to slightly drop or to stay constant [72]. As the opposite behavior was observed in this work with an increase with time, another saline solution was prepared and put in an environmental chamber to measure the pH after 24h. The results showed a constant pH, measured before and after the 24h as 5.68 and 5.67. The increase in pH observed on the control solution is therefore dubitable.

After soaking in every solution, bubbles could be observed mainly around the sample but also in the solution, see Figure 4.4. Their amount wasn't constant and seemed to increase when cracks were present. They were also located on the container walls.
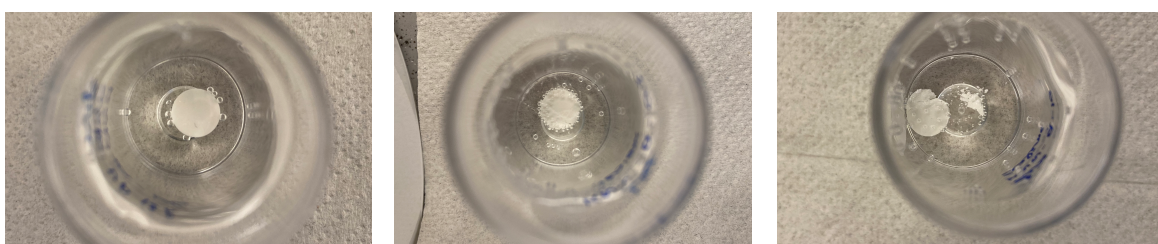
(a) In ultra-pure water   (b) In deionized water   (c) In saline solution

Figure 4.4: Amount of bubbles in the solutions after 12h soaking in different liquids.

4.3 Raman spectroscopy

Several samples were analyzed before and after soaking. In the Figures of this section, the spectra are scaled by dividing the intensity by the maximum intensity. The pictures that are presented were taken from the microscope on the spectrometer. The analyzed area is located at the center of the provided pictures.

4.3.1 Before soaking

Figure 4.5 presents spectra obtained before soaking on samples from batch a.

(a) Picture 1   (b) Picture 2   (c) Picture 3
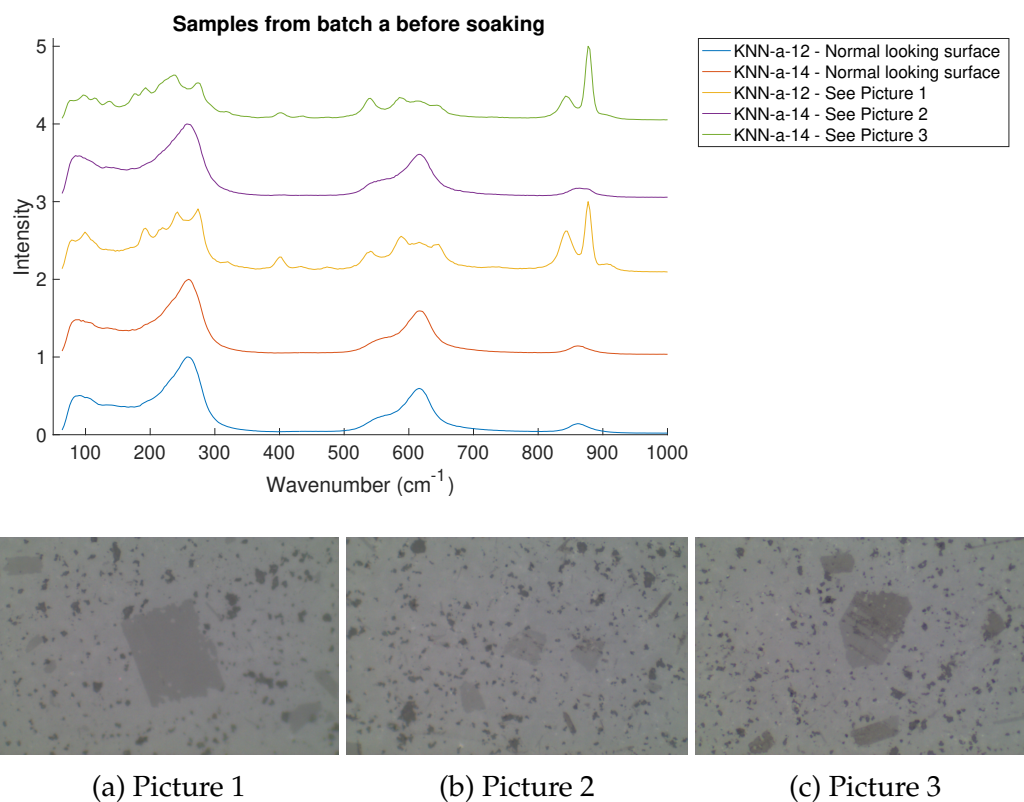
Figure 4.5: Raman spectroscopy at different locations on two samples from batch a (top) and the corresponding pictures of the surface (bottom)

For this batch the main observation is the presence of different structures at the surface that isn't homogeneous. Different gray spots are visible and present different sizes and shapes. As shown by the purple curve, some of these spots present the same spectra as the normal-looking parts of the sample and correspond to what is expected from KNN: the active modes v_1, v_5 and $v_1 + v_5$, presented in the literature review, section 2.2.1, are located at 256, 613 and 861 cm^{-1}.

For the other spots, the curves show more differences. Even if the global shape is the same, a lot of Raman bands are divided into smaller ones. Around a Raman shift of 400 cm^{-1}, a band appears on the curves representing the gray spot. Another difference lies in the $v_1 + v_5$ mode located at 861 cm^{-1}, which has a small intensity for the normal-looking surfaces and presents a splitting into two peaks, one with an increase in wavenumber (877 cm^{-1}) and one with a decrease (842 cm^{-1}). The meaning of these bands is discussed in the next chapter, section 5.2.

The surface from the samples chosen out of batch b are more homogeneous. None of the gray spots visible on the samples from batch a are visible. However some dark spots are present. They are small and evenly distributed on the surface. The spectra all have the same aspect as the blue curve from Figure 4.5, with active modes located at 256, 613 and 861 cm^{-1}. The spectra are presented in Appendix C.1. Batch c presented more similarities with batch b: no gray spots could be found, only small and evenly distributed black spots that didn't present a different spectrum in the range of interest. The spectra are also presented in Appendix C.1.

4.3.2   Layered structures

As the previous section highlighted, a layered structure appears for the samples from the first batch. These structures were also visible on the samples from the same batch after soaking. Their Raman spectra are presented in Figure 4.6.

Raman spectroscopy on the layered structures

(a) a-14   (b) a-6   (c) a-07

(d) a-08   (e) a-09   (f) a-11
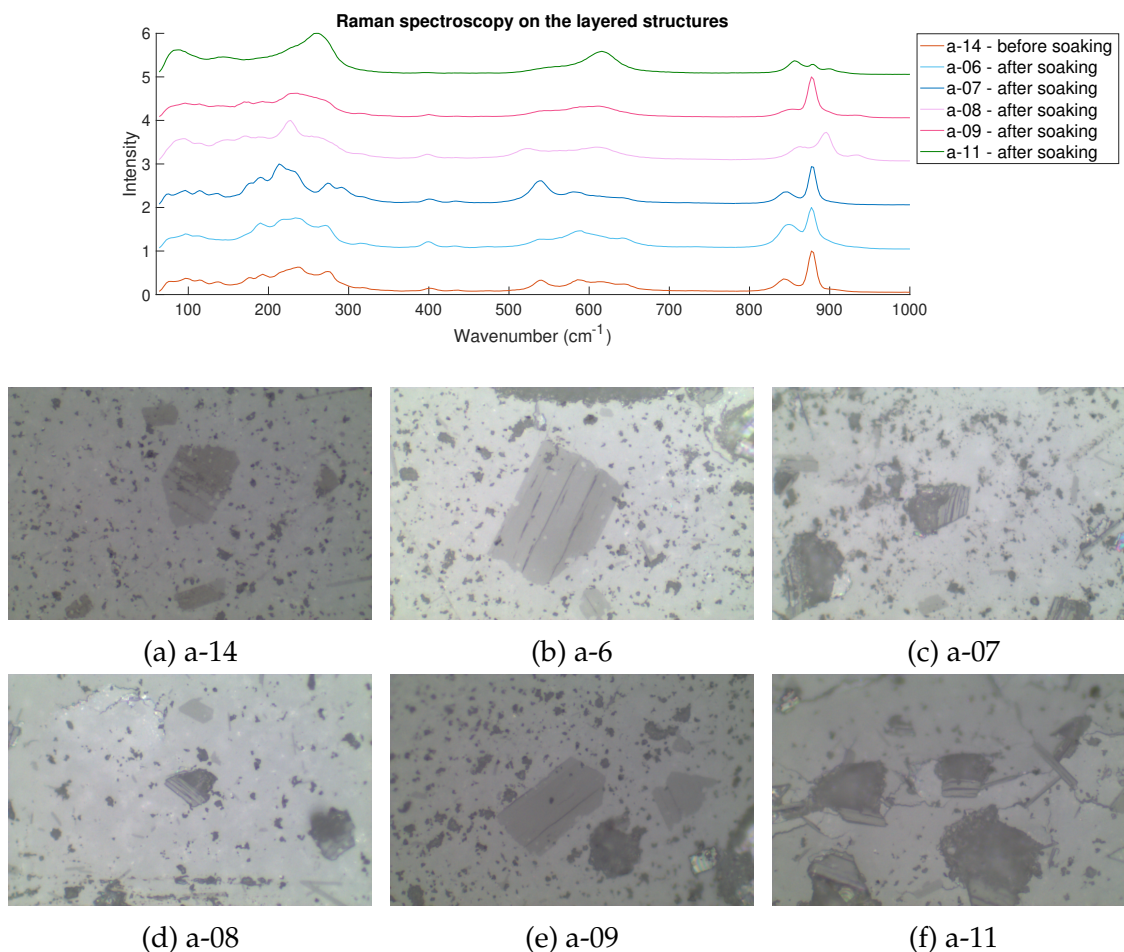
Figure 4.6: Raman spectroscopy of the layered structure before and after soaking in different liquids (top) and their visual aspect (bottom).

4.3.3 Shiny structures

Another structure appearing after soaking is one presenting a shiny color. Their amount was not constant as they were more present on the samples from batch a. They were visible before measurement and as can be seen in Figure 4.7, they present a variety of aspects and spectra. Three out of the four samples presented on the left graph exhibited a clear cubic shape that seems to be on top of a dark area. These three spectra present the same general trend of bimodal band around $860\,cm^{-1}$, a peak at $400\,cm^{-1}$ and several peaks in between $100\text{-}300\,cm^{-1}$. In other cases, the difference in aspect was less highlighted and this is also translated by Raman spectra being similar to KNN. The only visible difference is, in some cases, the presence of a Raman peak located around $138\,cm^{-1}$ according to the samples (Figure 4.7, samples b-05 and b-11).

(a) a-06   (b) a-07   (c) a-08   (d) a-09

(e) b-03   (f) b-08   (g) b-11   (h) c-08

(i) c-08
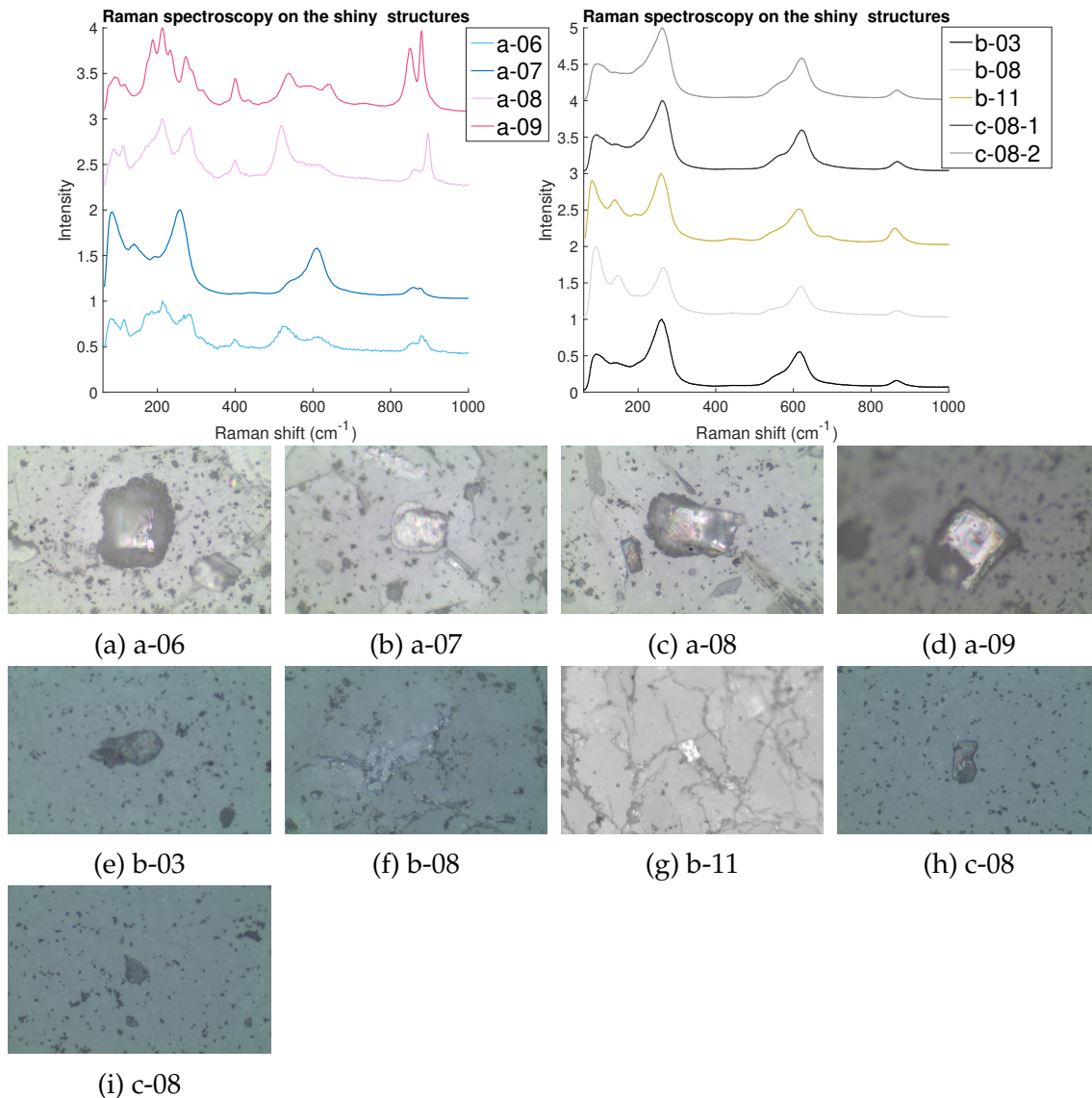
Figure 4.7: Raman spectroscopy of the shiny structures after soaking in all the different soaking conditions (top) and their corresponding visual aspect (bottom).

4.3.4 Soaking effect

Some structures were not visible before soaking but well after. Their Raman spectra are presented in Figures 4.8, 4.9 and 4.10. As these Figures highlight, the majority of the new structures are large and black spots, with mainly unchanged spectra compared to KNN.

One spot, located on a sample soaked in ultra-pure water, presented a different spectrum than the one of KNN, and was located next to a sheet-like structure. This behavior of dark area appearing next to a sheet-like structure was observed

on several samples.

(a) a-06 (b) a-08-1 (c) a-08-2 (d) c-01
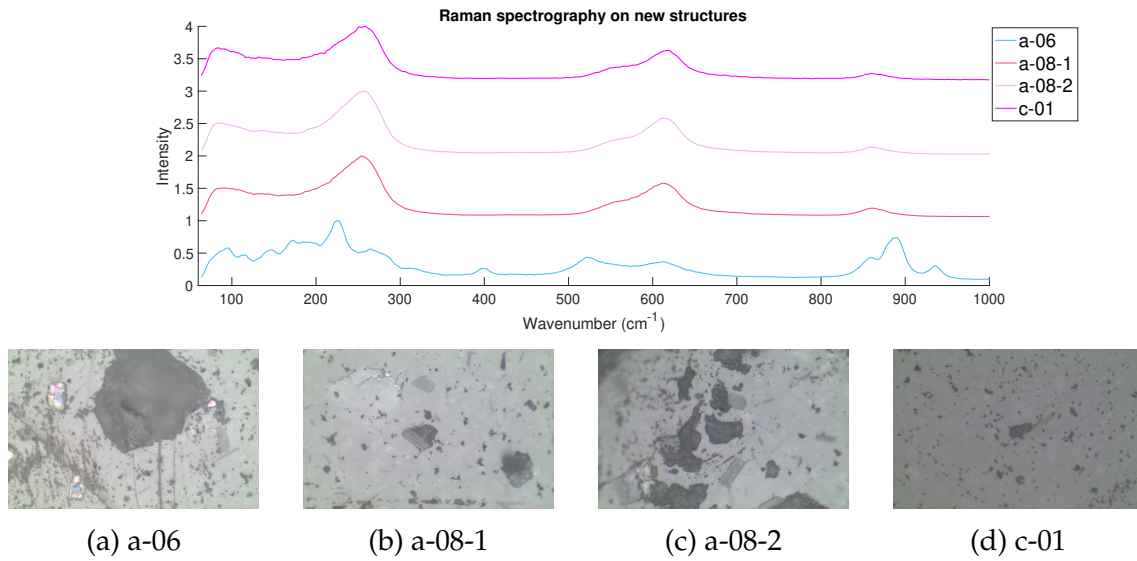
Figure 4.8: Raman spectroscopy of the structures appearing after soaking in ultra-pure water and deionized water (top) and their corresponding visual aspect (bottom).

(a) a-10 (b) b-03 (c) b-04-1 (d) b-04-2

(e) c-11
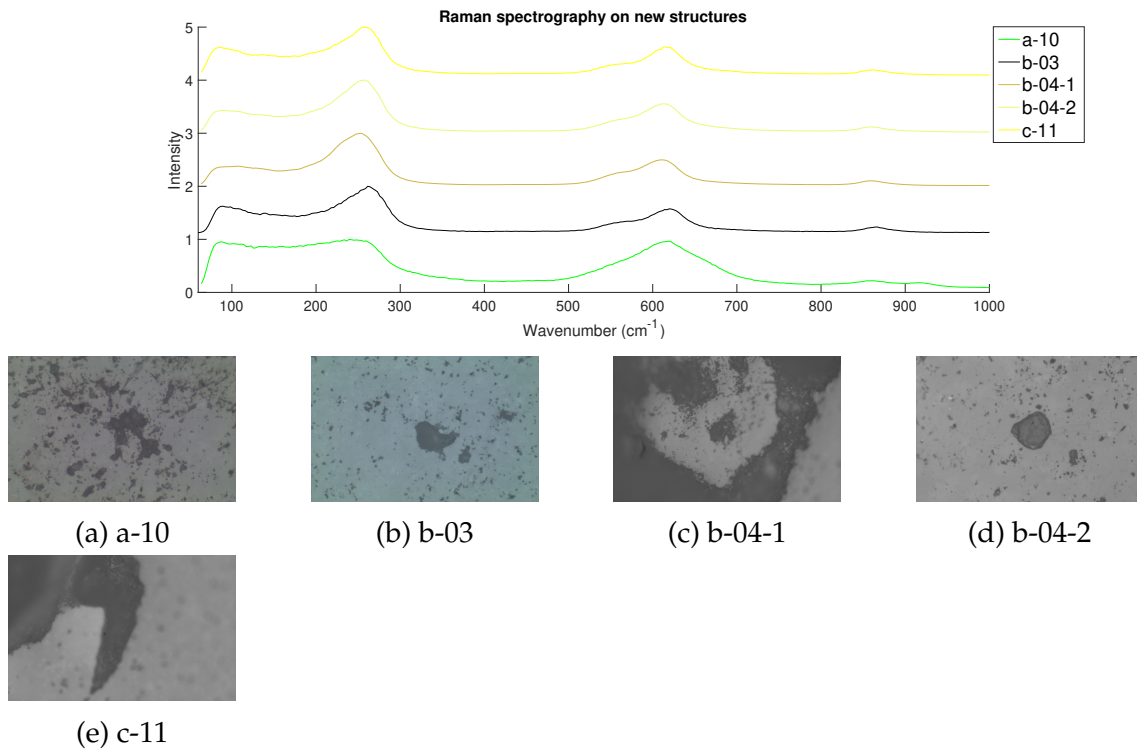
Figure 4.9: Raman spectroscopy of the structures appearing after soaking in saline solution for 6, 12 and 72h (top) and their corresponding visual aspect (bottom).

(a) b-06   (b) c-09-1   (c) c-09-2   (d) c-10-1

(e) c-10-2
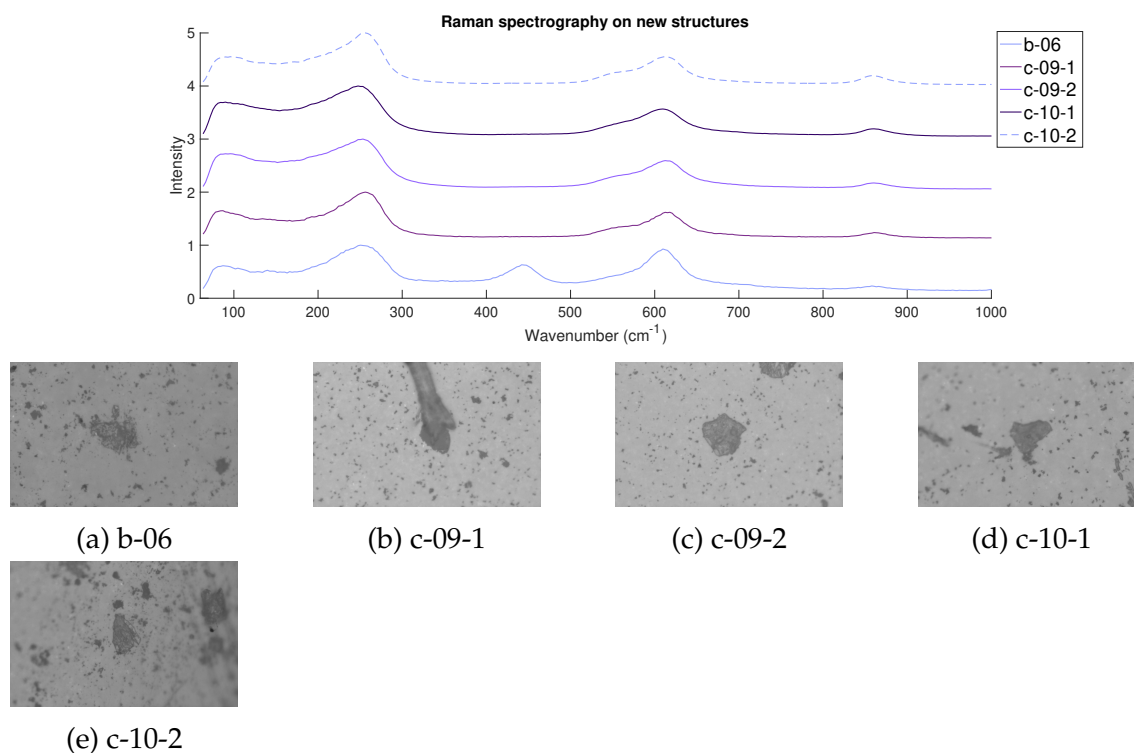
Figure 4.10: Raman spectroscopy of the structures appearing after soaking in saline solution for 24h (top) and their corresponding visual aspect (bottom).

4.3.5 Unchanged structures

The last structures highlighted with the Raman spectroscopy are the small, evenly distributed black spots with different shapes. They were already visible before soaking. Their spectra are presented in Figures 4.11 and 4.12. The main observation is that these structures either present a similar spectrum to KNN or small modifications, mainly a new peak around 400 cm^{-1} and sometimes a bimodal around 860 cm^{-1}. Overall, the visual characteristics are preserved.

(a) a-09   (b) c-02   (c) c-05   (d) b-04   (e) b-11

(f) c-11
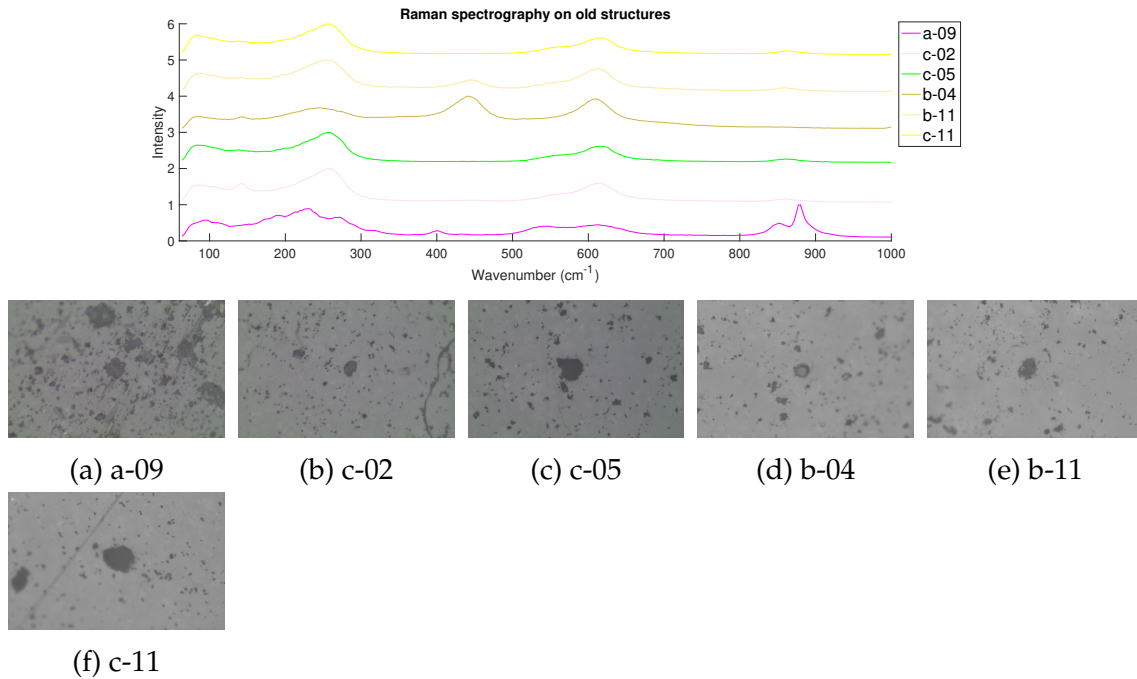
Figure 4.11: Raman spectroscopy after soaking in deionized water and saline solution (12 and 72h) of the structures already present before soaking (top) and their corresponding visual aspects (bottom).

(a) b-08-1   (b) b-08-2   (c) c-03   (d) b-06-1   (e) b-06-2
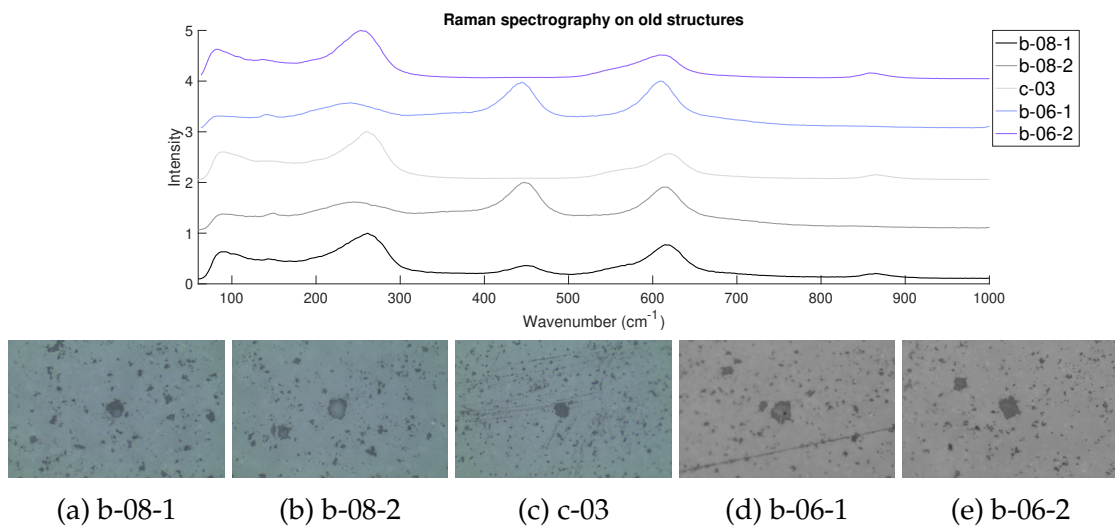
Figure 4.12: Raman spectroscopy after soaking in saline solution (6 and 24h) of the structures already present before soaking (top) and their corresponding visual aspects (bottom).

4.4 Bulk XRD

4.4.1 Calcination and sintering

The XRD pattern of the three batches after calcination are presented in Figure 4.13. It can be seen that the spectra don't correspond to stoichiometric KNN but are all more close to a stoichiometry with a lack of sodium (PDF 01-085-2528). However the remaining peak can be attributed to $NaNbO_3$ (PDF 04-023-1697). In batch c, some $K_2Nb_4O_{11}$ are found especially around $2\theta < 30°$ (PDF 00-031-1059).

During sintering, a lot of changes occurred. These are observable in Figure 4.14. Stoichiometric KNN can be noticed in batches b and c (PDF 00-061-0315). In batch a, the pattern presents a shift compared to the stoichiometric KNN, sometimes to the right sometimes to the left according to the peaks. Batch c also presents some secondary phases that can be attributed to $K_2Nb_4O_{11}$.
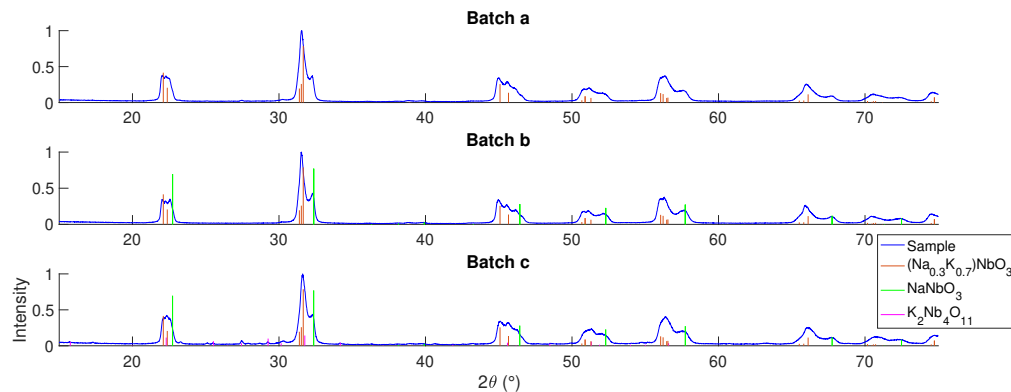
Figure 4.13: XRD patterns after calcination.
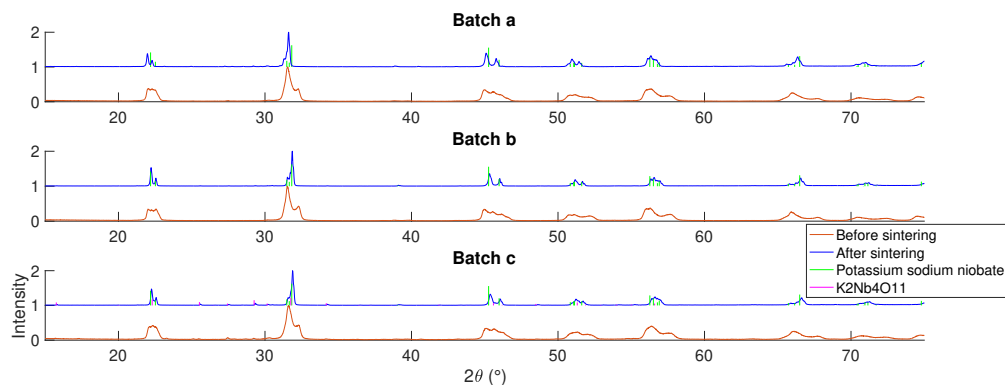
Figure 4.14: XRD patterns after sintering.

4.4.2 After 12h soaking

Figure 4.15a compares an unsoaked sample with 4 samples soaked in ultra-pure water. All the peaks were scaled based on the maximum value. Figures 4.15b and 4.15c expose the patterns for respectively deionized water and saline solution.

After soaking in ultra-pure water, a slight shifting can be observed. Sample a-06, which underwent XRD before and after soaking, presents a shifting to the right. Peaks corresponding to the crystal planes (100) and (200), (110) and (210) are shifted by 0.23°; peaks for the crystal planes (020) and (201) by 0.20° and finally the one for the crystal plane (121) is shifted by 0.18°. The same behavior can be observed for samples a-04 and a-07 after soaking, compared to KNN-a-06 before soaking except that the values are not exactly the same, although they all share the same order of magnitude. Sample KNN-a-05 presented a deviating behavior after soaking: the peak corresponding to the crystal plane (100) is almost not present anymore. The other peaks are shifted to the left by higher values than for the other samples. The intensities in the measurements of this sample are also non constant: the intensity of the peak (211), located at $2\theta \simeq 56°$ increases and becomes comparable to the one of crystal plane (121).

After soaking in ultra-pure water the only new behavior is observed on sample c-01. The peaks are broader on this sample that they are on any other one.

The soaking in saline solution didn't present any modification of the crystal structure as all the spectra are constant. This observation is valid for all the other soaking conditions as shown in Figure 4.16.
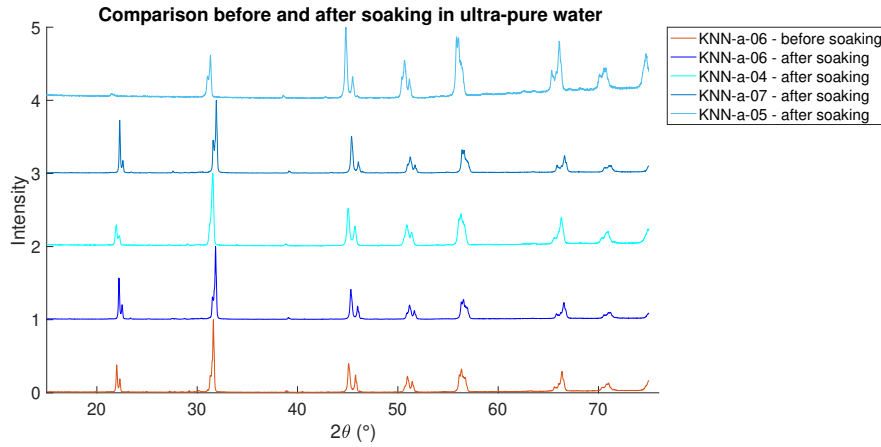
(a) 12h soaking in ultra-pure water
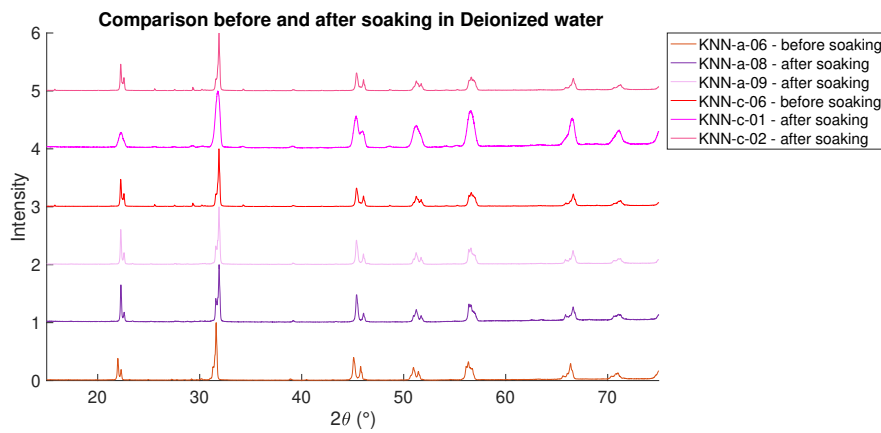
(b) 12h soaking in deionized water
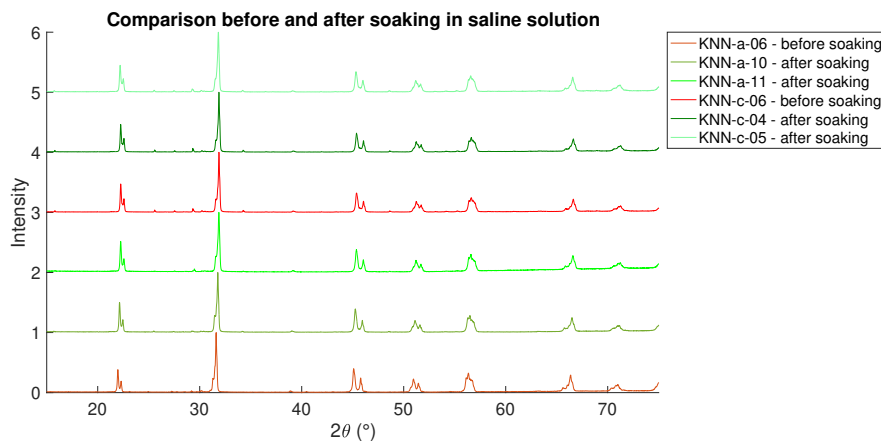
(c) 12h soaking in saline solution

Figure 4.15: XRD patterns comparing samples soaked 12h in different liquids with unsoaked samples.
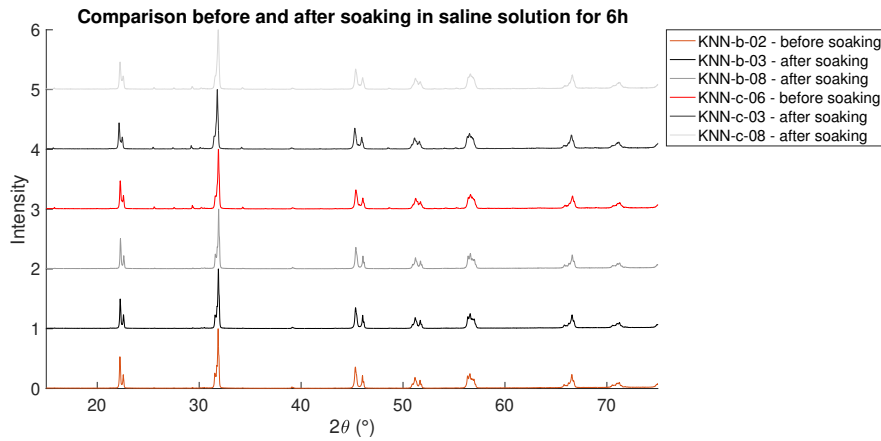
(a) 6h soaking in saline solution
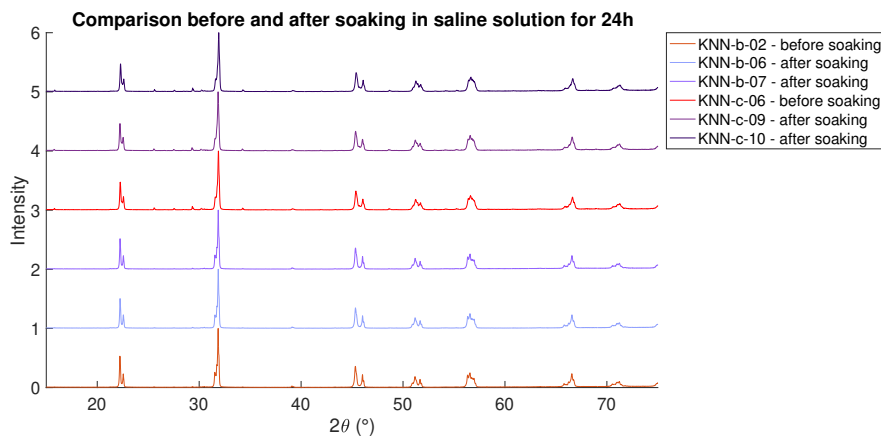
(b) 24h soaking in saline solution
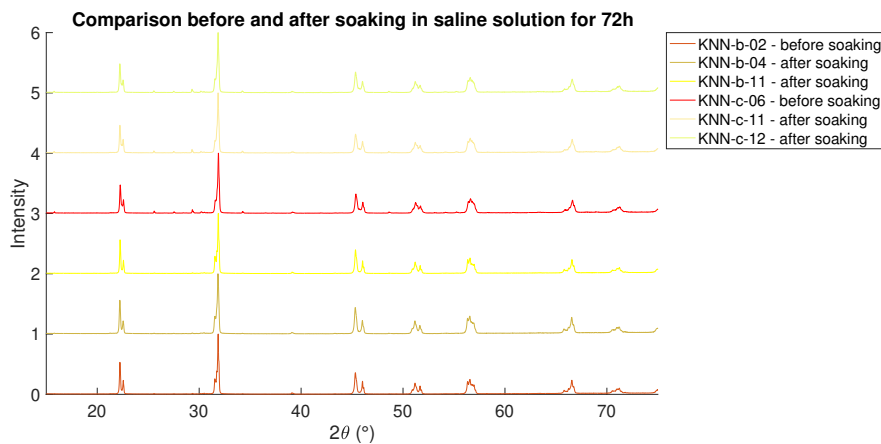
(c) 72h soaking in saline solution

Figure 4.16: XRD patterns comparing samples soaked in saline solution for different times with unsoaked samples.

4.5   Grazing incident XRD

4.5.1   After 12h soaking

Figure 4.17 compares the GIXRD results of unsoaked with soaked samples in the different solutions. Half of the samples were analyzed by this method and the results are presented in this section.

A first and general observation is the smoothness of all the curves. The noise is not too present. On unsoaked samples this translates the efficiency of the polishing to a quarter of a micron. On soaked samples this can be interpreted as a modest modification of surface roughness. An important factor to highlight is the presence of the peak corresponding to the crystal plane (100) for the sample a-05. As presented in the previous section, this peak could not be observed on the XRD pattern.

After soaking in ultra-pure water, no difference was observed. All the peaks present before soaking are still there, at the same position and with the same relative intensity compared with one another.

Soaking in deionized water also didn't deeply modify the sample. No difference could be highlighted except for the sample from batch c that presented an unwanted peak at $2\theta = 47°$ (after the bimodal peak located at $2\theta = 45°$). This peak isn't present on the sample after soaking and is therefore supposed to be a secondary phase.

The observations for Figure 4.17c representing the comparison before and after soaking in saline solution are the same as the one for soaking in deionized water: no difference is highlighted and the extra peak present for the sample from batch c isn't present on the sample after soaking. The same goes for the 24- and 72-hour soaking in saline solution.

The only sample presenting a different behavior is c-03, presented in Figure 4.18a. The peaks are still well represented but the noise is higher.
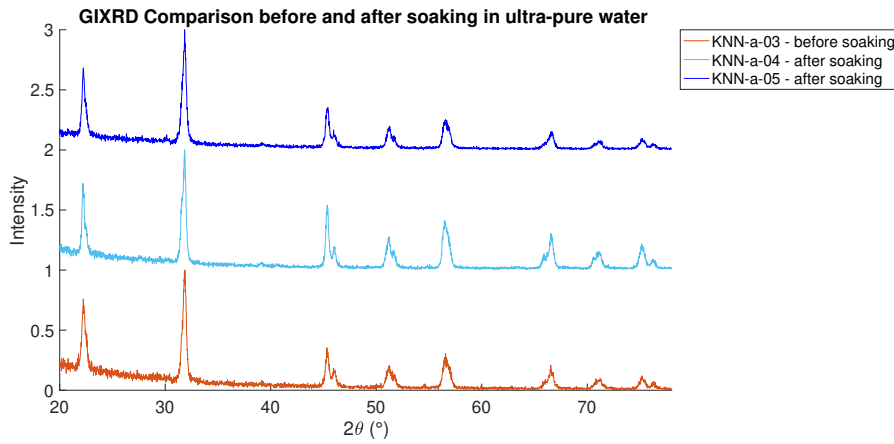
(a) 12h soaking in ultra-pure water.
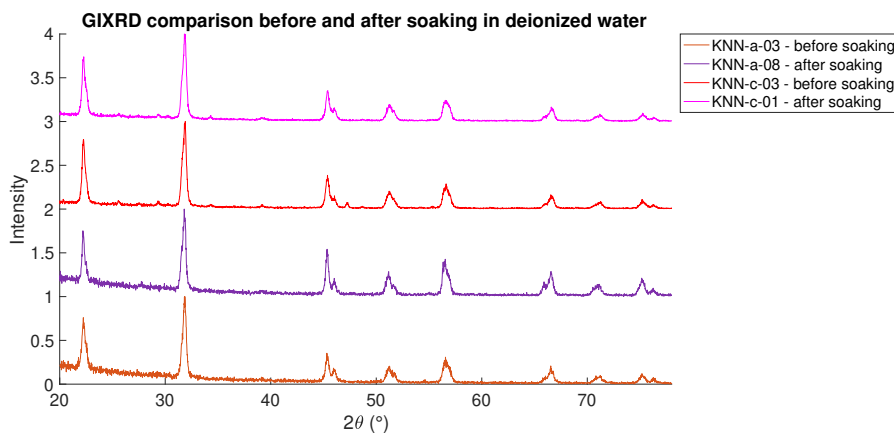
(b) 12h soaking in deionized water.
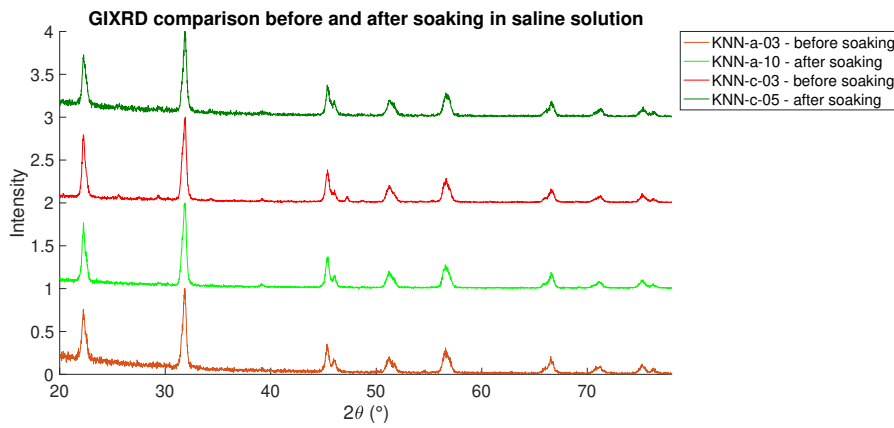
(c) 12h soaking in saline solution.

Figure 4.17: GIXRD patterns comparing samples soaked for 12h in different liquids with unsoaked samples.

4.5.2 Soaking in saline solution for different times
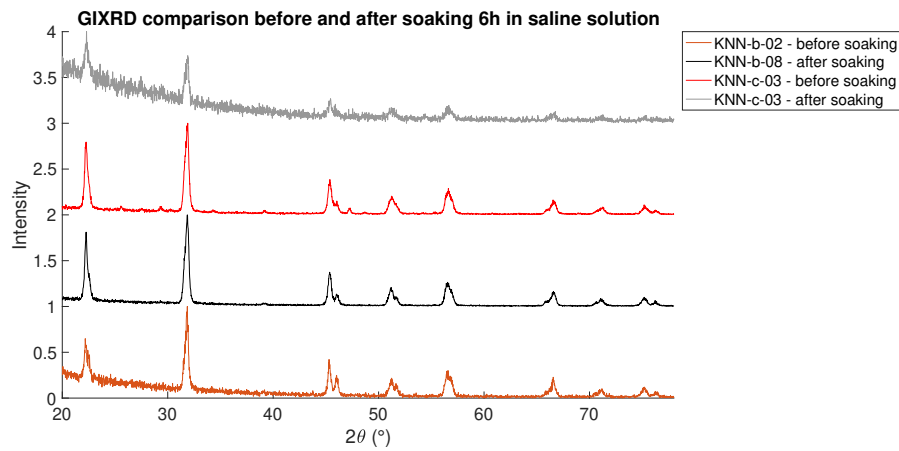
(a) 6h soaking in saline solution.
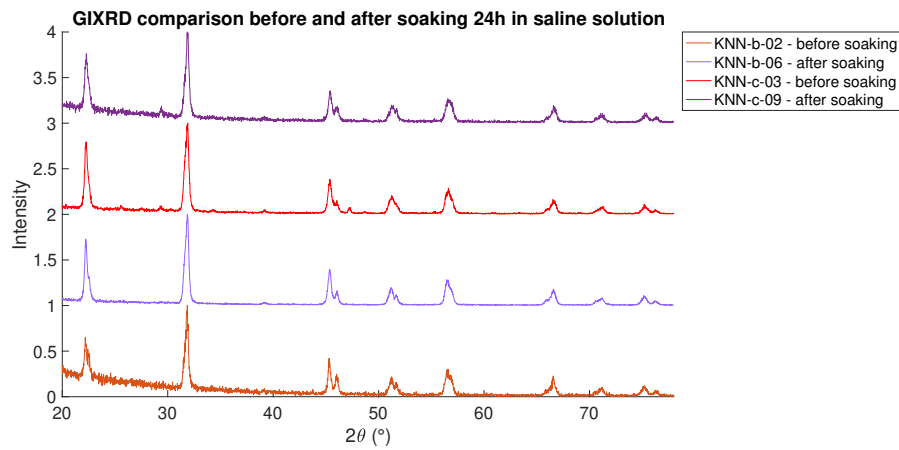
(b) 24h soaking in saline solution.
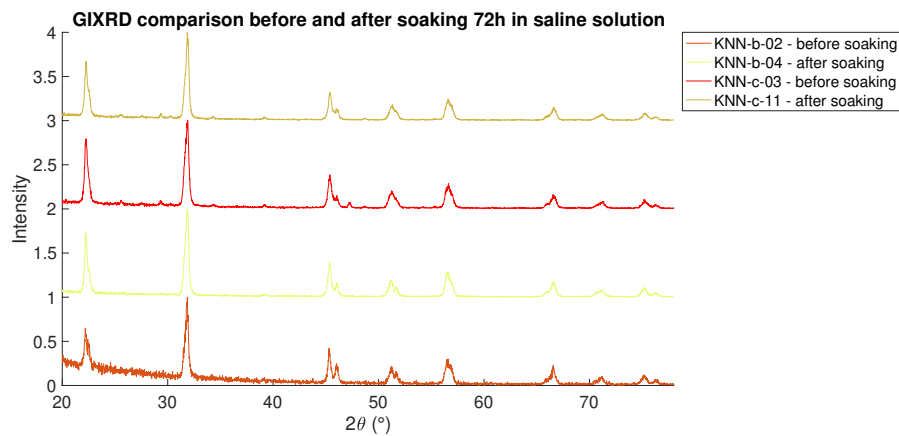
(c) 72h soaking in saline solution.

Figure 4.18: GIXRD patterns comparing samples soaked in saline solution for different times with unsoaked samples.

4.6 Nanoindentation

Nanoindentation was performed on every sample before and after soaking. After soaking different types of structures were analyzed based on what could be observed. The indent was taken in the middle of the picture presented with the measurements.

4.6.1 After 12h soaking

Figure 4.19 presents the curves obtained with the nanoindenter on a sample from batch a soaked in ultra-pure water. The curves from the other sample are given in Appendix D.1 as they present a similar behavior. Figure 4.19 highlights the fact that the different spots that can be found on the surface present different mechanical properties. For a same load they underwent a larger displacement by one order of magnitude for some and by two orders for other. The load-displacement curve before and after soaking measured on the normal-looking surface seem comparable. However, when looking at the corresponding hardness, plotted in Figure 4.20a, all the values are in the lower end. The three other samples present a clear decrease in hardness with the majority of the different surfaces leading to a lower hardness by orders of magnitude.

For the soaking in deionized water, the samples presented different behavior depending on whether they originated from batch a or c. In batch a, a lot of these different structures could be seen. In Figure 4.21 these structures presented larger displacements for a given load compared to before soaking. Samples from batch c, however, exhibited normal-looking surfaces and the only defect that could be found didn't show any significant difference in displacement; this is shown in Figure 4.22 for one sample while the data for the second sample is presented in Appendix D.9. The evolution of the hardness is presented in Figure 4.20b. As for the soaking in ultra-pure water, the different structures on the surface of samples from the first batch presented a low hardness. Two samples, one from batch a and one from batch c, present a clear modification of the hardness upon soaking, a decrease for the former, and an increase for the latter. However for the two other samples no clear conclusion can be drawn.

In saline solution, the behavior was considerably more stable. Less different structures could be seen on the surface, both for samples from batch a and from batch c. Figure 4.23 presents curves for a sample from batch a soaked 12h in saline solution, while the data for the three other samples are presented in Appendix D.5, D.10 and D.11 as they all present the same behavior. In terms of hardness, the two samples from batch c couldn't be measured before soaking due to technical difficulties; the two samples from batch a present a general decrease in hardness.
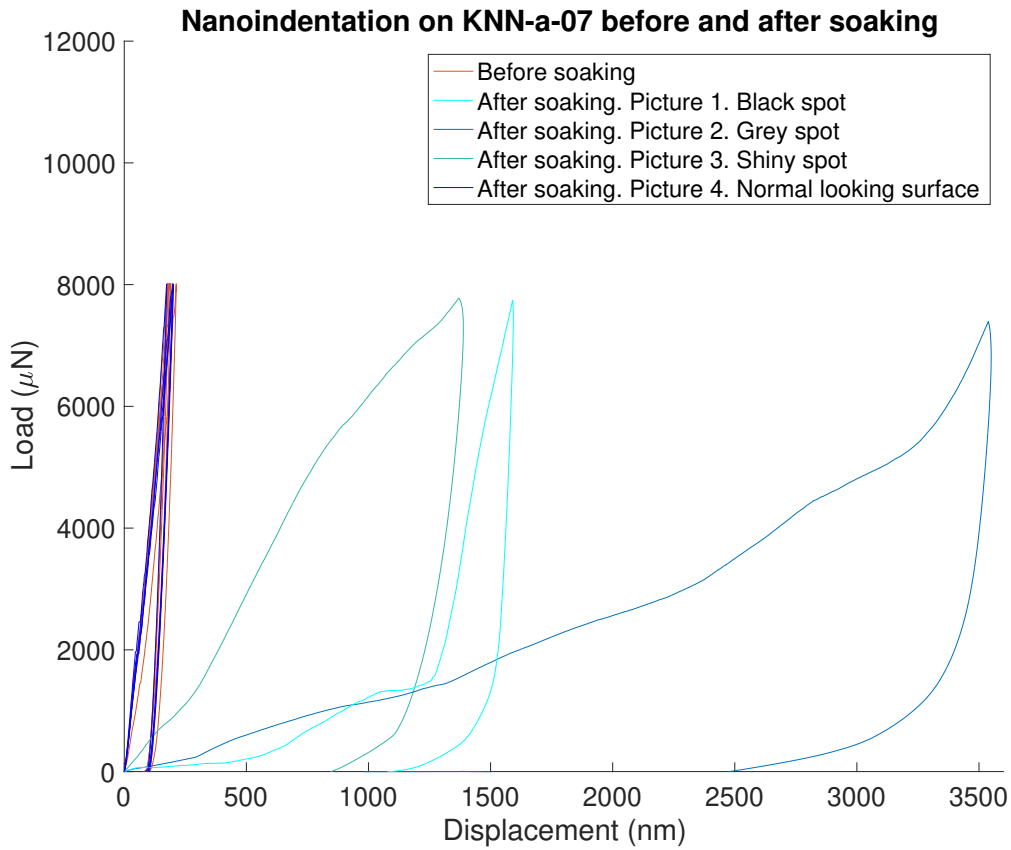
(a) Nanoindendation curves. A zoom of the area corresponding to a displacement of 140-220 nm is presented in Appendix D.2
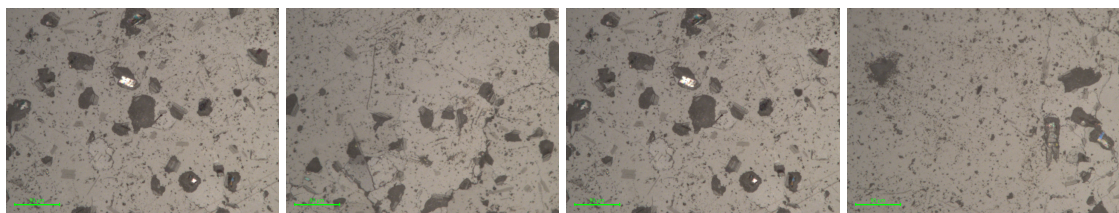
(b) Black spots. Picture 1

(c) Gray spots. Picture 2

(d) Shiny spots. Picture 3.

(e) Normal looking surface. Picture 4

Figure 4.19: Nanoindentation on a sample soaked for 12h in ultra-pure water and the corresponding pictures of the surface. The indent was taken in the middle of the picture, except for picture 4 where it was taken on the shiny surface.
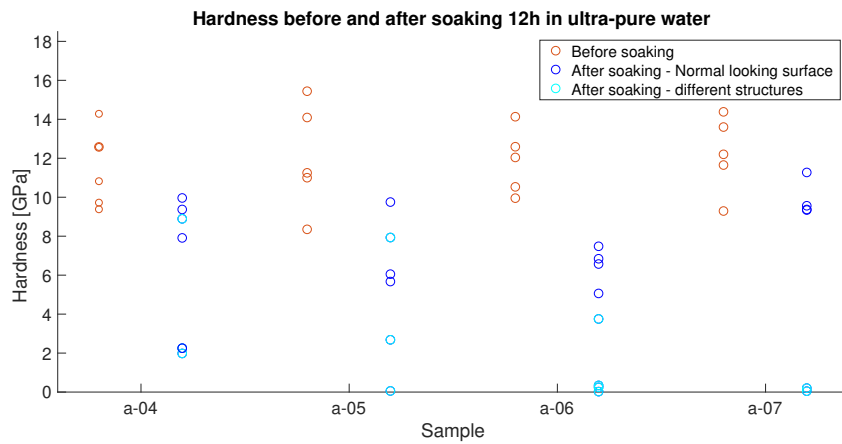
(a) Ultra-pure water.

(b) Deionized water.
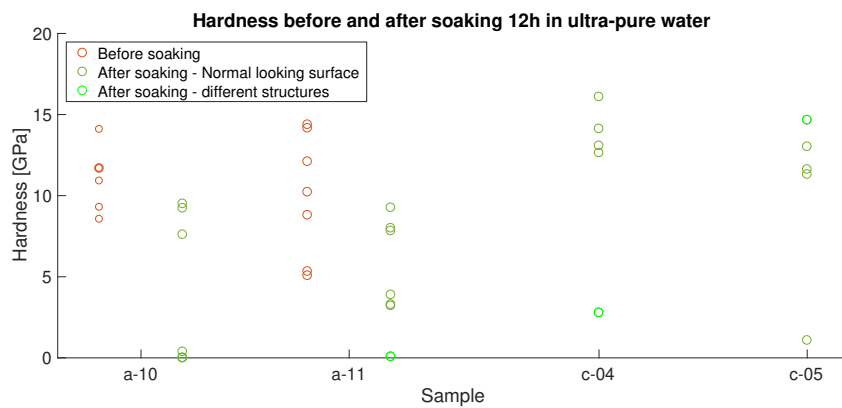
(c) Saline solution.

Figure 4.20: Comparison of the hardness obtained through nanoidentation before and after soaking for 12h in different solutions.
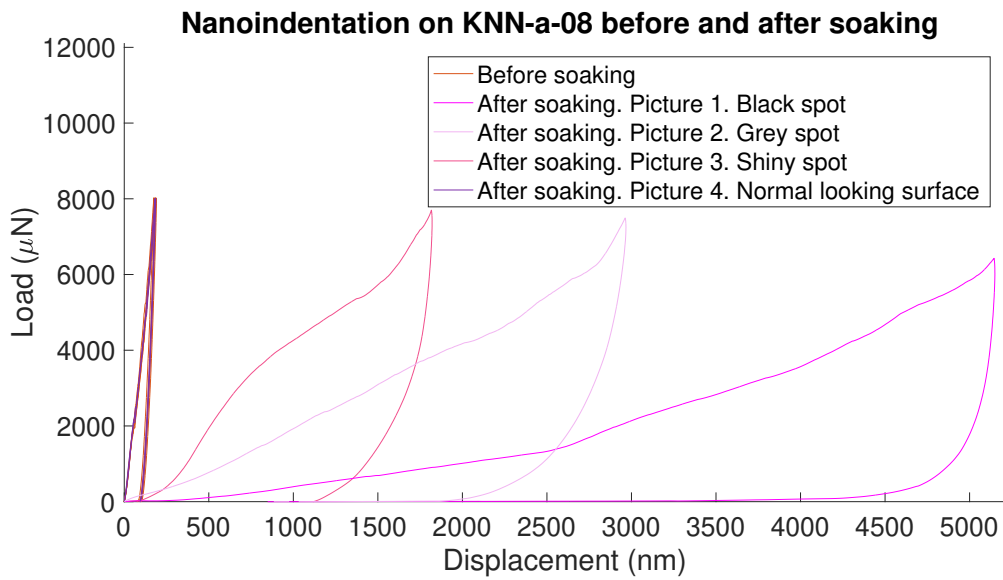
(a) Nanoindendation curves. A zoom of the area corresponding to a displacement of 140-220 nm is presented in Appendix D.3
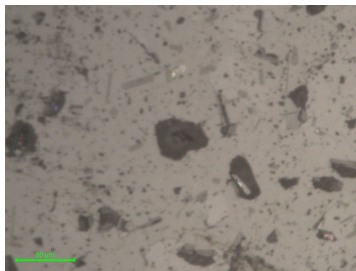
(b) Black spots. Picture 1
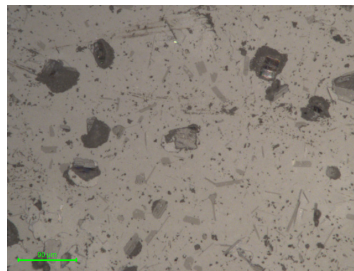
(c) Grey spots. Picture 2
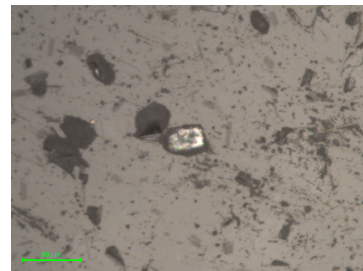
(d) Shiny spots. Picture 3.
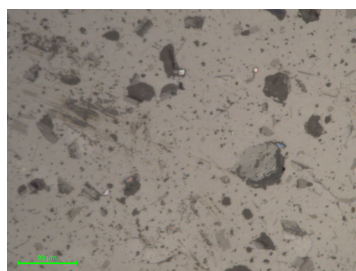
(e) Normal-looking surface spot. Picture 4

Figure 4.21: Nanoindentation on a sample soaked for 12h in deionized water and the corresponding pictures of the surface.
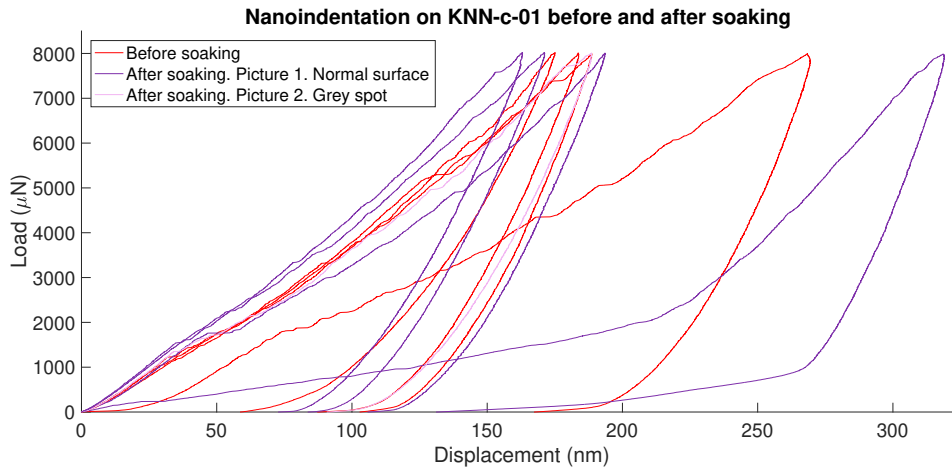
(a) Nanoindendation curves.
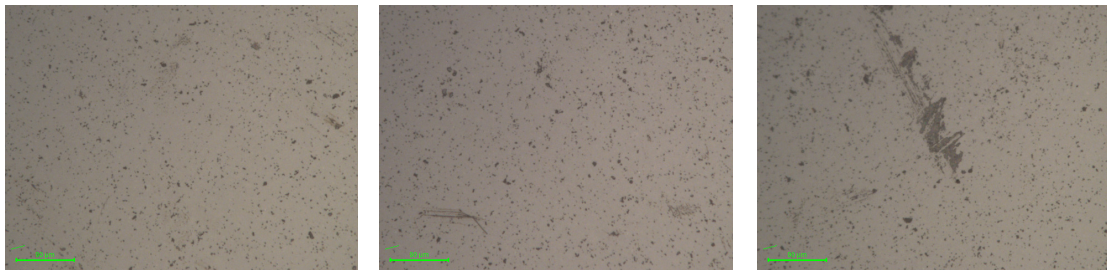
(b) Normal looking surface spot. Picture 1

(c) Grey spots. Picture 2.

Figure 4.22: Nanoindentation on a sample soaked for 12h in deionized water and the corresponding pictures of the surface.

(a) Nanoindendation curves.
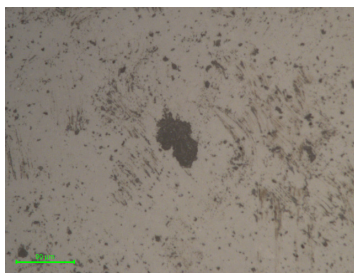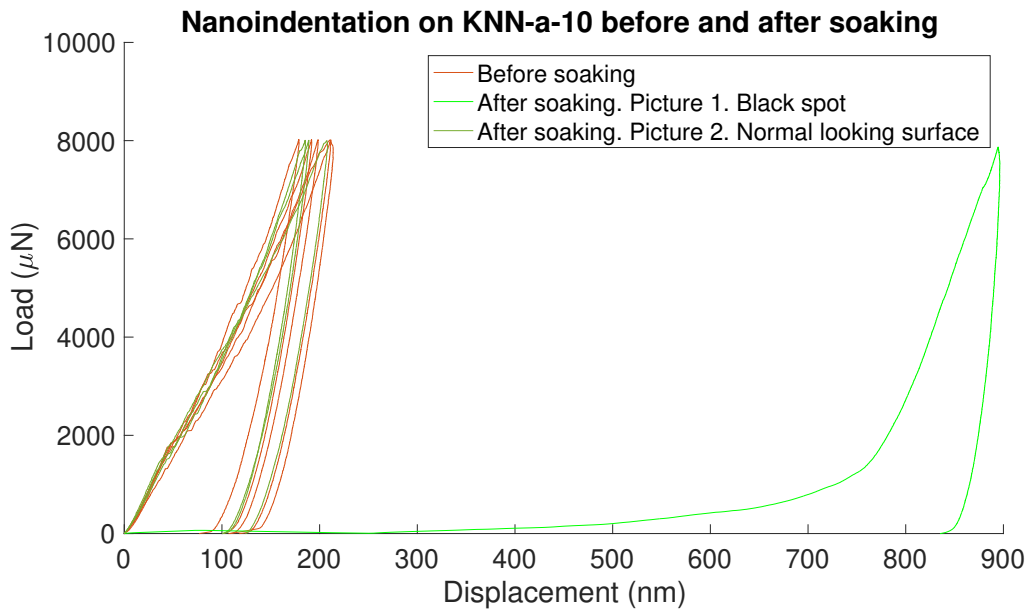
(b) Black spots.
Picture 1
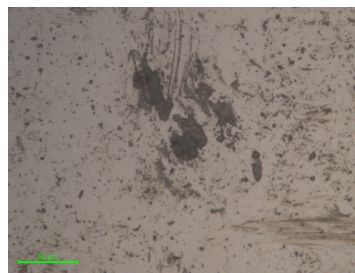
(c) Normal looking surface.
Picture 2

Figure 4.23: Nanoindentation on a sample soaked for 12h in saline solution and the corresponding pictures of the surface. One curve taken on a black spot isn't displayed as the displacement during measurement exceeded the limit of 5000 nm.

4.6.2 After different periods of time in saline solution

After soaking for 6h in saline solution, two samples presented the same behavior as previously presented. One of them is shown in Figure 4.24. As can be seen in this Figure, a dark spot, that seems to have appeared from soaking, presents a clear different mechanical behavior. The displacement corresponding to a given load is different but the shape of the curve too: the displacement continues to increase even during the unloading. The corresponding hardness presented in Figure 4.28a shows a lower hardness for the different surfaces while the other values don't present a clear decrease or increase in hardness. A sample soaked for

6h in saline solution presented a different behavior. As presented in Figure 4.25, all the curves on the normal looking surfaces present an increase in displacement during the unloading. As discussed later, in section 5.4.1, this leads to incorrect measurements of the hardness.

The 24- and 72-hour soaking gave consistent results, one sample from each are presented in Figure 4.26 and 4.27 respectively while the others are provided in the Appendix D.6 and D.12 to D.15. The results are the same as previously observed: only the different structures present a different mechanical behavior.
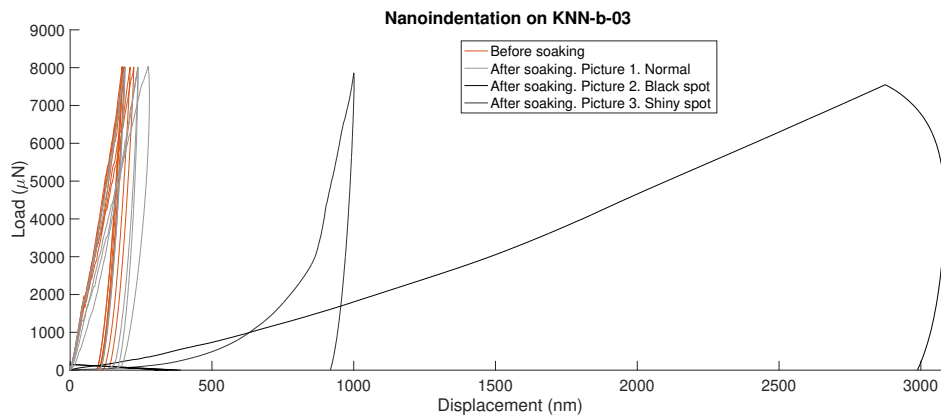
(a) Nanoindendation curves.
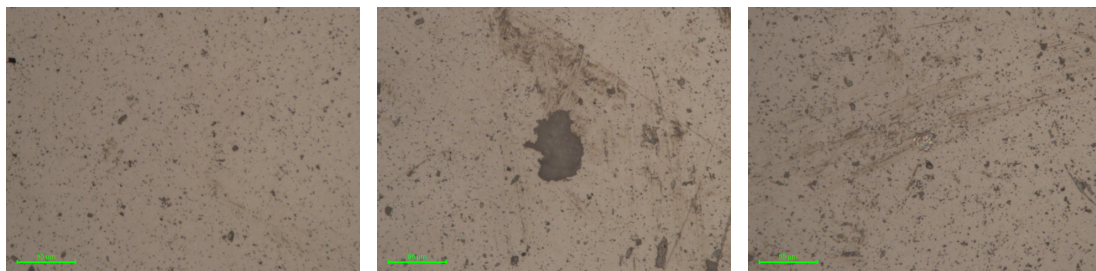
(b) Normal surface. Pic 1   (c) Black spot. Pic 2   (d) Shiny spot. Pic 3

Figure 4.24: Nanoindentation on a sample soaked for 6h in saline solution and the corresponding pictures of the surface.
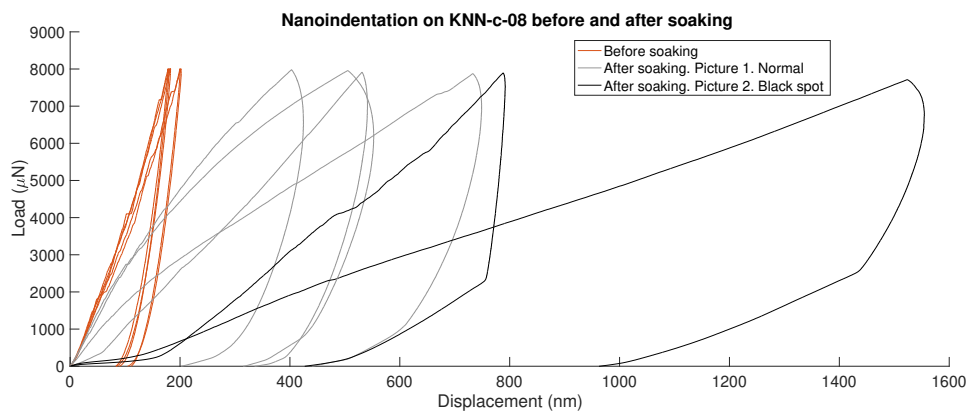
(a) Nanoindendation curves.
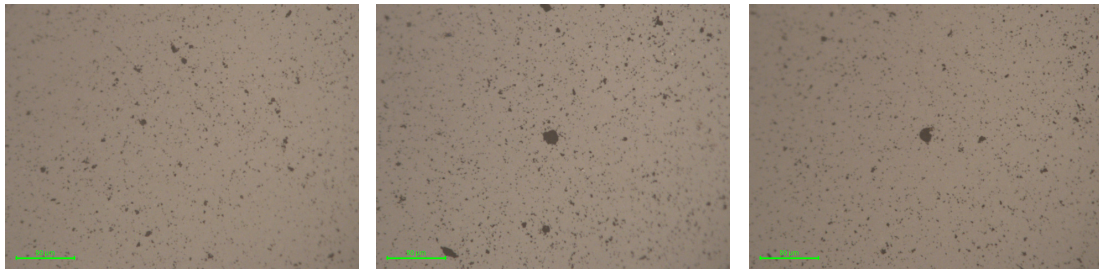
(b) Normal surface. Pic 1

(c) Black spot. Pic 2

Figure 4.25: Nanoindentation on a sample soaked for 6h in Saline solution and the corresponding pictures of the surface.
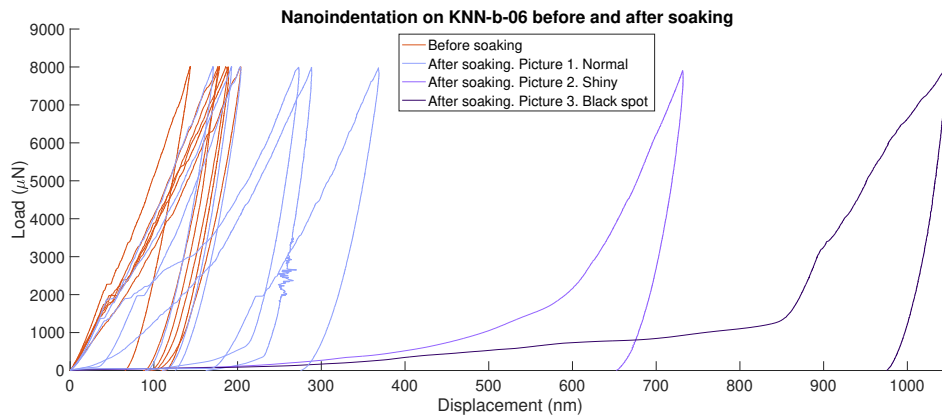
(a) Nanoindendation curves.
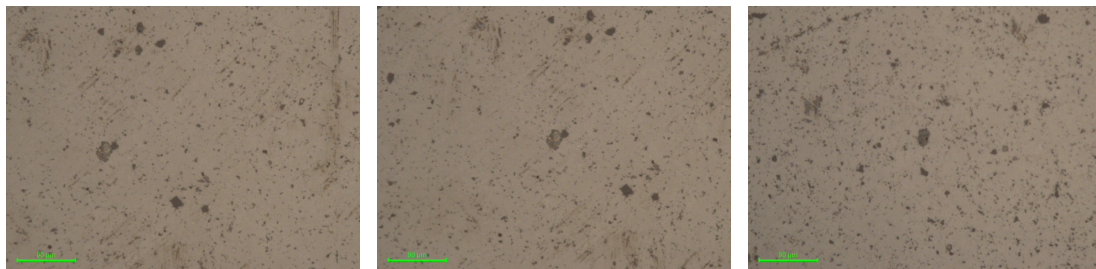
(b) Normal surface. Pic 1   (c) Shiny spot. Pic 2   (d) Black spot. Pic 2

Figure 4.26: Nanoindentation on a sample soaked for 6h in saline solution and the corresponding pictures of the surface.
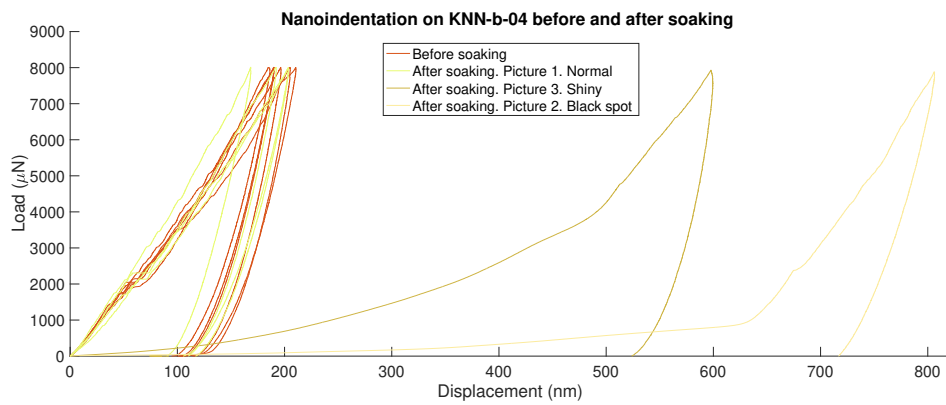
(a) Nanoindendation curves.
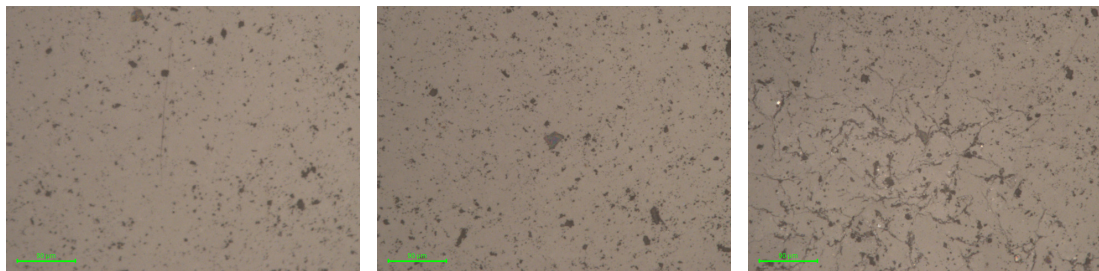
(b) Normal surface. Pic 1   (c) Shiny spot. Pic 2   (d) Black spot. Pic 2

Figure 4.27: Nanoindentation on a sample soaked for 6h in Saline solution and the corresponding pictures of the surface.
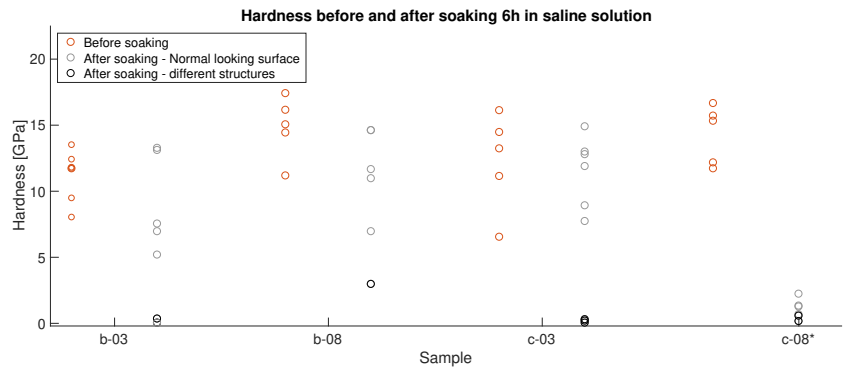
(a) 6h in saline solution for four different samples.
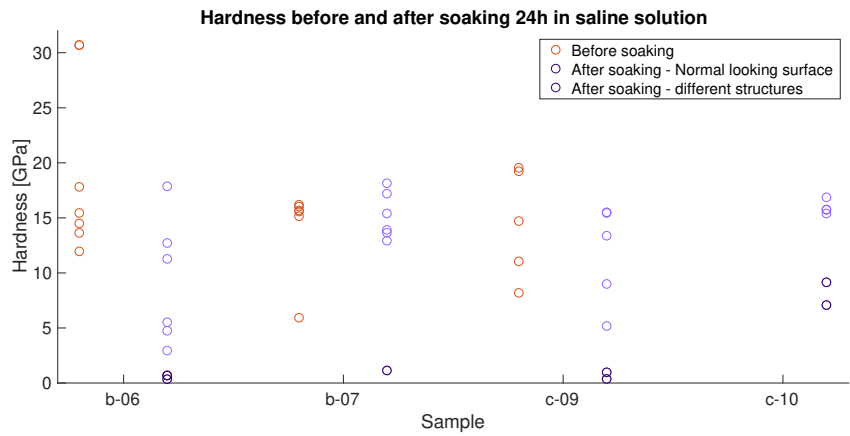
(b) 24h in saline solution for four different samples.
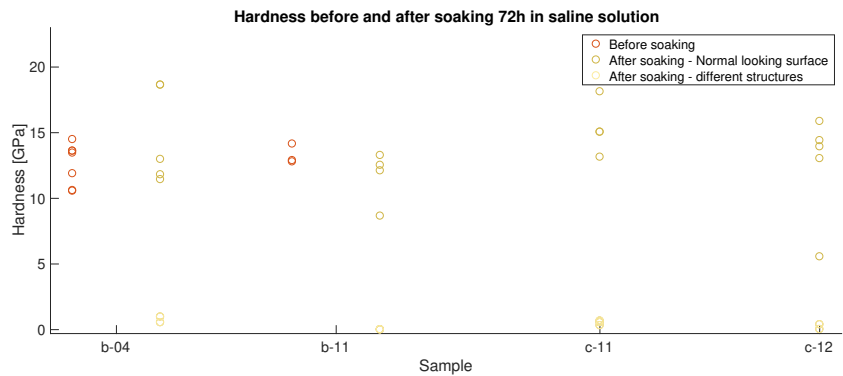
(c) 72h in saline solution for four different samples.

Figure 4.28: Comparison of the hardness obtained through nanoindentation before and after soaking in saline solution for different times. The results from sample c-08 can not be trusted.

4.7 Microindentation

This section presents summarized data. Graphs containing the seven measurements performed on each sample are presented in Appendix E.

4.7.1 Before soaking

The hardness of unsoaked samples was measured on two samples from each batch, with seven indents on each of them. The results, summarized in Table 4.3, show a hardness of 3.2156 Gpa for batch a, 3.2205 GPa for batch b and 4.0190 GPa for batch c. Batch c has then a higher hardness than the first two batches by 0.8GPa. It also has the highest standard deviation with a variation of 4.83% from the mean while it is 4.54% for samples from batch a. Batch b has a mean hardness comparable to the batch a but the lowest standard deviation, with a deviation of 1.93%.

	Mean value [GPa]	Standard deviation [GPa]
Batch a	3.2156	0.1459
Batch b	3.2205	0.0621
Batch c	4.0190	0.1941

Table 4.3: Vickers hardness of unsoaked samples from batches a, b and c.

4.7.2 After 12h soaking

Figure 4.29 presents the evolution of the hardness upon soaking for 12h in different liquids by comparing the results of the Vickers hardness test on the soaked samples with the unsoaked samples from the same batch. It also highlights the standard deviation of the seven indents performed per sample.

After soaking in ultra-pure water, the four samples exhibited a higher standard deviation. This can be linked with the higher heterogeneity that was observable on the samples. The deviation around the mean value equaled 4.66%, 8.10%, 4.98% and 6.44% for samples a-04 to a-07. One of the four samples presented a higher hardness than the values before soaking with a mean value of 3.5915 GPa, which represents an increase of 11.69% compared to before soaking. The three other samples showed a decrease in hardness of 2.08%, 7.07% and 3.64% compared to before soaking.

After soaking in deionized water, samples from batch a presented a higher standard deviation, with a deviation of 7.18% and 7.98%, than the samples from batch c. This, once again, emphasizes the observable heterogeneity on the samples. In samples from batch c, the deviation is lower than before soaking, with 3.04% and

2.23%. In terms of values of hardness, one sample from batch a showed an increase of 6.02% and one exhibited a decrease of 10.02%. In batch c, one sample showed an increase of 1.22%; but this increase is not significant as the average value for the soaked sample in comprised between the averages from the two samples measured. The second soaked sample revealed a decrease of 3.26%.

After soaking in saline solution the general trend is an increase of the hardness. For samples from batch a the increase is of 20.23% and 15.69% while it is lower for the samples from batch c with an increase of 3.84% and 4.59%. All the samples present a low standard deviation, around 3.3% and even 1.29% for one sample.
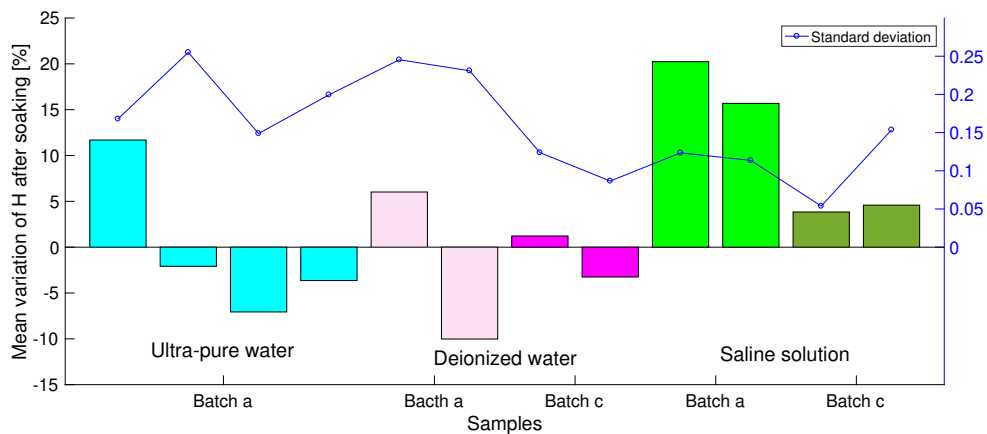
Figure 4.29: Variation and standard deviation of the hardness in comparison with unsoaked samples in different liquids.

4.7.3   After different periods of time in saline solution

Figure 4.30 presents the same evolution of the hardness but upon soaking in saline solution for different times. One may notice that the results for the 12-hour soaking, already presented in the previous section, are reproduced in this Figure. This is to gather all the data for the soaking in saline solution.
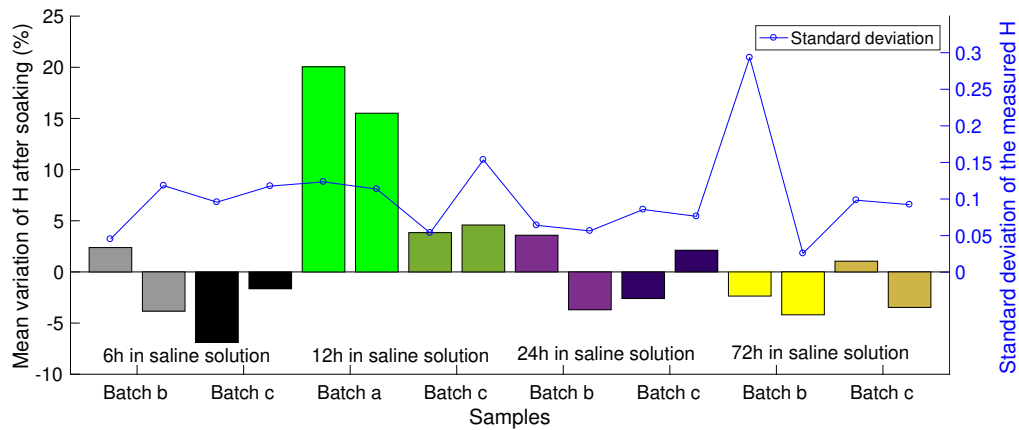
Figure 4.30: Variation and standard deviation of the hardness upon soaking in different times in saline solution.

The standard deviation is quite constant among the different samples, except for one sample where an extreme value was obtained.

The 6-hour soaking led to a decrease in hardness of 3.83%, 6.89% and 1.64% for three samples and an increase of 2.38% for the fourth sample. The 24-hour soaking led to more compact results: the samples from batch b presented respectively an increase of 3.58% and a decrease of 3.70%. The same behavior can be observed in samples from batch c with an increase in hardness of 2.11% and a decrease of 2.60%. Finally the longest soaking lead to a decrease of 2.36%, 4.19% and 3.74% while the last sample presented a slight increase in hardness of 1.05%.

4.8 SEM/EDX

SEM images of samples before and after soaking were taken and will be presented in this section. The EDX measurements and the SEM images from the *NorFab/NTNU NanoLab* were obtained by Caitlin Guzzo as specified in the caption of the relevant figures.

Some low-magnification pictures, presented in Figure 4.31, allowed to compare the general aspect of the surfaces of the samples after soaking. The samples from batch a, soaked in deionized water, presented a different behavior than the other ones: a lot of defects of different sizes and shapes were visible while the other surfaces presented less pores and mainly darker areas.

(a) a-09. 12h in deionized water

(b) b-03. 6h in saline solution

(c) c-08. 6h in saline solution

(d) b-07. 24h in saline solution

(e) c-09. 24h in saline solution
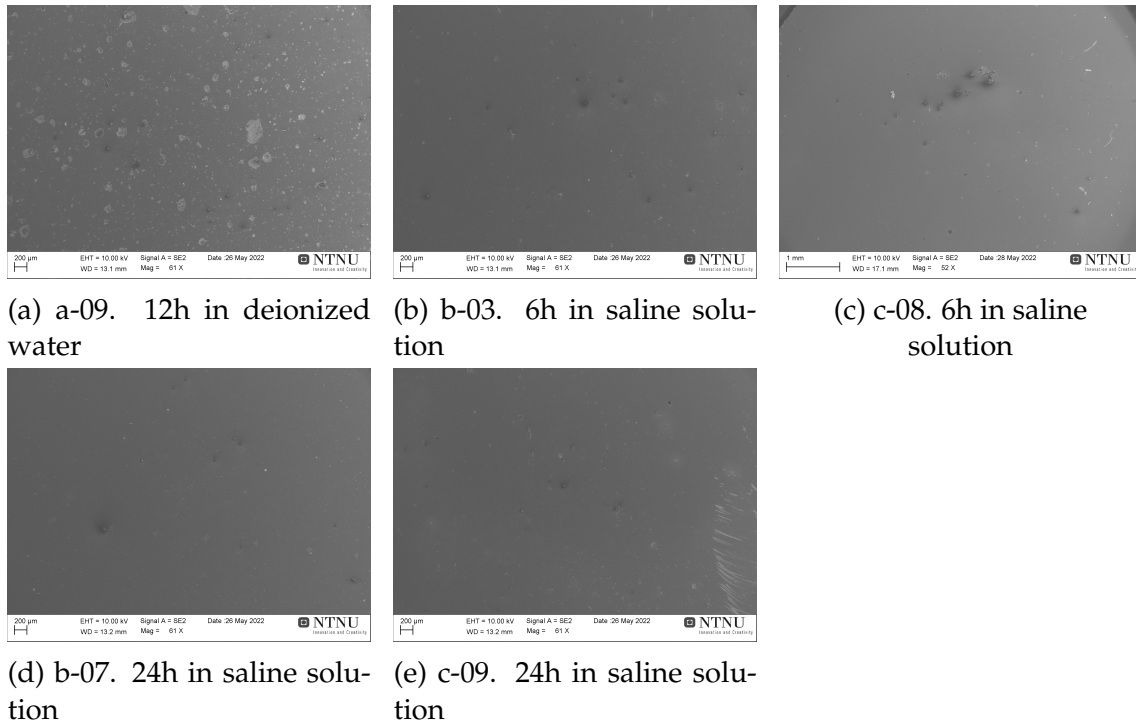
Figure 4.31: Comparison of the surfaces after soaking with SEM.

A slight zoom on samples from batch a allowed to see the general behavior: the surface presents cracks and flakes at several different places. This behavior is visible in Figure 4.32 which displays an image taken with SEM on a sample soaked for 12h in saline solution.
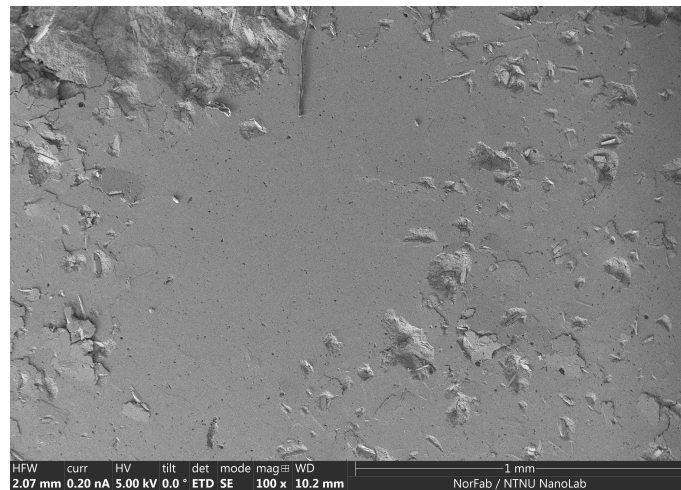
Figure 4.32: SEM image of sample a-11 after soaking for 12h in saline solution. Obtained by Caitlin GUZZO.

Grain sizes can be investigated by comparing SEM results. Figure 4.33 compares

three samples: b-07 and c-01 after soaking and c-06 before soaking. It can be observed that the grains present similar sizes in the order of the micron. Sample c-01 seems however to present slightly smaller grains.

(a) b-07   (b) c-01   (c) c-06
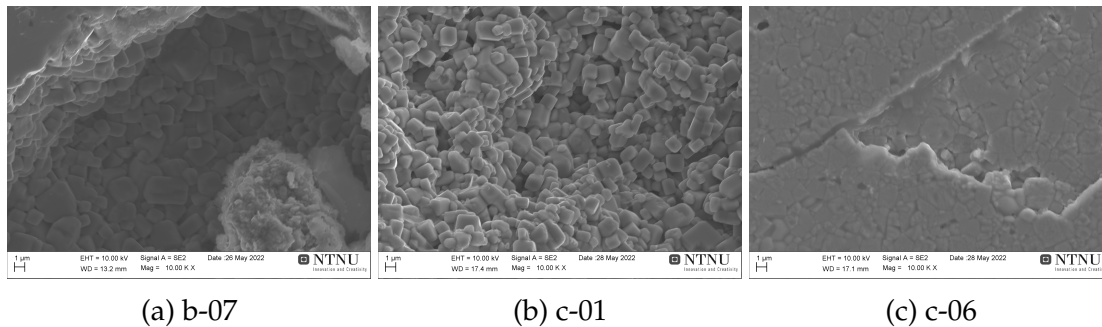
Figure 4.33: SEM comparing the grain sizes on two soaked samples and on a thermally etched one.

An important result is the presence of sheet-like structures, displayed in Figure 4.34a. The EDX map reported that these structures are sodium-deficient compared to the surroundings, without presenting an excess in potassium; niobium and oxygen are also constant. An uncracked grain is visible in the middle of the sheet-like structure and this grain does not present the sodium deficiency. An excess of potassium, without any change for the other elements, can be seen in the south-west corner and is linked to the pores present at this location. This phenomenon of potassium in the pores after soaking is also highlighted in Figure 4.35b and compared to the situation before soaking (Figure 4.35a) where the pores are not filled with an excess of potassium. The latter Figure also shows an entrapped pore, introduced in Section 2.2.5. They are characteristic of abnormal grain growth.

(a) SEM image

(b) EDX map - Potassium

(c) EDX map - Sodium

(d) EDX map - Niobium

(e) EDX map - Oxygen
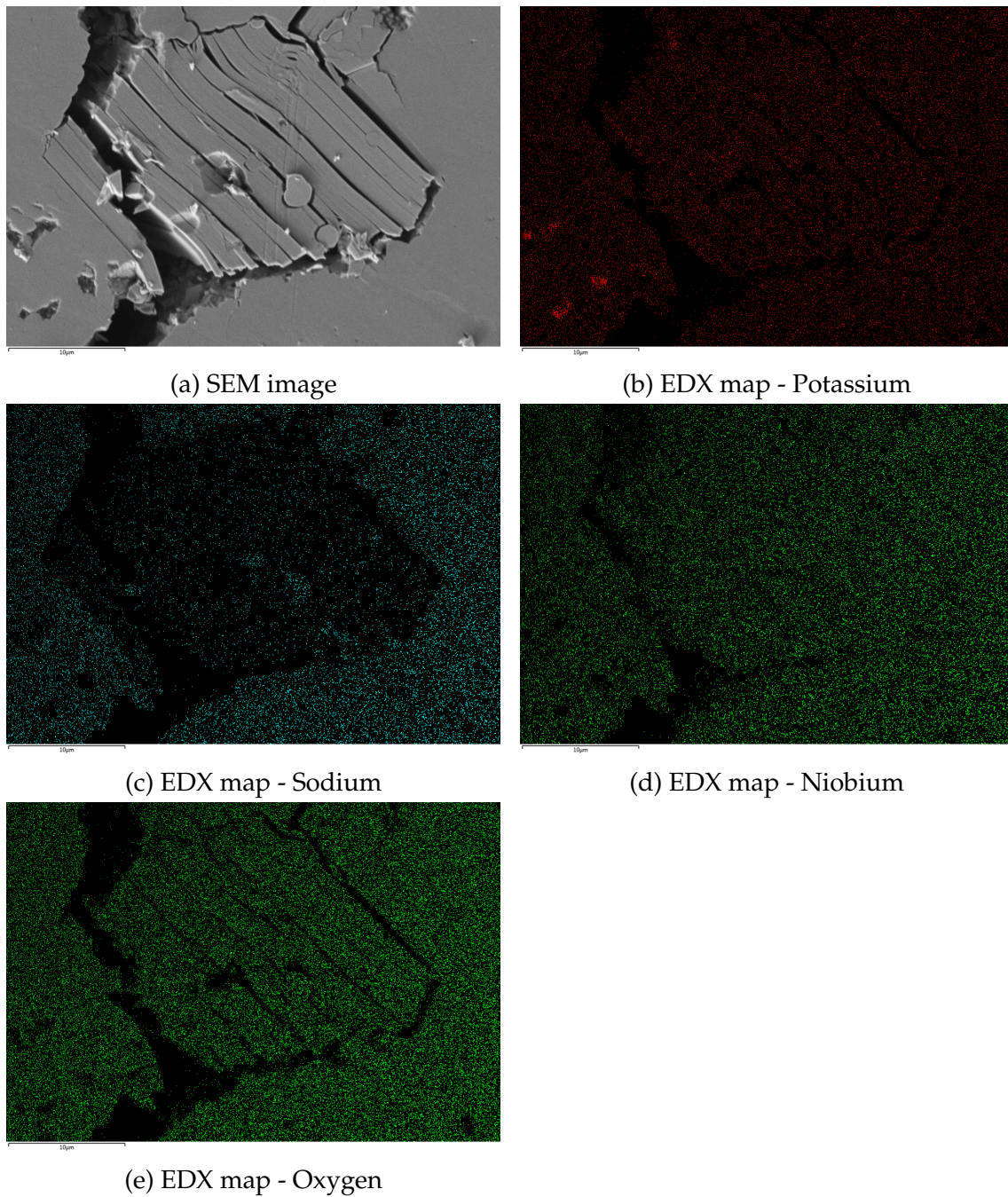
Figure 4.34: EDX map-scan on sample a-11 after soaking for 12h in saline solution. Obtained by Caitlin GUZZO.

(a) b-12 before soaking

(b) a-04 after soaking for 12h in ultra-pure water
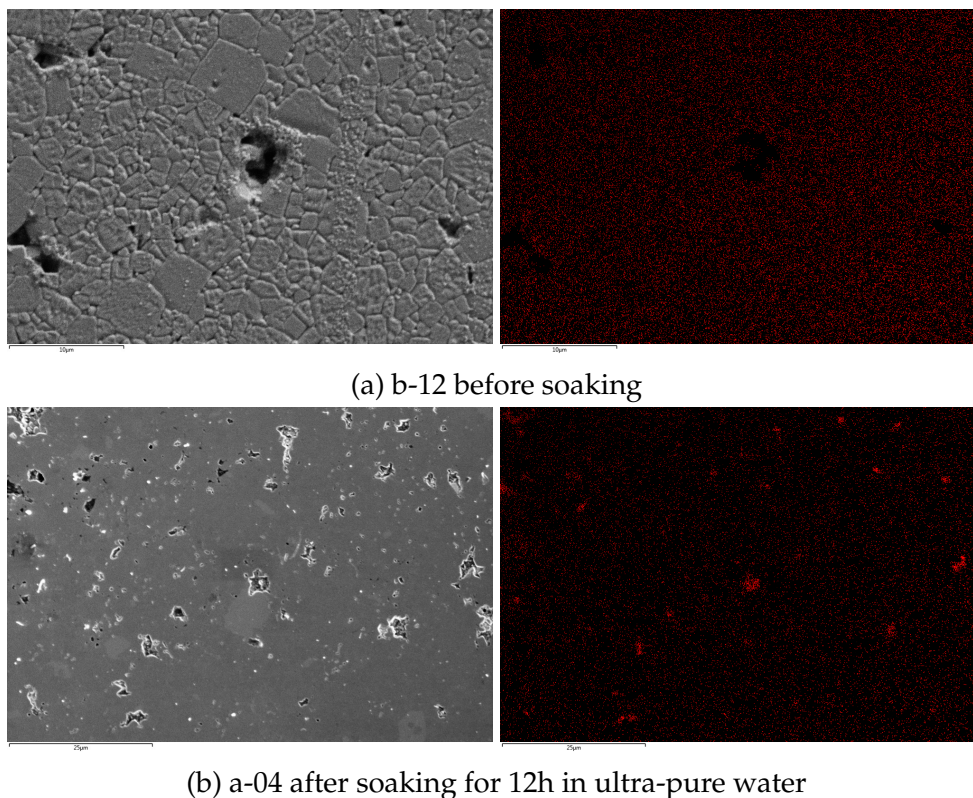
Figure 4.35: EDX map-scan on samples before and after soaking. Highlighting of the potassium excess in the pores after soaking. Obtained by Caitlin GUZZO.

Figure 4.36b presents a sodium-deficient region that corresponds to a lighter grey spot on the SEM. This structure was observed on different samples, they presented different sizes and numbers. In batch c these secondary phases were smaller but present in a higher amount than in batch a. These secondary phases were also visible before soaking as exhibited in Figure 4.36a. To evaluate and confirm the sodium deficiency, a line-scan was performed and the results are presented in Figure 4.37. They show a clear variation in sodium on the light-grey region while all the other elements remain constant. Figure 4.38 represents a crack, originating from a Vickers hardness test, being deflected by one of these structures.
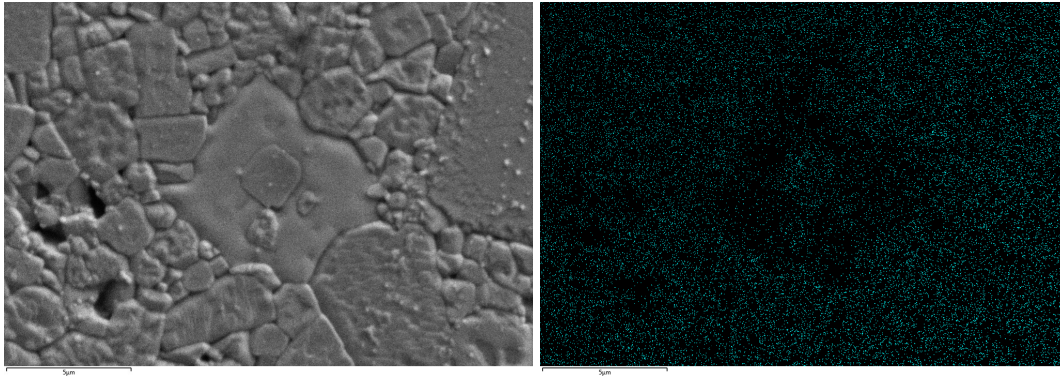
(a) b-12 before soaking.
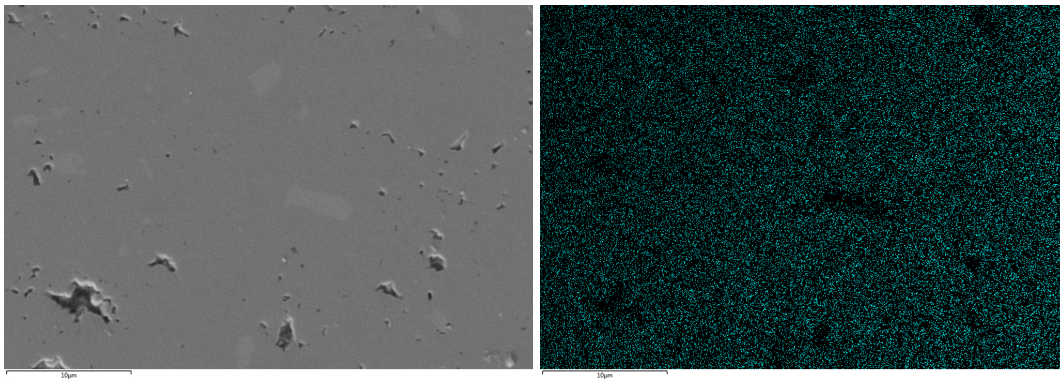
(b) a-11 after soaking for 12h in saline solution.

Figure 4.36: EDX map-scan on samples before and after soaking. Highlighting of the sodium deficiency. Obtained by Caitlin GUZZO.
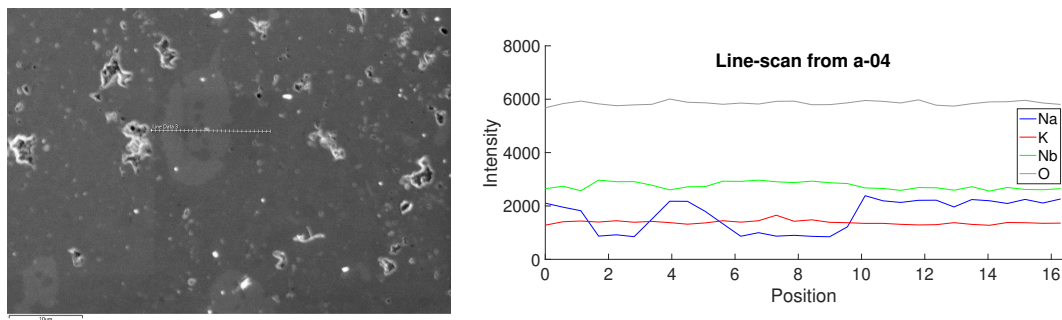
Figure 4.37: EDX line-scan on the sample a-04 after soaking for 12h in ultra-pure water. Obtained by Caitlin GUZZO.

Another line-scan was performed on a distinct sample soaked under the same conditions. The results, presented in Figure 4.39, show a modification of the potassium this time (and a slight variation in the oxygen) while the amount of sodium remains constant. This modification of amount of potassium on surface
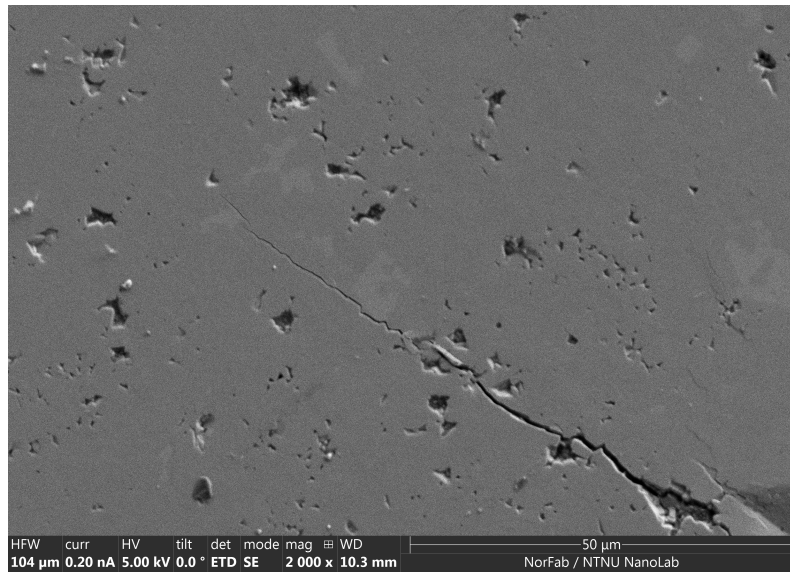
Figure 4.38: SEM image of sample b-04 after soaking for 72h in saline solution. Obtained by Caitlin GUZZO.

with different colors is also highlighted in Figure 4.40b. The pores present an excess in potassium as already presented but the darker areas around it also suggest an excess in potassium. Figure 4.41 show that for an unsoaked but thermally etched sample these dark and potassium enriched areas are present.
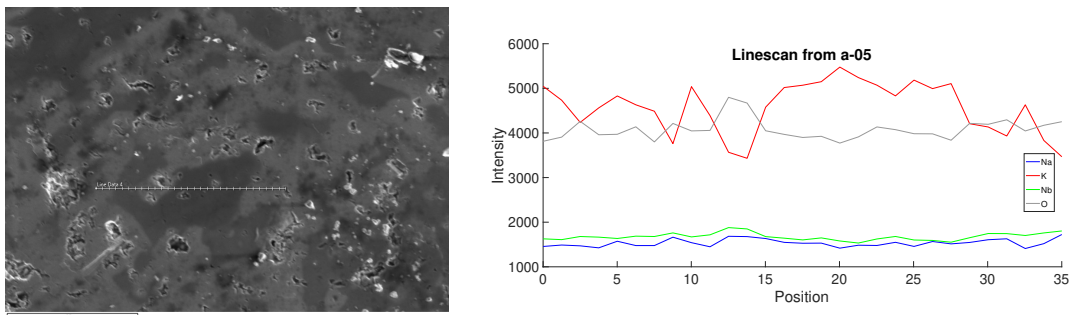
Figure 4.39: EDX line-scan on sample a-05 after soaking for 12h in ultra-pure water. Obtained by Caitlin GUZZO.

(a) SEM image
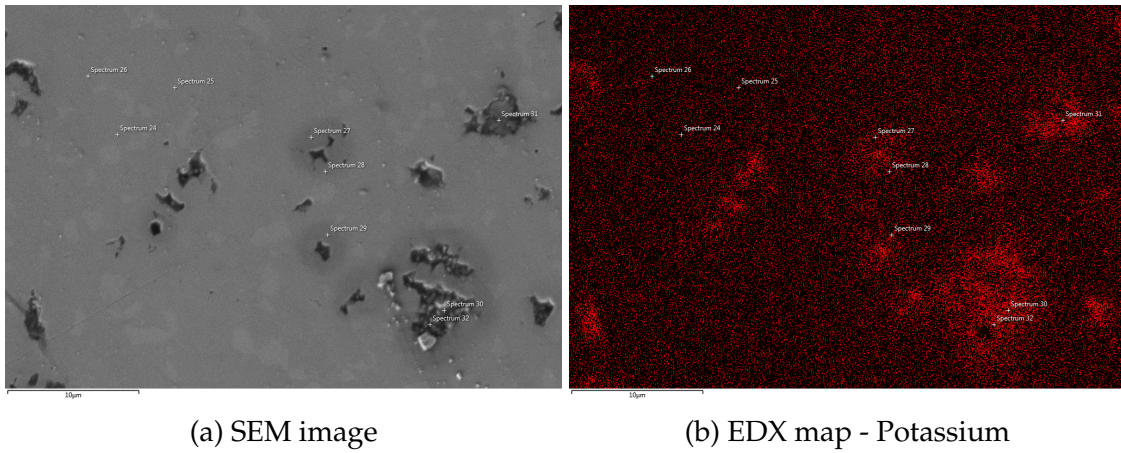
(b) EDX map - Potassium

Figure 4.40: EDX map-scan on sample c-01 after soaking for 12h in deionized water. Highlighting of the potassium excess. Obtained by Caitlin GUZZO.

(a) SEM image
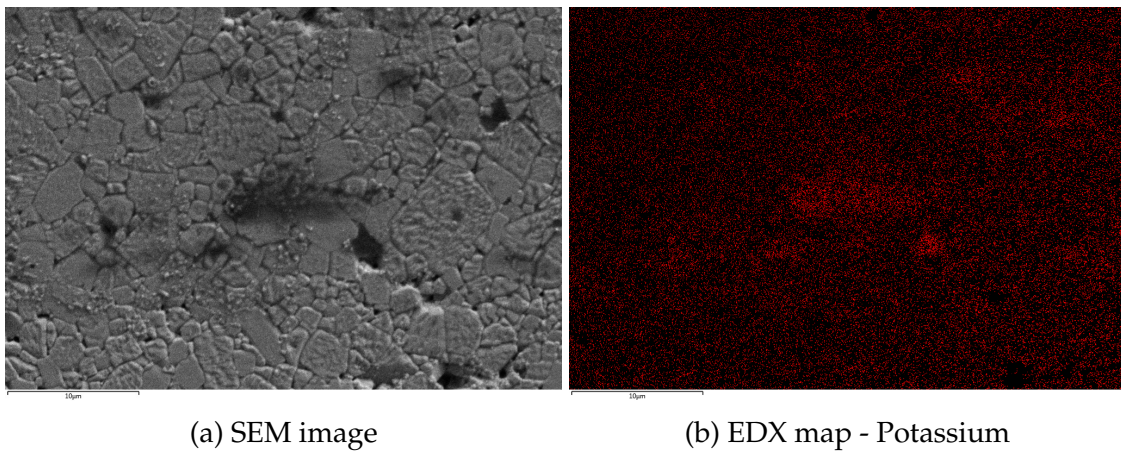
(b) EDX map - Potassium

Figure 4.41: EDX map-scan on sample b-12 unsoaked. Highlighting of the potassium excess. Obtained by Caitlin GUZZO.

CHAPTER

5

DISCUSSION

This chapter provides a discussion of the results presented in chapter 4. It starts with an evaluation of the appearance of the samples both before and after soaking and continues with a critique on the density measurements. This is followed by a discussion on the micro- and crystallographic structures where the secondary phases are emphasized. The evolution of the mechanical properties upon soaking are examined and finally a model for hydration is proposed.

5.1   Appearance and density

After sintering, the samples showed a homogeneous shape and color. They didn't appear brittle and no cracks were visible. After polishing the samples dimensions were also constant in diameter and thickness. Batch c presented smaller but constant diameters: between 7.80 mm and 8.03 mm while it was between 7.97 mm and 8.26 mm for the two other batches. During sintering, as expected, the samples lost some mass. The maximum mass loss was of 1% but the average mass loss was around 0.23%. As shown in Figure 3.4, in batches a and c this mass loss was consistent, whereas a higher variation can be seen in batch b. These low values support a good sintering and not too many alkali losses.

5.1.1   Density measurement

The values obtained with the Archimedes method were presented in Table 4.1 and are between 82.25 and 101.31% with an average value of 92.23%. The unusual variations in measured density can be explained by the sensitivity of certain parameters of the Archimedes method. To illustrate this, 0.0005 g of weight is added to either m_1, m_2 or m_3 used to calculate the relative density of the bulk samples. The corresponding relative density is presented in Table 5.1. This highlights the

ease to obtain a variation of 2% in the resulting density. Even though a high precision scale was used, the continuous change in mass due to the evaporation of the isopropanol when measuring m_3 could explain the variation. Therefore, more trust is placed in the values obtained with the geometrical method.

m_1 [g]	m_2 [g]	m_3[g]	Relative density [%]
0.2170	0.1776	0.2183	92.9264
0.2170 + 0.0005	0.1776	0.2183	93.1405
0.2170	0.1776 + 0.0005	0.2183	94.0822
0.2170	0.1776	0.2183 + 0.0005	91.7986

Table 5.1: Effect of small modifications in mass measurement on the relative density obtained with Archimedes method.

The average densities measured with the geometrical method were given in section 4.1 as 93.22%, 92.18% and 95.60% for the three batches. This is in line with values reported in the literature: over 94% for Yu et al. [95], 95% for Li et al. [54].

5.1.2 Observation after soaking

After soaking, regardless of the soaking conditions, a lot of bubbles were visible as mentioned in section 4.2.2 (Figure 4.4).

Three hypothesis were drawn, all driven by the fact that more bubbles could be seen around cracked samples.

- The presence of a reaction between the liquid and the material liberating gas.

- The release of the air trapped in the pores of the material. As calculated, the average density of the samples was around 93% for the first batch, the one were the bubbles were first observed. This leaves some pores with air entrapped.

- The saturation of the solution by air.

Despite being possible, the two first hypothesis are questionable. The first one because the reaction of KNN with ultra-pure water should not release some gas. The second one because even if some of these pores are open pores, others are closed ones, so the amount of air trapped but capable of being released is probably too small to explain the amount of visible bubbles. The presence of bubbles on the container walls is also inconsistent with this last hypothesis. The third one, however, explains the presence of bubbles on the walls. Indeed, it is based on Henry's law that expresses the concentration of gas dissolved in a liquid at

equilibrium through H, Henry's constant [31]. The liquids used for soaking were stored at room temperature, and at this temperature, H has a given value. A given amount of air is therefore dissolved into the water. When the soaking starts, the experimental setup is put inside an environmental chamber at 37°C, a higher temperature than the room temperature. With an increase of temperature, H increases[1]. The liquid is then saturated and bubbles appear. As their formation is eased by imperfections on surfaces, it explains why these bubbles were mostly visible on cracks (where the apparent surface is larger) and on the container's walls. This hypothesis considers that the presence of a material inside the liquid is not the reason of the emergence of bubbles, and this was confirmed by using a control solution. Indeed, bubbles were also visible in the solution put in the environmental chamber without KNN. This hypothesis is thus the most plausible.

5.1.3   Evolution of the mass and the pH upon soaking

As presented in Figure 4.3, the mass of the samples from batch b increased after soaking while batch c didn't show this increase. After soaking, all samples were dried one night in a desiccator to remove all moisture trapped on the surface and in the pores. From the density measurements (section 4.1) one can see that batch b has a higher porosity than batch c. In one night, the samples from batch b could conceivably not have the time to fully dry. The water present in the pores could explain this increase in mass.

5.1.4   Microstructure

A way to evaluate the sintering is by inspecting the amount of entrapped pores visible with the SEM. As discussed in section 2.2.5, these pores are to be avoided. One example was shown in Figure 4.35a. The pores were found equally in samples from the three batches.

5.2   Crystallographic structure

The quality of the sintering and the calcination can be analyzed through the XRD results, comparing the calcined powder and the sintered pellets (Figure 4.14). The calcination was not perfect as shown by the presence of $NaNbO_3$ in Figure 4.13. This treatment uses temperature up to only 825°C. It was thus decided to not re-mill and redo the calcination even with the presence of these phases and to

---

[1]This statement is true for temperature values under around 100°C, where H starts to decrease as T increases [8].

directly proceed to the sintering at 1125°C to complete the reaction. This choice was profitable as the XRD pattern after sintering showed stoichiometric KNN for batch b and c (Figure 4.14). The first batch presented variations in the peaks locations compared to the expected 2θ locations of the stoichiometric KNN. The hypothesis to explain this phenomenon is the amount of sacrificial powder that was used during sintering. Indeed, for this first batch, less powder was used which can lead to more alkalin losses. The third batch also presented some secondary phases that can be linked to potassium niobates.

In terms of Raman spectroscopy, the majority of the spectra showed the presence of KNN through the active modes v_1, v_2, v_5 and $v_1 + v_5$, characteristic of KNN. However, the first batch presented a lot of different structures with different spectra (Figure 4.5) which can be explained as follows. The splitting into two peaks, observed at a wavenumber of 861cm^{-1}, can be related to the distortion of NbO_6 that occurs when the sodium and potassium ions are not present in stoichiometric amount [27]. Liu et al. [57] presented a FT-Raman spectrum for $K_4Nb_6O_{17}$, a known secondary phase of KNN, with these two bands located at these wavenumber. This structure presents a shorter Nb-O bond which distorts the octoahedra.

The soaking did not impact the bulk crystallographic structure as, no matter the soaking condition, the pattern didn't present notable differences, see Figures 4.15 and 4.16. The crystallographic structure of the surface was also unmodified as exhibited by the GIXRD (Figures 4.17 and 4.18).

5.3   Secondary phases

Raman spectroscopy and EDX measurements allowed to highlight the presence of different secondary phases. Some could be seen before soaking, others appeared after.

5.3.1   Layered structures

A first structure that could be observed is the layered structure (Figure 4.34a) which is sodium deficient. A literature review allowed to identify this structure as being $K_4Nb_6O_{17}$, a layered tungsten bronze type structure [2, 59].

This $K_4Nb_6O_{17}$ presents sheets that are cleavable and flexible [34]. This corresponds to what was observed in the SEM, as some of the layered appeared bended in Figure 4.34a.

The Raman spectra of this structure are presented in Figure 4.6. A comparison with what was found in the literature is presented in Figure 5.1. The spectra pre-

sented in Figure 5.1b were obtained by Liu et al. [57], while Figure 5.1a takes the spectra previously presented and adds the Raman shifts associated with the different peaks. It can be highlighted that the peaks are located at the same Raman shift even if the relative intensities are sometimes different. This allows to conclude that these secondary phases are indeed a polyniobate: $K_4Nb_6O_{17}$.
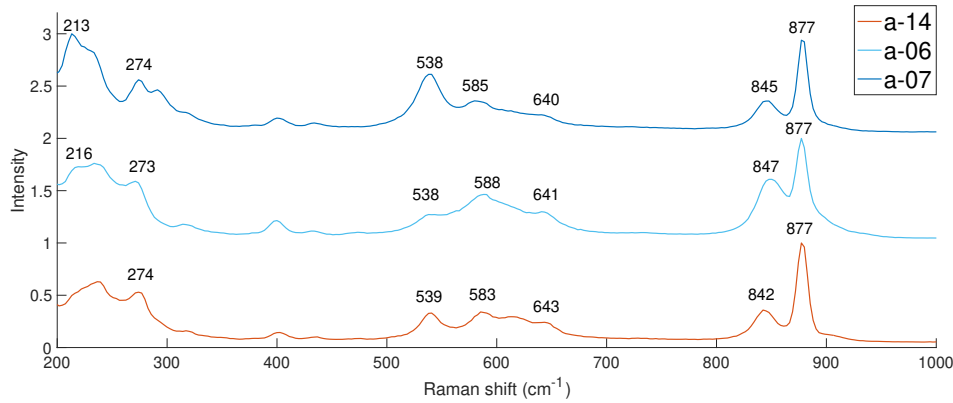
(a) Raman spectra of layered structure on three different samples.
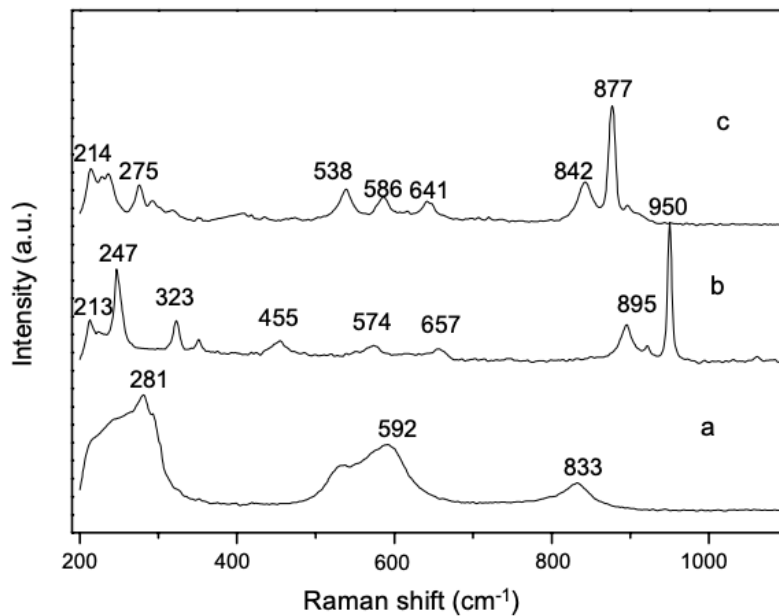
(b) FT-Raman spectra of the samples: (a) $KNbO_3$, (b) KNb_3O_8, and (c) $K_4Nb_6O_{17}$ [57]

Figure 5.1: Comparison of the layered structures with $K_4Nb_6O_{17}$.

It could be said that for some of these layered structures the Raman spectra shares similarities with both stoichiometric KNN and $K_4Nb_6O_{17}$. This is highlighted in Figure 5.2. This can be explained by the combination of two phenomena: the depth of the layered structure can be smaller than the one of the Raman spectroscopy, and a grain of stoichiometric KNN could be present in the middle of
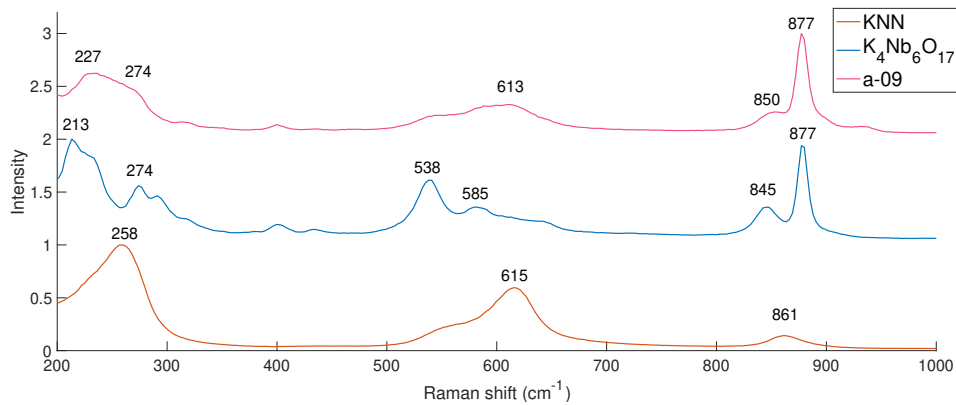
Figure 5.2: Comparison of the Raman spectra measured on a layered structure with KNN and $K_4Nb_6O_{17}$.

the polyniobate. Indeed, Figure 4.34a proved this was possible.

5.3.2 Light-grey structures

As shown in Figure 2.13, SEM revealed the presence of light-grey structures. They were reported to be tungsten-bronze type phase, $K_2Nb_4O_{11}$ or $K_6Nb_{10.88}O_{33}$ [7].

Structures with the same appearance were observed in this work (Figure 4.36b) and EDX allowed to measure their sodium deficiency compared to stoichiometric KNN. Another correlation with the presence of these $K_2Nb_4O_{11}$ is reported in the XRD results. Indeed, Figure 4.14, presenting XRD pattern before soaking of the different batches, shows peaks corresponding to this phase in batch c. It was in this batch that the light-grey structures were the most present. These polynio-bates were already present before soaking as highlighted by Figure 4.36.

These light-grey structures could not be linked to any of the other structures found with Raman spectroscopy or nanoidentation. Shape-wise they could be the small darker area observed in Figures 4.11 and 4.12. However neither their amount nor their mechanical properties are correlated. Indeed, Figure 4.38 shows one of the light-grey structures deflecting a crack, while the hardness of the small darker area obtained through nanoindentation was lower compared to the rest of the sample. This mismatch in hardness prevents these structures from being linked.

5.3.3 Shiny structures

The shiny structures, highlighted with the Raman spectroscopy (Figure 4.7) and the nanoindentation, could not be observed with the SEM. This was expected

as refracted light can be measured with the optical microscope but not with the scanning electron microscope.

The appearance of the shiny structures can be compared to the one of niobium, a silvery grey metal [17]. The presence of these supposed niobium-rich areas correlates with the work of Ozmen et al. [63]. Indeed, they presented the formation of a Nb-rich crust after 100-hour aging in ultra-pure water based suspensions with an adjusted pH at 4. A part of their work was presented in the literature review (section 2.2.7): the rates of dissolution of the different cations of KNN are different and depend on the pH. They presented niobium as the most stable cation and this stability was increased with an acidic medium. This adapts to this work as follows: the different soaking conditions presented an acidic medium, the saline solution being the most acidic with a pH around 5.5, the deionized water is known to have a pH around 6 while the ultra-pure water is expected to have a pH just below 7. Under these conditions the release of potassium and sodium is larger than the one of niobium and the formation of a Nb-rich crust is possible.

The link between the pH and niobium stability can be highlighted with the presence of these silvery structures after 6h in saline solution, and their absence after 12, 24 and 72 hours [2]. As shown in Figure 4.3, the pH of the saline solution increases with time, this is due to the release of alkali. The small thickness of any Nb-crust would be undetectable by Raman due to the interaction depth of the technique. Indeed the thickness of the Nb-rich crust was calculated to be 0.01184 μm by Ozmen et al. after a 100-hour soaking while the depth of the beam used in Raman spectroscopy is around 0.7 μm and the soaking lasted shorter in this work. This considerable difference could explain why the spectra are mostly comparable to KNN: it indeed measured the KNN underneath. Mostly as half of the spectra presented in Figure 4.7 represented stoichiometric KNN, while the other half, corresponding to samples soaked in ultra-pure water and deionized water, can be attributed to $K_2Nb_4O_{11}$.

However, ultra-pure water and deionized water have a higher pH than saline solution and therefore niobium should be less stable. This is inconsistent with the fact that samples soaked under these conditions presented the highest amount of these structures. To clarify this, it has to be highlighted that these shiny structures were visible after soaking in these two liquids only on samples from batch a. And this batch contained a lot of potassium-rich area with the secondary phases $K_4Nb_6O_{17}$, $K_2Nb_4O_{11}$ and $K_6Nb_{10.88}O_{33}$. As potassium is released three times faster than niobium: all these large K-rich areas could be transformed into Nb-rich crust during soaking. In batch c, no sheet-like structures were visible but the K-rich regions were present. However they were smaller and the Nb-rich layer resulting from the leakage of potassium could be too small to be seen. This is also supported by the fact than the different spectra of the silvery structures on samples soaked in ultra-pure water and deionized water (shown in Figure 4.7)

---

[2]Only one small area was visible after 72h.

presented the characteristic peaks of potassium niobate.

5.4 Mechanical properties

5.4.1 Nanoindentation

The nanoindentation result showed that, on the surfaces whose look didn't change after soaking and on average, the hardness had a slight tendency to decrease for samples soaked, regardless of the soaking conditions (Figures 4.20a and 4.28a). However, on some samples, the hardness presented an increase, this is visible for sample c-01 soaked in denionized water (Figure 4.20b) and b-04 soaked 72h in saline solution (4.28c)

Some of the nanoindentation curves on the surface looking unchanged after soaking present a slight stepped shape on the loading part. This is the case in Figure 4.26. This could be the trace of different behaviors of the surface, i.e. a different structure to go through before going back to the behavior corresponding to the bulk. This situation is illustrated in Figure 5.3 where h_1 is the depth of the secondary phases. This behavior was also observed on samples before soaking (Figure 4.23) and is too inconsistent with the rest of the dataset to draw any conclusion. However, on the different structures present on the surface, this behavior was more emphasized as the slope of the curve increased sharply after a given displacement higher than 800 nm in certain samples, 600 nm in others or even higher (see also Figure 4.23). As a comparison, the depth of the Raman is 0.7 μm (700 nm) and was able to measure the different spectra of the structure. This behavior could mean that the material is impacted by the soaking only to a depth less than these hundreds of nanometers and that the bulk of the material wasn't weakened.

Some measurements out of samples soaked for 6h in saline solution presented a curve with a different shape than the rest (Figure 4.24 and 4.25). This behavior is called the *nose effect*. It is the result of a creep effect in the material and could be avoided by applying a dwell time before the unloading [76]. This nose effect leads to a negative contact stiffness, used to calculate the hardness. Therefore the hardness can't be confidently measured with the Oliver and Pharr method used in this work.

Secondary phases

The secondary phases identified as layered tungsten-bronze $K_4Nb_6O_{17}$ and Nb-crust presented lower values of hardness than the rest of the material. This was shown in Figures 4.19 and 4.21 by a maximum displacement at respectively 1500

$$h_{tot} > h_1 \rightarrow 2 \text{ different structures are measured}$$
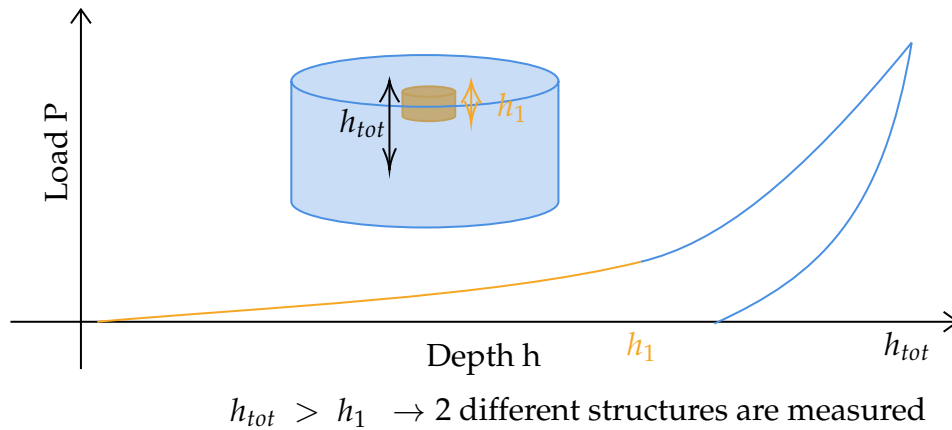
Figure 5.3: Schematic representation of the measurement of a soft secondary phase with the nanoindenter.

and 2900 nm. As a comparison the maximum displacement measured on the rest of the surface was 200 nm. This is translated to a loss of hardness by three orders of magnitude.

Figure 4.34a featured cracks on the layered tungsten-bronze phase appearing after soaking. Because of the poor hardness observed, the cracks are believed to start from one of the cracks between the sheets.

A hypothesis for the low hardness of the Nb-crust lies in the ductility of niobium. This metal presents a Vickers hardness of 1.47 GPa [17] which correlates with the low value observed in Figure 4.20a. However, the thickness of this crust was presented (in section 5.3.3) to be lower than 10 nm. Hence, the results suggest that the thickness impacted by the presence of the crust is larger than the thickness of the actual crust.

5.4.2 Hardness variation

The Vickers hardness of samples before soaking was measured, in average, to be between 3.2 GPa for the batch a and 4.01 GPa for the batch c. This is in the range of the 3.55 GPa reported for KNN by another study [55] and also presented in the literature review, section 2.2.8.

As presented in Figures 4.29 and 4.30, the variation of the Vickers hardness showed sometimes an increase and sometimes a decrease upon soaking. The samples from batch a, soaked for 12h, had the most inconsistent results with the highest increase and the highest decrease in hardness. Out of the eight samples tested from this batch, four presented an increase in hardness, and these four samples were broken during soaking. Out of the four samples presenting a decrease in hardness, three presented an unchanged surface after soaking. The hypothesis

of the survivorship bias can therefore be drawn: the broken, and therefore un-measured surfaces, presented probably the lowest hardness as they broke; only the remaining parts, probably the hardest were measured and this could explain the general impression of increase in hardness. Figure 5.4 presents the two samples that presented the highest increase in hardness, they were both soaked for 12h in saline solution and they both lost a large portion upon soaking.

(a) a-10

(b) a-11. The measurement were performed on the piece on the right.

Figure 5.4: Appearance of the two samples presenting the highest increase in Vickers hardness.

Looking in more details at the results from the soaking of the other batches, the samples from batch b presented a behavior independent from the soaking condition, shown in Figures 4.29 and 4.30. After 6h the two samples presented some-times higher sometimes lower values. After 24h one sample presented a clear increase in hardness while the second one presented some decrease. Finally after 72h one sample presented a clear decrease while the other showed no differences. All the samples from batch c, no matter the soaking conditions, presented their seven measurements in between the measurements of the two unsoaked samples. So even if the average hardness presents a variation from -3.47% to $+4.59\%$, the individual data points don't show any clear modification. It can be concluded that, for this batch, the soaking didn't impact the Vickers hardness.

One sample marks an exception to this observation. c-03, soaked for 6 hours in saline solution presented a clear decrease in hardness as its highest hardness corresponded to the lowest value of one of the unsoaked sample and to the average of the second unsoaked sample. This is also the only sample presenting a change in the GIXRD pattern (Figure 4.18a). The characteristic peaks of KNN representative of the crystallographic structure were visible but the noise was higher than compared to the other samples. However, the nanoindentation results didn't present this decrease in hardness as show in Figure 4.28a.

Some of the indents performed were image with SEM, which means that the corresponding hardness could be traced back. A notable result is presented in Figure 5.5. This indent presents a dark outline, especially on the top-part of the indent,

characteristic of what was found after soaking. However the obtained hardness was 400.5 GPa while the average for this sample was 399.14 GPa. This apparently different surface didn't give a different hardness. This result is not unforeseen as the goal of the Vickers hardness measurement is to obtain an average hardness of a representative part of the sample. However, it can be said that the new structures appearing on the surface are not contributing to a large decrease of the Vickers hardness. It should be noted that this dark outline was not observed in other indents.
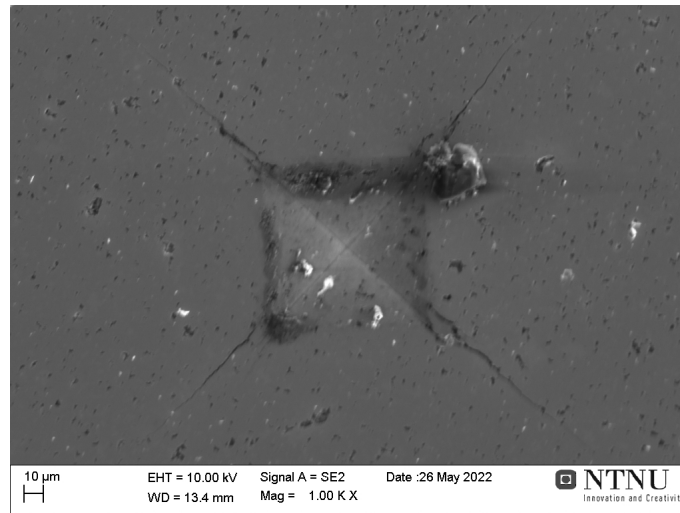
Figure 5.5: SEM images of an indent performed on c-09 after soaking

5.5 Hydration

5.5.1 Layered structure

Gasparin et al. [34] studied the impact of the humidity on this structure. Their results showed the formation of a trihydrate compound where the sheets would glide along a vector contained in the (100) plane. This gliding leads to an increase of the distance $|b|$, while the two other dimensions, $|a|$ and $|c|$, characteristic of the NbO_6 octahedra, were constant upon hydration. Their results being for exposure to humidity present in the air, it can be said that by immersing the compound in water, this phenomenon accelerates. Therefore when soaking, this hygroscopic secondary phase will increase in volume. This increase in volume explains why some surfaces after soaking presented cracking and flaking as seen in Figure 4.32.

The insertion of water molecules in between the sheets breaks some bonds, as can be seen in Figure 5.6, where the dotted lines represent the bonds that break during the formation of the trihydrate compound. This eases the separation of the sheets under mechanical stress and the presence of these structures should

decrease the hardness of the material. This corresponds to what was observed in the nanoindenation results and discussed in section 5.4.1 as the curves measured on these structures showed higher displacement for a given load and a hardness decreased by orders of magnitude. The role of these layered structures in the mechanical stability of the sample upon soaking is supported by the fact that, before soaking, significantly more of these structures could be observed on samples of batch a compared to batch c and after soaking in the different liquids for 12 hours, almost all the samples from batch a presented cracks or were broken, while samples from batch c appeared mostly flawless. Based on this finding it can be concluded that the cracks observed after soaking (Figures 4.34a, 4.32) originated from these structures.
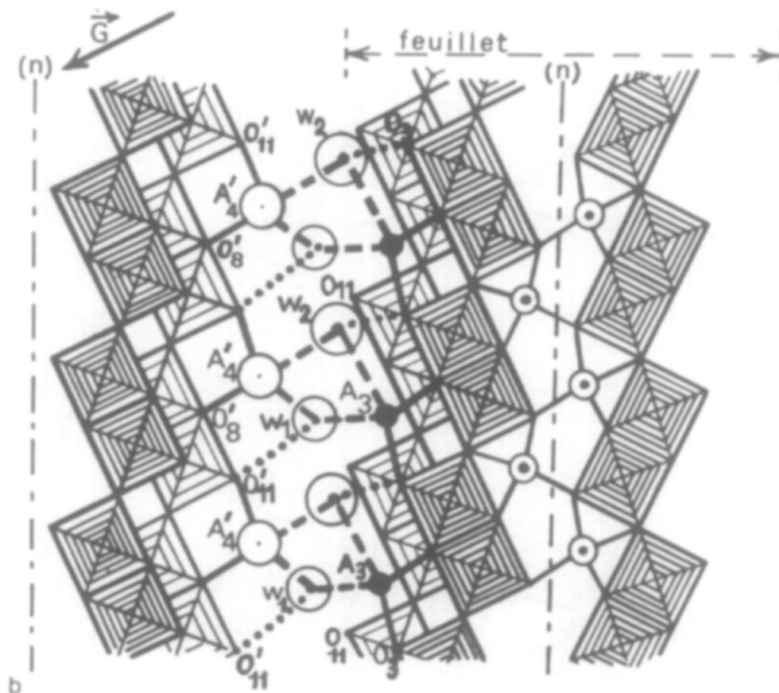
Figure 5.6: Hydration mechanism of $K_4Nb_6O_{17}$ [34]

5.5.2 Potassium leakage

As presented in the literature review, section 2.2.7, potassium is expected to be the first alkalin to leave the pellet upon soaking. This was confirmed by the EDX map showing potassium in the pores after soaking but not before soaking. This would mean that during the rinsing of the surface after soaking, the potassium entrapped in the pores is not fully rinsed and accumulates.

With the cracks originating from the hydration of the layered structures, more surface is exposed which could increase this leakage.

The effect of soaking is believed to be a desorption of cations from the surface after a reaction between H^+, OH^- and the surface. However, as shown in Figure 4.41, an enrichment of potassium on the surface was seen on an unsoaked sample. Two reasons can explain this without jeopardizing the described effect of soaking:

- The study of Gasparin [34] showed that hydration of the layered structure happened with the humidity of the air. The unsoaked samples, even if they were kept in a desiccator, spent some time in contact with the air.

- The sample on which the phenomenon was observed was thermally etched. This means it received a lot of thermal energy. This energy could be sufficient to start the reaction of releasing potassium and therefore explain the results.

CHAPTER

6

CONCLUSION

The aim of this thesis was to contribute to the general effort of developing KNN-based materials for biomedical applications. To fulfill this objective, it was decided to focus on the impact of soaking on the mechanical properties of KNN as their control over time is of great importance for implant materials. In practice, this translates by using three liquids of different chemical complexity for soaking and measuring their impact on the material though different mechanical and chemical characterization methods.

In a first step, state of the art of KNN has been studied. This allowed to highlight the benefits of this material as a bone implant and to predict the challenges that could arise during the work. The main qualities of KNN are its biocompatibility and its mechanical and piezoelectric properties aligned with the function it intends to fulfill. While the main challenge is the reproductability due to the presence of secondary phases.

Then, a solid-state synthesis was carried out to synthesize three batches of stoichiometric KNN for a total of 42 pellets. The soaking took place in ultra-pure water and deionized water for 12h and in saline solution for different periods of time: 6h, 12h, 24h and 72h.

Different characterization methods, each of them with their own goal, were used. Nanoindentation and microindentation allowed to control the evolution of the hardness of the surface and the bulk respectively. X-ray diffraction was also performed on the bulk and on the surface to monitor change in the crystallographic structure. Raman spectroscopy was used to investigate the chemical structure at the surface. Finally SEM and EDX were used to investigate the chemical composition and appearance of the samples.

Analysis performed on samples before soaking reported an average hardness of 12.28 GPa and an average Vickers hardness of 3.48 GPa. Raman spectroscopy identified layered tungsten-bronze $K_4Nb_6O_{17}$ secondary phase by comparing the results with previously reported results. Tungsten-bronze $K_2Nb_4O_{11}$ secondary

phase were identified both with SEM and XRD.

The two main conclusions that emerged from this thesis are that no clear difference in behavior was measured based on the soaking conditions and that secondary phases can be detrimental to the material. Indeed, the hardness showed only notable differences when measured on the secondary phases with the nanoindentation. The hygroscopicity of layered tungsten-bronze $K_4Nb_6O_{17}$ was determined to be the main factor of failure of the samples by the formation of a trihydrate compounds whose mechanical properties are prone to fracture. The formation of a Nb-crust was suggested by the presence of shallow niobium-rich areas. They can be prejudicial for the mechanical stability of the material due to the low hardness of niobium. The presence of this crust decreased with the increase of the pH of the saline solution. This is encouraging when keeping in mind the final biomedical applications as human blood and interstitial fluids present a pH of 7.35-7.45 [67], a more basic value than what was used in this work, and also a value for which the niobium is less susceptible to form a crust. A desorption of potassium from the surface during soaking was highlighted with EDX but was not linked to any modification of the mechanical stability of the material as the Vickers hardness presented low variations. The crystallographic structure remained constant through soaking as exhibited by the GIXRD results.

It is concluded that, in the absence of layered tungsten-bronze $K_4Nb_6O_{17}$ secondary phases, pellets of stoichiometric KNN are able to sustain 72-hour soaking in saline solution. This result is encouraging in the pursuit of making KNN an efficient material for bone implant. However, further work is required to reach this goal.

Further work

As the results showed no difference in the bulk of the material, next studies should focus on longer soaking time to both accentuate the modifications at the surface and to investigate whether the bulk undergoes any modification.

Because of their impact on the material, layered tungsten bronze $K_4Nb_6O_{17}$ should be avoided in future work. In this work it was due to a poor amount of sacrificial powder during sintering. Therefore this parameter should be more precisely controlled.

Nanoindentation could be performed with different loads on a same sample. This would allow to investigate the variation of the surface properties and to measure the thickness of the impacted layer. Different parameters for the Raman spectroscopy would also help decreasing the penetration depth.

As the samples sustained soaking in saline solution, this liquid could be used for a longer soaking. However, different and more complex, liquids can be used. The

pH was shown to be an important factor, therefore it should be more controlled in future work. Phosphate-buffered saline, with its pH at 7.4 is a good candidate for the next solution to use.

BIBLIOGRAPHY

[1] ISO 23317:2014. Implants for surgery — in vitro evaluation for apatite-forming ability of implant materials.

[2] J. Acker, H. Kungl, and MJ. Hoffmann. Influence of alkaline and niobium excess on sintering and microstructure of sodium-potassium niobate $(K_{0.5}Na_{0.5})NbO_3$. *Journal of American Ceramic Society*, 93, 2010. URL: https://doi.org/10.1111/j.1551-2916.2010.03578.x.

[3] Fran Adar. Depth resolution of the raman microscope: Optical limitations and sample characteristics, 2010.

[4] Kalsoom Akhtar, Shahid Ali Khan, Sher Bahadar Khan, and Abdullah M. Asiri. *Chapter 4: Scanning Electron Microscopy: Principle and Applications in Nanomaterials Characterization In: Sharma S. (eds) Handbook of Materials Characterization*, pages 113–145. Springer, 2018. URL: https://doi.org/10.1007/978-3-319-92955-2_4.

[5] Basics of Raman spectroscopy Anton Paar. https://wiki.anton-paar.com/us-en/basics-of-raman-spectroscopy/. Last accessed on 06-05-2022.

[6] C. Artini. Crystal chemistry, stability and properties of interlanthanide perovskites: A review. *Journal of the European Ceramic Society*, 37, 2017. URL: https://doi.org/10.1016/j.jeurceramsoc.2016.08.041.

[7] Malič B, Koruza J, Hreščak J, Bernard J, Wang K, Fisher JG, and Benčan A. Sintering of lead-free piezoelectric sodium potassium niobate ceramics. *Materials*, 8, 2015. URL: https://doi.org/10.3390/ma8125449.

[8] Aquatech bernard Pironin. Loi de henry. URL: http://bernard.pironin.pagesperso-orange.fr/aquatech/henry.htm.

[9] M. Birkholz. International tables for crystallography. *International Union of Crystallography*, H:581–600, 2019. URL: https://doi.org/10.1107/97809553602060000969.

[10] J. Blendell and W. Rheinheimer. *Solid-State Sintering In:Encyclopedia of Materials: Technical Ceramics and Glasses*. Elsevier, 2021. URL: https://doi.org/10.1016/B978-0-12-803581-8.12084-3.

[11] Bone remodeling cycle. `https://www.orthopaedicsone.com/display/Clerkship/Describe+the+process+of+bone+remodeling`. Last accessed on 30-03-2022.

[12] Britannica - Human skeleton. `https://www.britannica.com/science/human-skeleton`. Last accessed on 15-03-2022.

[13] H. Bruncková, L. Medvecký, P. Hvizdoš, and J.Ďurišin. Structural and nanomechanical properties of sol–gel prepared (K,Na)NbO$_3$ thin films. *Surface and interface analysis*, 47, 2015. URL: `https://doi.org/10.1002/sia.5846`.

[14] R. Zuo; J. Rodel;R. Chen and L. Li. Sintering and electrical properties of lead-free na0.5k0.5nbo3 piezoelectric ceramics. *J. Am. Ceram. Soc*, 89(6), 2006. URL: `https://doi.org/10.1111/j.1551-2916.2006.00991.x`.

[15] Jantzen CM. *Thermodynamic approach to glass corrosion IN: Corrosion of Glass, Ceramics and Ceramic Superconductors: Principles, Testing, Characterization and Applications*. Clark; Zoitos; Noyes Publications, 1992.

[16] Congruent dissolution, Oxford reference. `https://www.oxfordreference.com/view/10.1093/oi/authority.20110803095632223`. Last accessed on 21-04-2022.

[17] R.W. Balliett; M. Coscia and F.J. Hunkeler. Niobium and tantalum in materials selection. *The Journal of The Minerals, Metals & Materials Society (TMS)*, 38:25–27, 1986. URL: `https://doi.org/10.1007/BF03258681`.

[18] R. Cui, Ke Tang, D. Zhu, C.Yue, and L. Yang. Sm^{3+}-doped knns ferroelectric ceramics with enhanced photoluminescence by polarization-feld-modulation. *Journal of Materials Science: Materials in Electronics*, 31, 2020. URL: `https://doi.org/10.1007/s10854-019-02552-x`.

[19] LLadislav Cvrček. *Chapter 14 - Plasma Modified Polymeric Materials for Implant Applications IN: Non-Thermal Plasma Technology for Polymeric Materials*. Elsevier, 2019. URL: `https://doi.org/10.1016/B978-0-12-813152-7.00014-7`.

[20] Matthew P Dewar. Characterization and evaluation of aged 20cr32ni1nb stainless steels, 2013. URL: `https://doi.org/10.7939/R3191N`.

[21] Schwarcz Henry P.; Abueidda Diab and Jasiuk Iwona. The ultrastructure of bone and its relevance to mechanical properties. *Frontiers in Physics*, 5, 2007. URL: `https://doi.org/10.3389/fphy.2017.00039`.

[22] Dielectric material. `https://whatis.techtarget.com/definition/dielectric-material`. Last accessed on 29-03-2022.

[23] Dolhen, Morgane, and Mahajan et al. Sodium potassium niobate (k 0.5 na 0.5 nbo 3 , knn) thick films by electrophoretic deposition. *RSC Advances*, 5, 12 2014. URL: https://doi.org/10.1039/C4RA11058G.

[24] Marwa El-Azazy. *Introductory Chapter: Infrared Spectroscopy - A Synopsis of the Fundamentals and Applications*, pages 2–10. IntechOpen, 11 2018. URL: https://doi.org/10.5772/intechopen.82210.

[25] Miller indices crystallography Encyclopædia Britannica. https://www.britannica.com/science/Miller-indices. Last accessed on 27-04-2022.

[26] The seven primitive crystal systems Encyclopædia Britannica. https://www.britannica.com/science/orthorhombic-system#/media/1/433565/149097. Last accessed on 26-04-2022.

[27] Chang Won Ahn et al. Raman spectra study of $K_{0.5}Na_{0.5}NbO_3$ ferroelectric thin films. *The Japan Society of Applied Physics*, 49, 2010. URL: https://doi.org/10.1143/JJAP.49.095801.

[28] G. Quinn et al. Fracture toughness of ceramics by the vickers indentation crack length method: a critical review. *American Ceramic Society*, 27, 2007. URL: https://doi.org/10.1002/9780470291313.ch5.

[29] M Ahart; M Somayazulu; R Cohen et al. Origin of morphotropic phase boundaries in ferroelectrics. *Nature*, 451, 2008. URL: https://doi.org/10.1038/nature06459.

[30] The Raman effect F. Agulló-Rueda. https://www.icmm.csic.es/Fagullo/courses/raman/effect/. Last accessed on 06-05-2022.

[31] D. G. Fredlund. Density and compressibility characteristics of air–water mixtures. *Canadian Geotechnical Journal*, 13, 1976. URL: https://doi.org/10.1139/t76-040.

[32] E. Fukada and I. Yasuda. On the piezoelectric effect of bone. *Journal of the Physical Society of Japan*, 12, 1957. URL: https://doi.org/10.1143/JPSJ.12.1158.

[33] J. Garcia and F. Rubios-Marcos. Polymorphic phase boundary in piezoelectric oxides. *Journal of applied physics*, 127, 2020. URL: https://doi.org/10.1063/5.0002983.

[34] Madeleine Gasperin and Marie Thérèse Le Bihan. Mecanisme d'hydratation des niobates alcalins lamellaires de formule $A_4Nb_4O_{17}$ (a = k, rb, cs). *Journal of Solid State Chemistry*, 43, 1982. URL: https://doi.org/10.1016/0022-4596(82)90251-1.

[35] K. Grandfield. Bone, implants, and their interfaces. *Physics Today*, 68:40–45, 2015. URL: https://doi.org/10.1063/PT.3.2748.

[36] H. Gu, K. Zhu, X. Pang, B. Shao, J. Qiu, and H. Ji. Synthesis of (k, na) (nb, ta)o3 lead-free piezoelectric ceramic powders by high temperature mixing method under hydrothermal conditions. *Ceramics International*, 38, 2012. URL: https://doi.org/10.1016/j.ceramint.2011.10.003.

[37] S. Gupta. *1 - Introduction to ferroelectrics and related materials In: Ferroelectric Materials for Energy Harvesting and Storage*. Woodhead Publishing Series in Electronic and Optical Materials, 2021. URL: https://doi.org/10.1016/B978-0-08-102802-5.00001-7.

[38] D. Hadjidakis and I. Androulakis. Bone remodeling. *Annals of the New York Academy of Sciences*, 1092, 2006. URL: https://doi.org/10.1196/annals.1365.035.

[39] G.W. Hastings and F.A. Mahmud. Electrical effects in bone. *Journal of biomedical engineering*, 10, 1988. URL: https://doi.org/10.1016/0141-5425(88)90109-4.

[40] Hygroscopic Definition in Chemistry by Anne Marie Helmenstine. https://www.thoughtco.com/definition-of-hygroscopic-605230. Last accessed on 21-04-2022.

[41] Hysitron. Ti 950 triboindenter user manual. Revision 10.0.1216.

[42] A. Iacomini, JA. Tamayo-Ramos, C. Rumbo, I. Urgen, and M. Mureddu et al. Processing optimization and toxicological evaluation of "lead-free" piezoceramics: A knn-based case study. *Materials*, 14, 2021. URL: https://doi.org/10.3390/ma14154337.

[43] Ibn-Mohammed, Koh, S.C.L., Reaney, and I.M. et al. Are lead-free piezoelectrics more environmentally friendly? *MRS Communications*, 7, 2017. URL: https://doi.org/10.1557/mrc.2017.10.

[44] Incongruent dissolution, Oxford reference. https://www.oxfordreference.com/view/10.1093/oi/authority.20110803100000549. Last accessed on 21-04-2022.

[45] B.M. Isaacson and R.D. Bloebaum. Bone bioelectricity: what have we learned in the past 160 years? *Journal of biomedical materials research*, 95, 2010. URL: https://doi.org/10.1002/jbm.a.32905.

[46] J Salem; G Quinn; M Jenkins. *Measuring the Real Fracture Toughness of Ceramics: ASTM C 1421 IN: Fracture Mechanics of Ceramics. Fracture Mechanics of Ceramics*. Bradt; Munz;; Sakai; White; Springer Boston, 2005. URL: https://doi.org/10.1007/978-0-387-28920-5_40.

[47] D Jenko, A benčan, B Malič, J Holc, and M Kosec. Electron microscopy studies of potassium sodium niobate ceramics. *Microscopy and Microanalysis*, 11, 2005. URL: https://doi.org/10.1017/S1431927605050683.

[48] (2022). JoVE Science Education Database. Materials Engineering. X-ray Diffraction. Cambridge. MA. https://www.jove.com/v/10446/x-ray-diffractions. Last accessed on 25-04-2022.

[49] D. Kharea, B. Basub, and A. Dubey. Electrical stimulation and piezoelectric biomaterials for bone tissue engineering applications. *Biomaterials*, 258, 2020. URL: https://doi.org/10.1016/j.biomaterials.2020.120280.

[50] B Malic; DJenko; J Holc; M Hrovat; M Kosec. Synthesis of sodium potassium niobate: A diffusion couples study. *Journal of American Ceramic Society*, 91, 2008. URL: https://doi.org/10.1111/j.1551-2916.2008.02376.x.

[51] M. Kosec, B. Malic, A. Bencan, and T. Rojac. *Chapter 5 KNN-Based Piezoelectric Ceramics In: KNN-based Piezoelectric Ceramics, Piezoelectric and Acoustic Materials for Transducer Applications*. Springer, 2008. URL: https://doi.org/10.1007/978-0-387-76540-2_5.

[52] Angelica Marie Maza Larsen. Potassium sodium niobate as sintered ceramics and aerosol deposited coating for biomedical applications. *NTNU - Institutt for materialteknologi - Master thesis*, 2021. URL: https://hdl.handle.net/11250/2785343.

[53] Ruben Beltrami; Elisa Mercadelli; Carlo Baldisserri; Carmen Galassi; Francesco Braghin; Nora Lecis. Synthesis of knn powders: Scaling effect of the milling step. *Powder Technology*, 375, 2020. URL: https://doi.org/10.1016/j.powtec.2020.07.098.

[54] Y. Li, Y. Liu, P. Ochsner, D. Isaia, and Y. Zhang. Temperature dependent fracture toughness of knn-based lead-free piezoelectric ceramics. *Acta Materialia*, 174, 2019. URL: https://doi.org/10.1016/j.actamat.2019.05.060.

[55] Zongxin Li, Huajun Sun, Xiaofang Liu, Huiting Sui, and Huiling Guo. High performance lead-free $Na_{0.5}K_{0.5}NbO_3$ piezoelectric ceramics obtained via oscillatory hot-pressing. *Ceramics international*, 46, 2020. URL: https://doi.org/10.1016/j.ceramint.2020.01.191.

[56] Hui Liu, Jun Chen, Longlong Fan, Yang Ren, Zhao Pan, K. V. Lalitha, Jürgen Rödel, and Xianran Xing. Critical role of monoclinic polarization rotation in high-performance perovskite piezoelectric materials. *Physical Review Letters*, 119, 2017. URL: https://doi.org/10.1103/PhysRevLett.119.017601.

[57] Jun-Feng Liu, Xiao-Lin Li, and Ya-Dong Li. Synthesis and characterization of nanocrystalline niobates. *Journal of Crystal Growth*, 247, 2003. URL: https://doi.org/10.1016/S0022-0248(02)02015-8.

[58] Xin Liu. *Organic Chemistry I*. Kwantlen Polytechnic University, 2021.

[59] M. Lundberg and M. Sundberg. Studies of phases in the $KNbO_3-Nb_2O_5$ system by high-resolution electron microscopy and x-ray powder diffraction. *Journal of Solid State Chemistry*, 63, 1986. URL: https://doi.org/10.1016/0022-4596(86)90172-6.

[60] Z. Mirzazadeh, Z. Sherafat, and E. Bagherzadeh. Physical and mechanical properties of pvdf/knn composite produced via hot compression molding. *Ceramics International*, 47, 2020. URL: https://doi.org/10.1016/j.ceramint.2020.10.199.

[61] Nilsson, Lidman, Ljungstrom, and Kjellman. Biocompatible material for implants. u.s. patent, U.S. Patent US6526984 B1, 4 March 2003.

[62] W.C. Oliver and G.M. Pharr. An improved technique for determining hardness and elastic modulus using load and displacement sensing indentation experiments. *Journal of Materials Research*, 7(6):1564–1583, 1992. URL: https://doi.org/10.1557/JMR.1992.1564.

[63] O. Ozmen, C. Ozsoy-Keskinbora, and E. Suvaci. Chemical stability of KNbO3, NaNbO_3, and $K_{0.5}Na_{0.5}NbO_3$ in aqueous medium. *Journal of the American Ceramic Society*, 101, 2018. URL: https://doi.org/10.1111/jace.15291.

[64] Peddigari, Mahesh, and Pamu. Raman and dielectric studies on lead free (k 0.5 na 0.5) nbo 3 piezoelectric ceramics. *IOP Conference Series: Materials Science and Engineering*, 73:012141, 02 2015. URL: https://doi.org/10.1088/1757-899X/73/1/012141.

[65] C. Piskin, L Karacasulu, M. Bortolotti, and C. Vakifahmetoglu. Synthesis of potassium–sodium niobate (knn) from NbO_2. *Open Ceramics*, 7, 2021. URL: https://doi.org/10.1016/j.oceram.2021.100159.

[66] P. Pop-Ghe, N. Stock, and E. Quandt. Suppression of abnormal grain growth in k0.5na0.5nbo3: phase transitions and compatibility. *Scientific reports*, 9, 2019. URL: https://doi.org/10.1038/s41598-019-56389-9.

[67] Ehrhardt Proksch. ph in nature, humans and skin. *The Journal of Dermathology*, 45, 2018. URL: https://doi.org/10.1111/1346-8138.14489.

[68] Ramajo, Leandro, Taub, Jonathan, Castro, and Miriam M. Effect of zno addition on the structure, microstructure and dielectric and piezoelectric

properties of $K_{0.5}Na_{0.5}NbO_3$ ceramics. *Materials Research*, 17:728–733, 05 2014. URL: https://doi.org/10.1590/S1516-14392014005000048.

[69] L. Ramajo, M. Castro, J. F. Fernandez, and F. Rubio-Marcos. Mechanical properties enhancement in potassium-sodium niobate lead-free piezoceramics: the impact of chemical modifications. *Journal of Materials Science: Materials in Electronics*, 28, 2017. URL: https://doi.org/10.1007/s10854-016-6168-8.

[70] R. Rani, S. Sharma, M. Quaglio, and R. Rai et al. A novel low temperature synthesis of knn nanoparticles by facile wet chemical method. *Materials Sciences and Applications*, 8, 2017. URL: https://doi.org/10.4236/msa.2017.83017.

[71] X ray Diffraction and Bragg's Law. PolymerWorld. https://www.youtube.com/watch?v=4e8EB1jzHIQ&ab_channel=PolymerWorld. Last accessed on 25-04-2022.

[72] B. Reddi. Why is saline so acidic (and does it really matter?). *International journal of medical sciences*, 10:747–50, 04 2013. URL: https://doi.org/10.7150/ijms.5868.

[73] Data Bridge Market Research. Global orthopedic implants market – industry trends and forecast to 2029, 2022. Last accessed on 05-05-2022. URL: https://www.databridgemarketresearch.com/reports/global-orthopedic-implants-market.

[74] M Rotan, M Zhuk, and J Glaum. Activation of ferroelectric implant ceramics by corona discharge poling. *Journal of the European Ceramic Society*, 40, 2020. URL: https://doi.org/10.1016/j.jeurceramsoc.2020.06.058.

[75] Nilofar Asim; Shideh Ahmadi; Alghoul;Y. Hammadi; Kasra Saeedfar; and K. Sopian. Research and development aspects on chemical preparation techniques of photoanodes for dye sensitized solar cell. *International Journal of Photoenerg*, 2014. URL: https://doi.org/10.1155/2014/518156.

[76] Osman Sahin, Orhan Uzun, Ugur Kolemen, and Nebahattin Ucar. Dynamic hardness and reduced modulus determination on the (001) face of β-sn single crystals by a depth sensing indentation technique. *Journal of Physics: Condensed Matter*, 19:306001, 07 2007. URL: https://doi.org/10.1088/0953-8984/19/30/306001.

[77] C. Schuh. Nanoindentation studies of materials. *Materials Today*, 9(5), 2006. URL: https://doi.org/10.1016/S1369-7021(06)71495-X.

[78] M. Shamos and L. Lavine. Piezoelectricity as a fundamental property of biological tissues. *Nature*, 213, 1967. URL: https://doi.org/10.1038/213267a0.

[79] R. Martin; D. Burr; N. Sharkey and D. Fyhrie. *Functional Musculoskeletal Anatomy In: Skeletal Tissue Mechanics*. Springer, 2015. Second edition.

[80] R. Martin; D. Burr; N. Sharkey and D. Fyhrie. *Skeletal Biology In: Skeletal Tissue Mechanics*. Springer, 2015. Second edition.

[81] C. Shi, J. Ma, J. Wu, and X. Wang et al. Coexistence of excellent piezoelectric performance and high curie temperature in knn-based lead-free piezoelectric ceramics. *Journal of Alloys and Compounds*, 846, 2020. URL: https://doi.org/10.1016/j.jallcom.2020.156245.

[82] T. Shrout and S. Zhang. Lead-free piezoelectric ceramics: Alternatives for pzt? *J Electroceram*, 19(185), 2007. URL: https://doi.org/10.1007/s10832-007-9095-5.

[83] V. Saxena; I. Shukla and L. Pandey. Hydroxyapatite: an inorganic ceramic for biomedical applications. *Materials for Biomedical Engineering*, 2019. URL: https://doi.org/10.1016/B978-0-12-816909-4.00008-7.

[84] S.Hulbert, L.Hench, D.Forbers, and L.Bowman. History of bioceramics. *Ceramics international*, 8, 1982. URL: https://doi.org/10.1016/0272-8842(82)90003-7.

[85] D. Shuman, A. Costa, and M. Andrade. Calculating the elastic modulus from nanoindentation and microindentation reload curves. *Materials Characterization*, 58, 2007. URL: https://doi.org/10.1016/j.matchar.2006.06.005.

[86] X. Su, Z. Jiao, M. Fu, G. An, and Y. Wu et al. Ultrafast synthesis and densification of zro2 doped knn ceramics by reactive flash sintering. *International journal of applied ceramic technology*, 18, 2021. URL: https://doi.org/10.1111/ijac.13820.

[87] Solid State Synthesis. https://www.sigmaaldrich.com/NO/en/applications/materials-science-and-engineering/solid-state-synthesis. Last accessed on 21-04-2022.

[88] The piezoelectric effect. https://www.nanomotion.com/nanomotion-technology/piezoelectric-effect/. Last accessed on 29-03-2022.

[89] K. Torres-Rivero, J.Bastos-Arrieta, N. Fiol, and A. Florido. *Chapter Ten - Metal and metal oxide nanoparticles: An integrated perspective of the green synthesis methods by natural products and waste valorization: applications and challenges*, volume 94, pages 433–469. Sandeep Kumar Verma, Ashok Kumar Das Comprehensive Analytical Chemistry, Elsevier, 2021. URL: https://doi.org/10.1016/bs.coac.2020.12.001.

[90] Vickers Hardness Test: What it is and how it's measured. `https://matmatch.com/learn/property/vickers-hardness-test`. Last accessed on 18-03-2022.

[91] H. Wang and A. Jasim. 14 - piezoelectric energy harvesting from pavement. *In Woodhead Publishing Series in Civil and Structural Engineering,Eco-Efficient Pavement Construction Materials*, 2020. URL: `https://doi.org/10.1016/B978-0-12-818981-8.00014-X`.

[92] RR.K. Fuchs; S.J. Warden and C.H. Turner. *2 - Bone anatomy, physiology and adaptation to mechanical loading*. In Woodhead Publishing Series in Biomaterials; Bone Repair Biomaterials; Woodhead Publishing, 2009. URL: `https://doi.org/10.1533/9781845696610.1.25`.

[93] What is Piezoelectricity? `https://onscale.com/piezoelectricity/what-is-piezoelectricity/`. Last accessed on 29-03-2022.

[94] E. Yilmaz, H. Mgbemere, H. Özcoban, R. Fernandes, and G. Schneider. Investigation of fracture toughness of modified $(KxNa_{1-x})NbO_3$ lead-free piezoelectric ceramics. *Journal of the European Ceramic Society*, 32, 2012. URL: `https://doi.org/10.1016/j.jeurceramsoc.2012.04.005`.

[95] S. Yu, S. Kuo, W. Tuan, Y.Tsai, and C. Su. Ion release from three lead-free piezoelectric ceramics and their physical and cytotoxicity characteristics. *Materials letters*, 65, 2011. URL: `https://doi.org/10.1016/j.matlet.2011.07.098`.

[96] SW. Yu, ST. Kuo, WH. Tuan, YY. Tsai, and SF. Wang. Cytotoxicity and degradation behavior of potassium sodium niobate piezoelectric ceramics. *Ceramics International*, 38, 2012. URL: `https://doi.org/10.1016/j.ceramint.2011.11.056`.

[97] Y. Zhai, Y. Feng, J. Du, J. Xue1, and J. Shen et al. The impedance, dielectric and piezoelectric properties of Tb_4O_7 and Tm_2O_3 doped knn ceramics. *Journal of Materials Science: Materials in Electronics*, 30, 2019. URL: `https://doi.org/10.1007/s10854-019-00748-9`.

[98] M. Zheng, Y. Hou, X. Yan, L. Zhang, and M. Zhu. A highly dense structure boosts energy harvesting and cycling reliabilities of a high-performance lead-free energy harvester. *Journal of Materials Chemistry C*, 5, 2017. URL: `https://doi.org/10.1039/c7tc00914c`.

[99] T. Zheng, H. Wu, Y. Yuan, Q. Li, T. Men, and C. Zhao et al. The structural origin of enhanced piezoelectric performance and stability in lead free ceramics. *Energy and Environmental Science*, 10, 2017. URL: `https://doi.org/10.1039/C6EE03597C`.

[100] H. Zhou, S. Lu, and D. Dempster. *2 - Bone anatomy, physiology and adaptation to mechanical loading.* IN Osteoporosis in Men (Second Edition),Academic Press, 2009. URL: https://doi.org/10.1016/B978-0-12-374602-3.00002-X.

[101] H. Wang; L. Zhu and B. Xu. *Principle and Methods of Nanoindentation Test In: Residual Stresses and Nanoindentation Testing of Films and Coatings.* Springer, Singapore, 2018.

APPENDIX

A Precursor used

Chemicals	In batch a (g)	In batch b (g)	In batch c (g)
Na_2CO_3	2.3114	2.3119	2.3117
K_2CO_3	3.0145	3.0152	3.0147
Nb_2O_5	11.5938	11.5938	11.5934

Table 1: Amount of precursor used for the three different batches.

B Geometrical measurement of the samples

	Mass [g]	Diameter [mm]	Thickness [mm]
a-04	0.2307	8.04	1.13
		8.04	1.12
		8.01	1.09
		8.01	1.10
a-05	0.2305	8.05	1.07
		8.09	1.05
		8.07	1.12
		8.09	1.05
a-06	0.2292	8.14	1.03
		8.15	1.05
		8.15	1.04
		8.16	1.05
a-07	0.2483	8.15	1.13
		8.12	1.14
		8.15	1.13
		8.12	1.13
		Continued on next page …	

	Mass [g]	Diameter [mm]	Thickness [mm]
		...continued from previous page	
a-08	0.2569	8.05	1.18
		8.09	1.18
		8.07	1.19
		8.10	1.18
a-09	0.2529	8.05	1.18
		8.06	1.25
		8.07	1.24
		8.10	1.24
a-10	0.2375	8.05	1.10
		8.06	1.10
		8.05	1.11
		8.03	1.13
a-11	0.2394	8.00	1.07
		8.02	1.04
		8.07	1.08
		8.06	1.09
a-12	0.2183	8.10	1.02
		8.03	1.04
		8.03	1.03
		7.97	0.99
a-13	0.2537	8.12	1.20
		8.16	1.18
		8.14	1.13
		8.12	1.13
a-14	0.2182	8.01	1.00
		8.06	1.05
		8.04	1.03
		8.06	1.05
b-02	0.2572	8.05	1.20
		8.08	1.20
		8.10	1.17
		8.05	1.15
b-03	0.2472	8.09	1.13
		8.14	1.10
		8.06	1.12
		8.11	1.12
		Continued on next page ...	

	Mass [g]	Diameter [mm]	Thickness [mm]
		. . . continued from previous page	
b-04	0.2535	8.04	1.22
		8.07	1.24
		8.08	1.18
		8.09	1.18
b-05	0.2553	8.26	1.17
		8.06	1.18
		8.14	1.19
		8.06	1.22
b-06	0.2606	8.04	1.16
		8.07	1.18
		8.06	1.19
		8.10	1.21
b-07	0.2571	8.01	1.23
		8.01	1.23
		8.04	1.26
		8.03	1.23
b-08	0.2580	8.00	1.23
		8.03	1.22
		8.05	1.24
		8.08	1.30
b-10	0.2614	8.00	1.21
		8.01	1.22
		8.03	1.25
		8.05	1.27
b-11	0.2420	8.07	1.12
		8.13	1.13
		8.14	1.14
		8.18	1.16
b-12	0.2684	8.01	1.25
		8.04	1.30
		8.05	1.26
		8.05	1.33
c-01	0.2350	7.89	1.13
		7.90	1.09
		7.87	1.11
		7.90	1.12
		Continued on next page . . .	

	Mass [g]	Diameter [mm]	Thickness [mm]
c-02	0.2220	7.85	1.03
		7.93	1.09
		7.85	1.11
		7.90	1.06
c-03	0.2168	7.94	1.02
		7.96	1.02
		7.96	1.02
		7.96	1.05
c-04	0.2455	7.88	1.12
		7.89	1.11
		7.89	1.16
		7.91	1.15
c-05	0.2364	7.88	1.10
		7.83	1.07
		7.88	1.11
		7.90	1.11
c-06	0.2475	7.88	1.14
		7.90	1.17
		7.95	1.13
		7.90	1.15
c-07	0.2449	7.87	1.12
		7.95	1.13
		8.00	1.15
		7.96	1.12
c-08	0.2257	7.89	1.08
		7.90	1.06
		7.88	1.11
		7.92	1.03
c-09	0.2196	7.89	1.03
		7.90	1.06
		7.88	1.02
		7.80	1.02
c-10	0.2212	7.85	1.03
		7.93	1.12
		7.86	1.10
		7.87	0.96

...continued from previous page

Continued on next page ...

	Mass [g]	Diameter [mm]	Thickness [mm]
		...continued from previous page	
c-11	0.2091	7.94	1.01
		7.91	1.04
		7.99	1.02
		8.00	1.04
c-12	0.2121	7.94	1.00
		7.97	1.01
		7.99	1.02
		8.03	0.99

Table 2: Geometrical measurement of all the samples

C   Raman

C.1   Before soaking
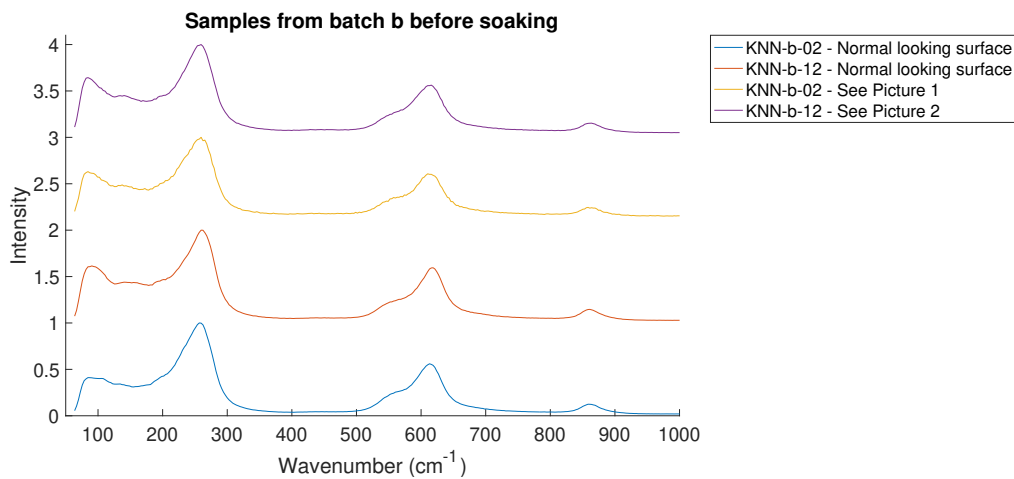
(a) Raman spectroscopy
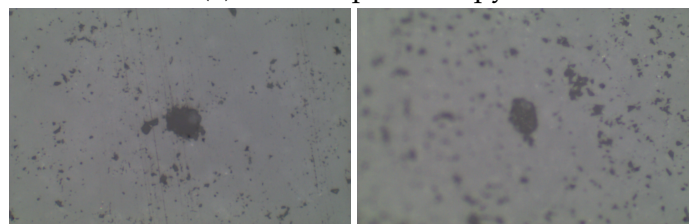
(b) Picture 1   (c) Picture 2

Figure 1: Raman spectroscopy on two samples from batch b and the corresponding pictures of the surface.

(a) Raman spectroscopy
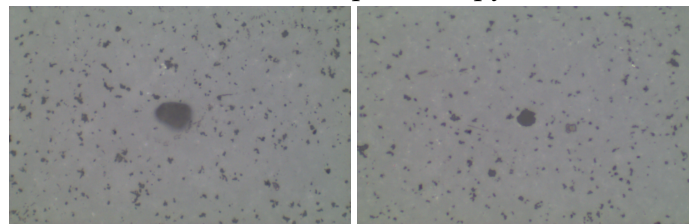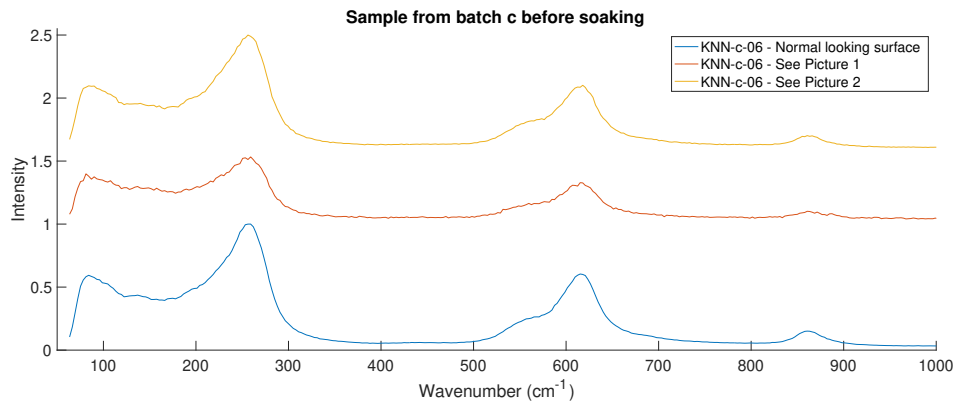
(b) Picture 1   (c) Picture 2

Figure 2: Raman spectroscopy on one sample from batch c and the corresponding pictures of the surface

D   Nanoindentation

D.1   KNN-a-06

One curve taken on a black spot isn't displayed as the displacement during measurement exceeded the limit of 5000nm.
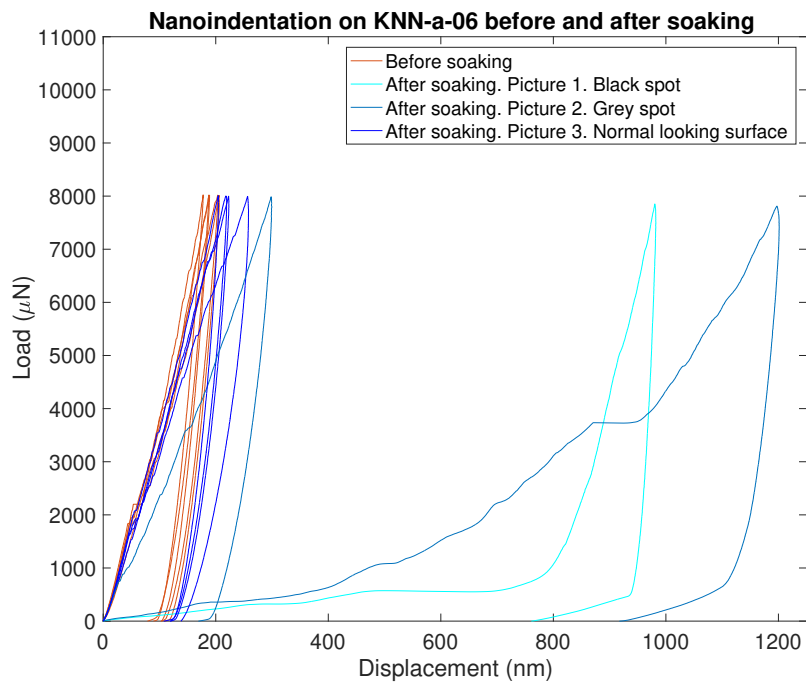
(a) Nanoindendation curves
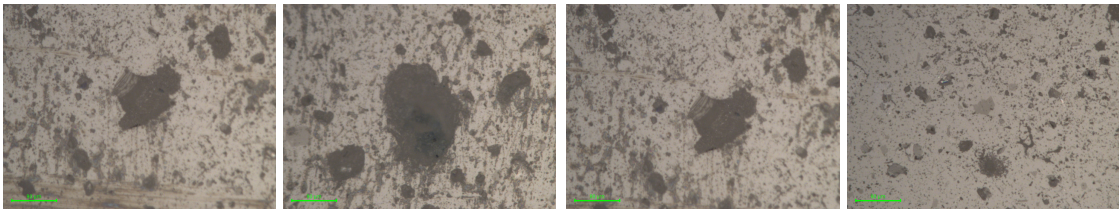
(b) Black spots. Picture 1   (c) Gray spots. Picture 2
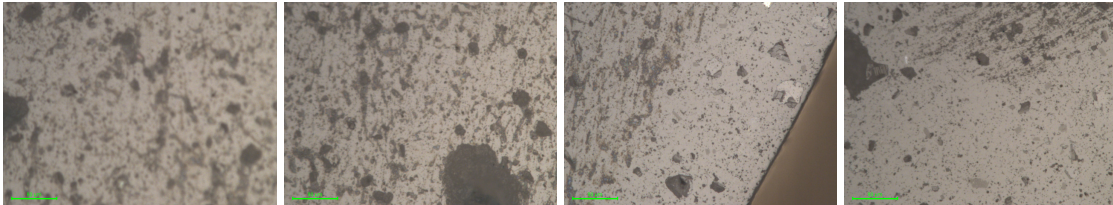
(d) Normal looking surface spot. Picture 3

Figure 3: Nanoindentation on a sample soaked for 12h in ultra-pure water and the corresponding pictures of the surface.

D.2 KNN-a-07

Nanoindentation on KNN-a-07
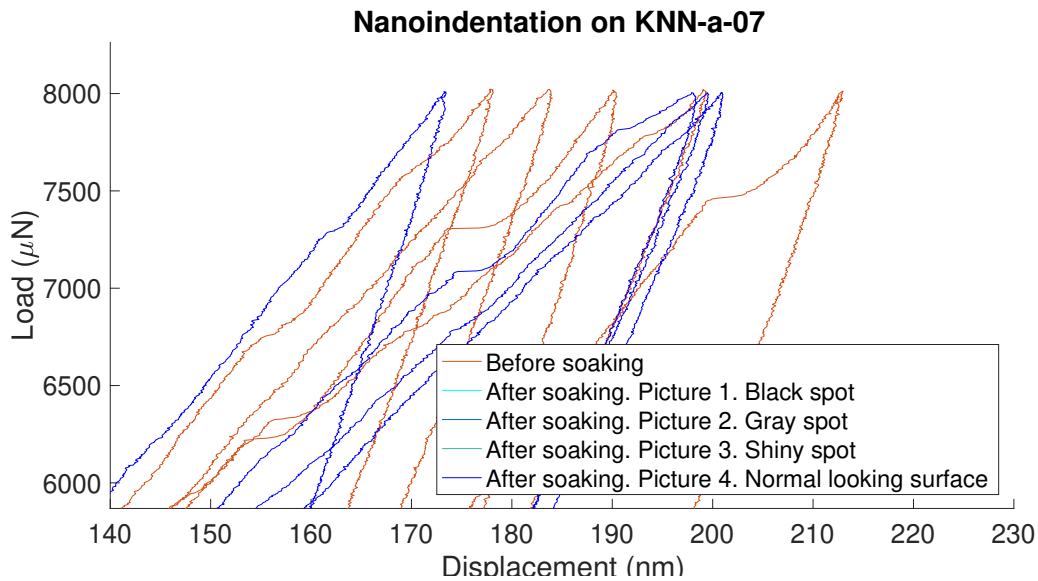
Figure 4: Nanoindentation on KNN-a-07 before and after soaking. Zoom from Figure 4.19a.

D.3 KNN-a-08

Nanoindentation on KNN-a-08 before and after soaking
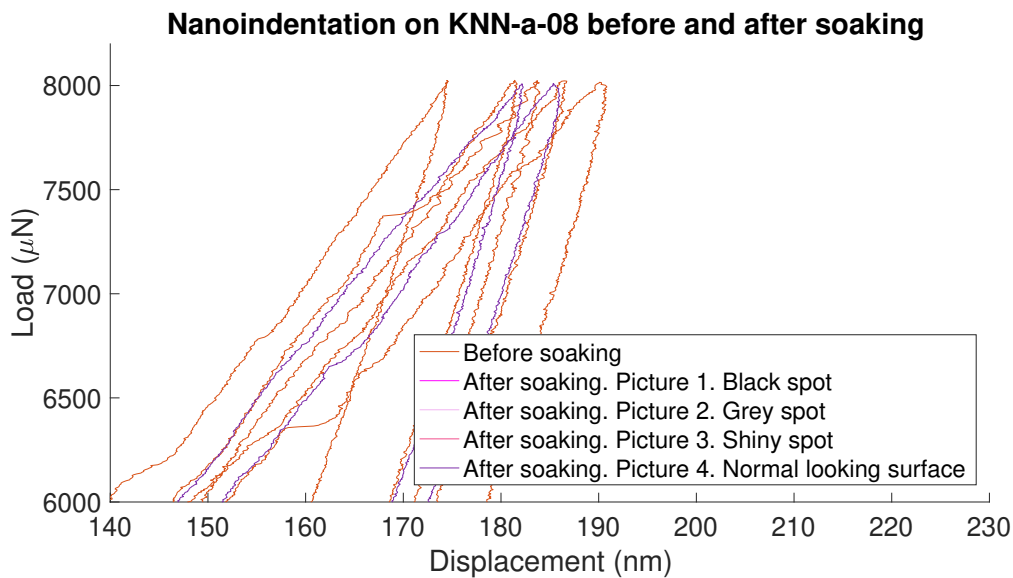
Figure 5: Nanoindentation on KNN-a-08 before and after soaking. Zoom from Figure 4.21a.

D.4 KNN-a-09

(a) Nanoindendation curves.
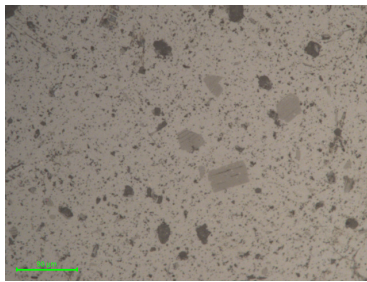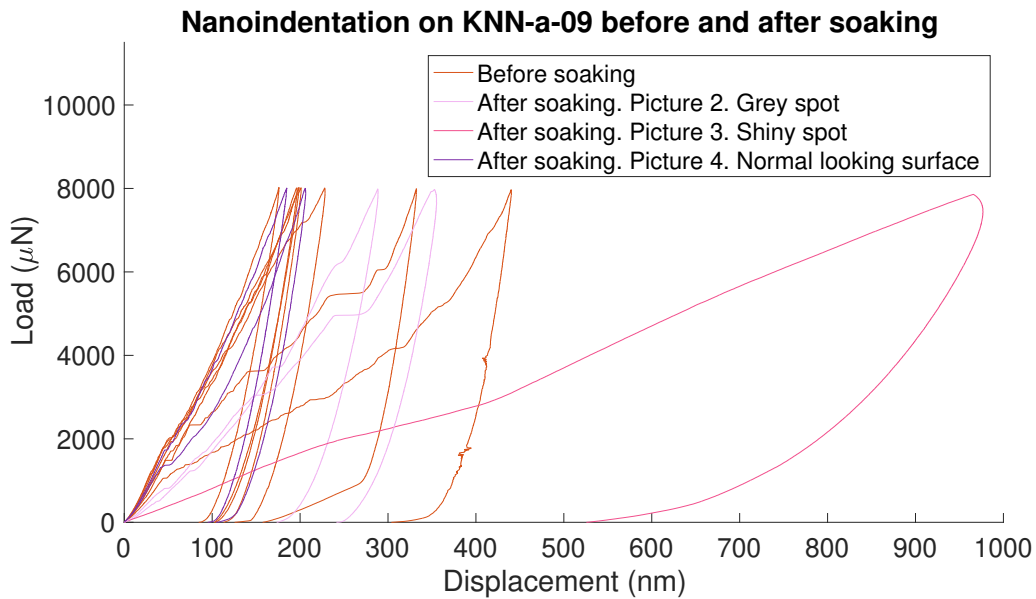
(b) Grey spots. Picture 2
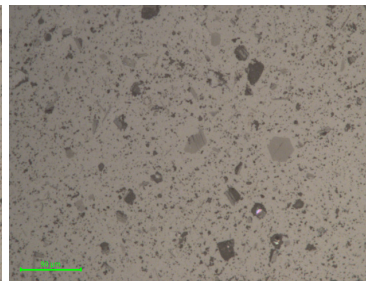
(c) Shiny spots. Picture 3.
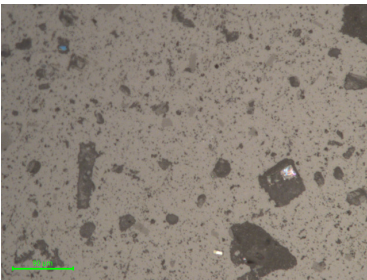
(d) Normal looking surface. Picture 3

Figure 6: Nanoindentation on a sample soaked for 12h in deionized water and the corresponding pictures of the surface. The indent was taken in the middle of the picture.
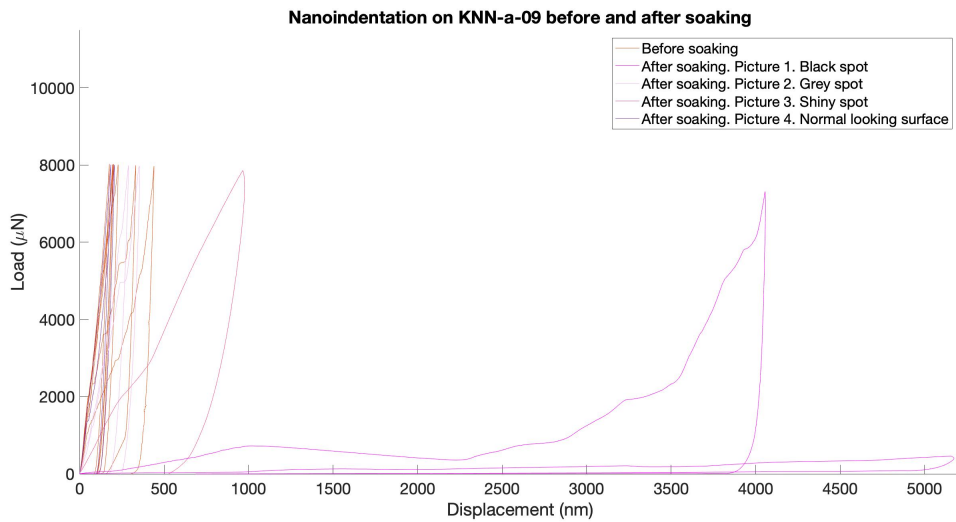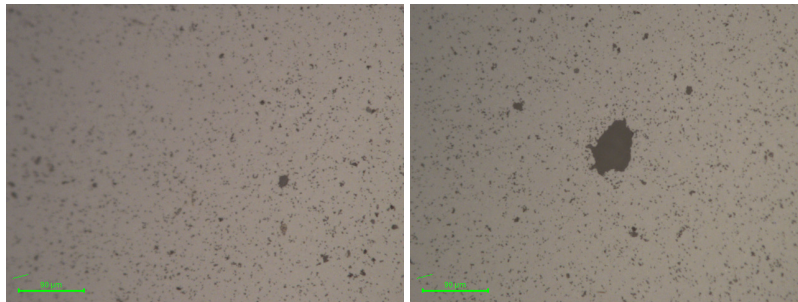
(a) Nanoindendation curves. A zoom out of Figure 6a
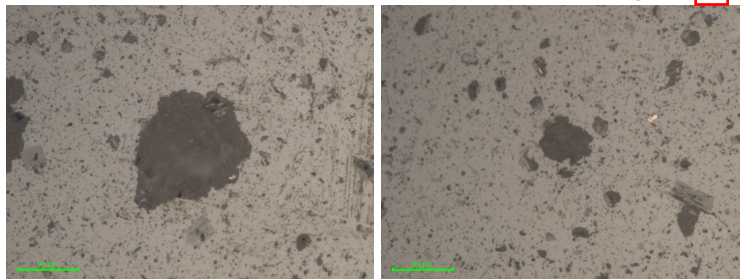

(b) Black spots. Picture 1

Figure 7: Nanoindentation on a sample soaked for 12h in Deionized water and the corresponding pictures of the surface. The indent was taken in the middle of the picture.

D.5 KNN-a-11
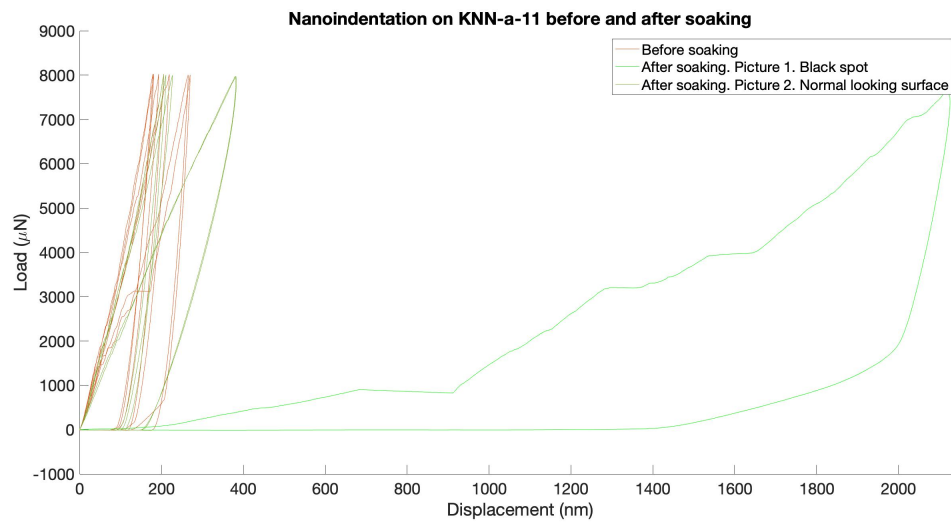
(a) Nanoindendation curves.
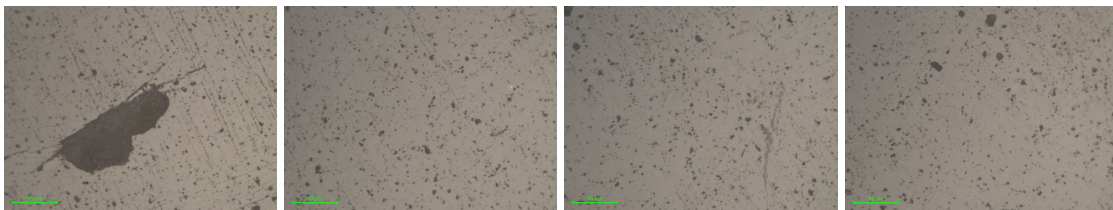
(b) Black spot. Pic1   (c) Normal looking surface. Picture 2

Figure 8: Nanoindentation on a sample soaked for 12h in Saline solution and the corresponding pictures of the surface.

D.6   KNN-b-07
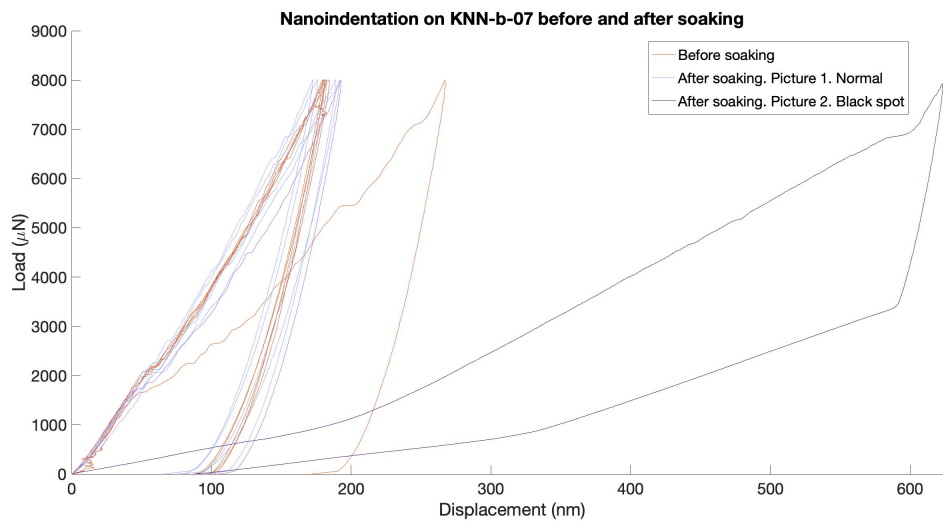
Figure 9: Nanoindendation on a sample soaked for 24h in saline solution.

D.7 KNN-b-08
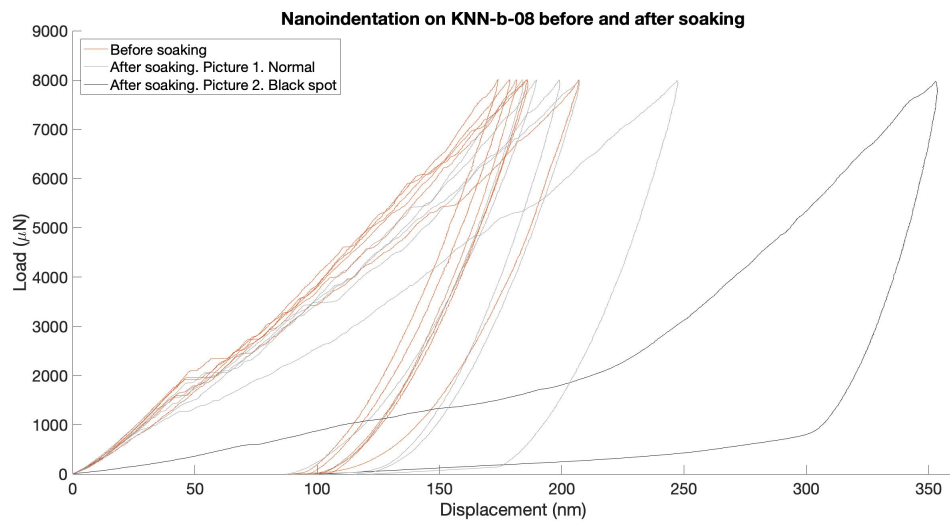
(a) Nanoindendation curves.
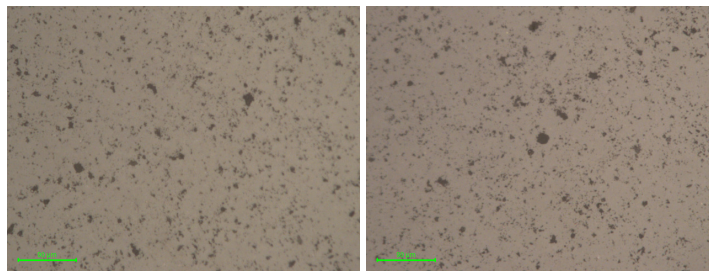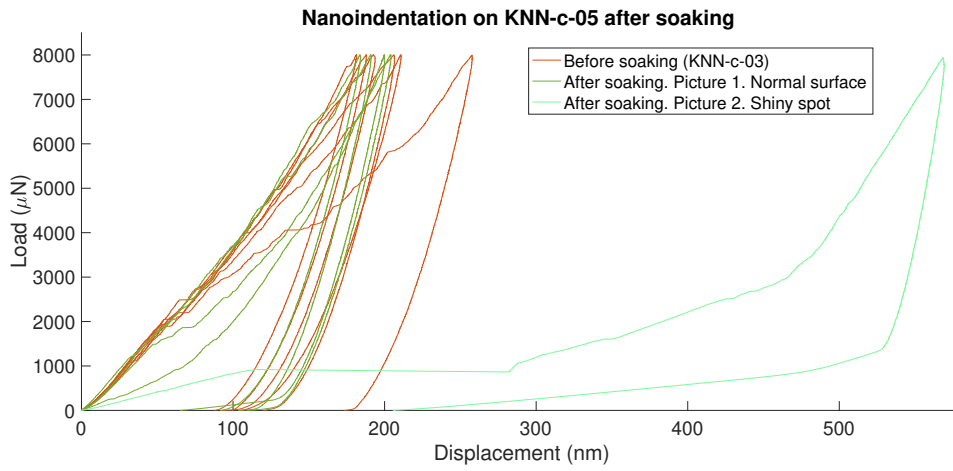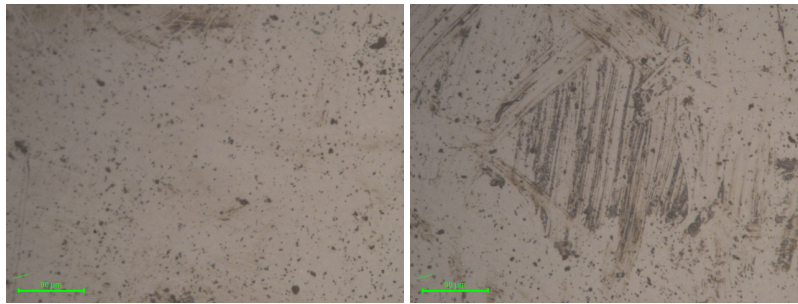

(b) Normal surface. Pic 1   (c) Black spot. Pic 2

Figure 10: Nanoindentation on a sample soaked for 6h in Saline solution and the corresponding pictures of the surface.

D.8 KNN-b-11
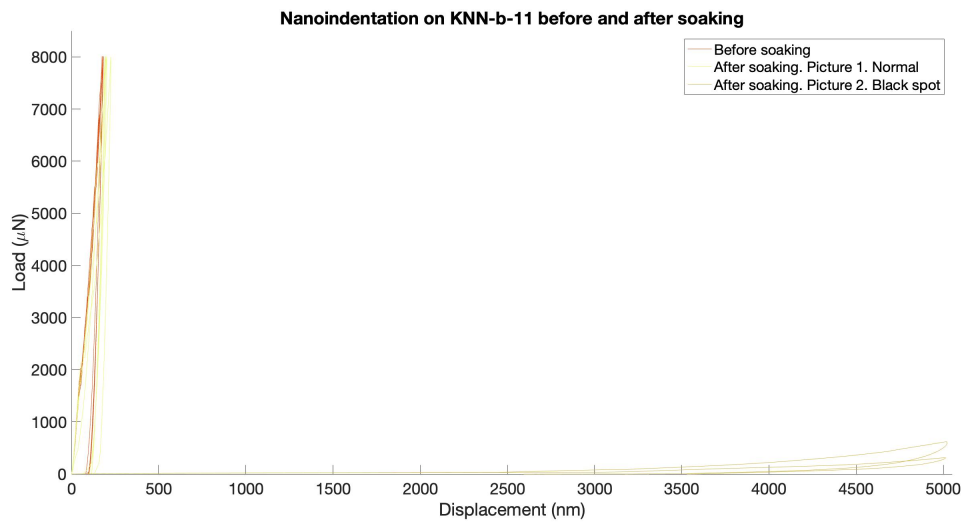
Figure 11: Nanoindendation on a sample soaked for 72h in saline solution.

D.9 KNN-c-02
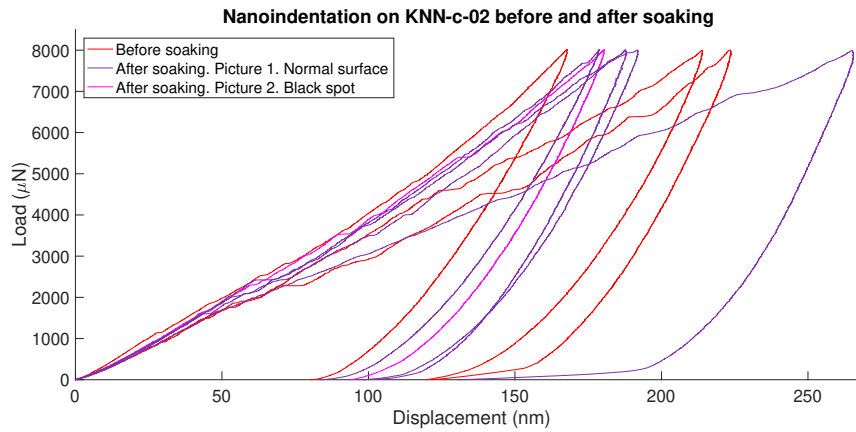
(a) Nanoindendation curves.

(b) Normal looking surface. Picture 1

(c) Black spot. Picture 2.

Figure 12: Nanoindentation on a sample soaked for 12h in deionized water and the corresponding pictures of the surface.

D.10 KNN-c-04
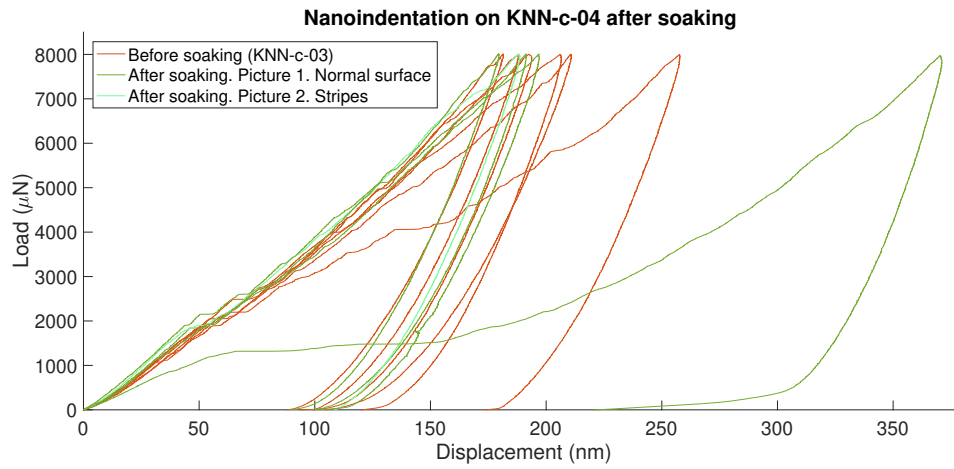
(a) Nanoindendation curves.
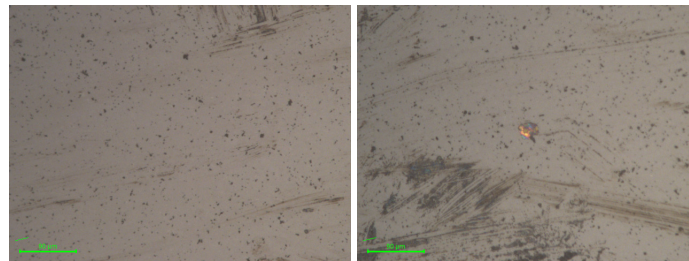
(b) Normal surface. Picture 1

(c) Shiny spot. Picture 2

Figure 13: Nanoindentation on a sample soaked for 12h in saline solution and the corresponding pictures of the surface.
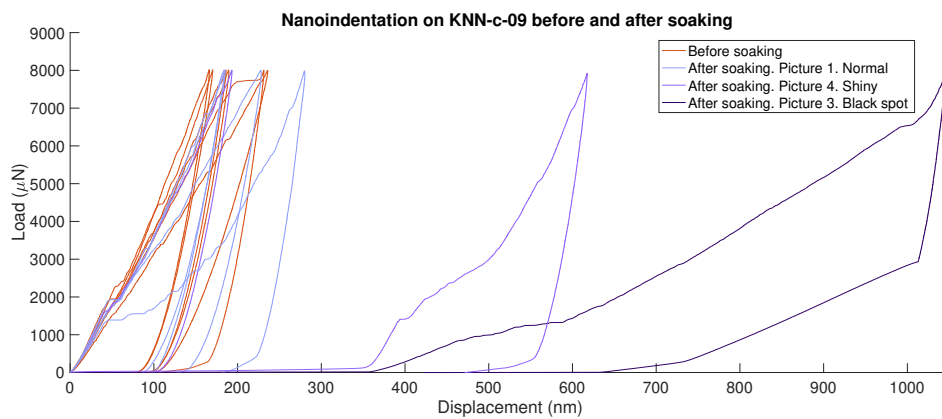
D.11   KNN-c-05

(a) Nanoindendation curves.

(b) Normal surface. Picture 1

(c) Stripes. Picture 2

Figure 14: Nanoindentation on a sample soaked for 12h in saline solution and the corresponding pictures of the surface.

D.12   KNN-c-09

Figure 15: Nanoindendation on a sample soaked for 24h in saline solution.
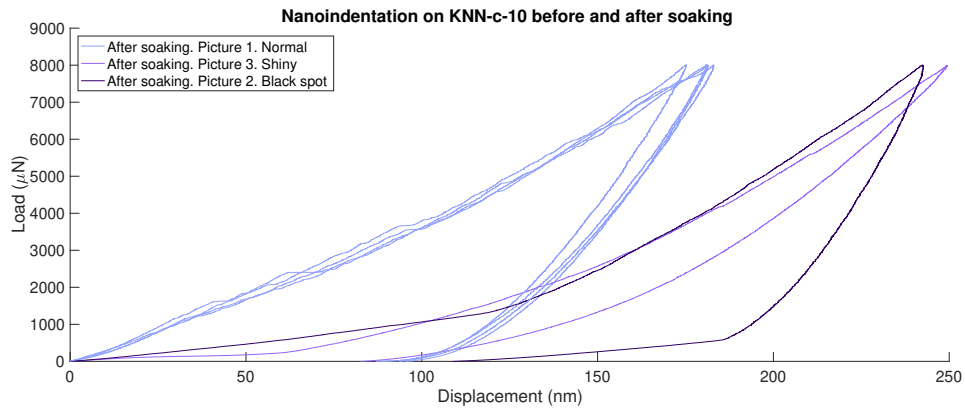
D.13 KNN-c-10

Figure 16: Nanoindendation on a sample soaked for 24h in saline solution.

D.14 KNN-c-11

Due to technical difficulties, nanoindentation could not be performed on this sample before soaking.
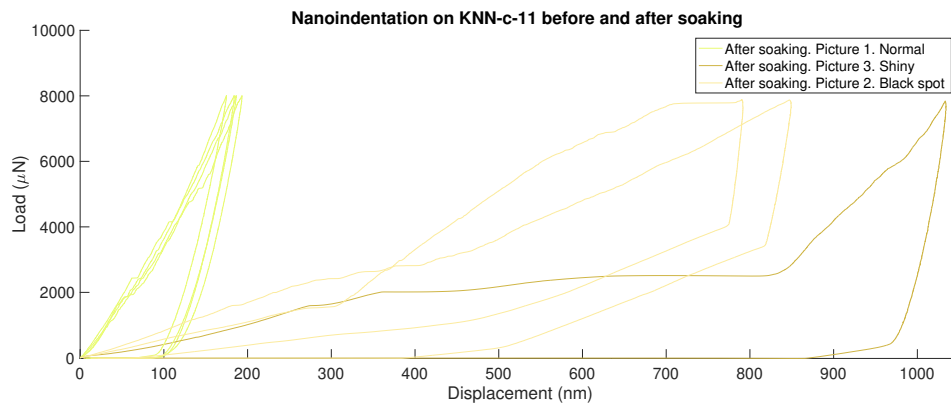

Figure 17: Nanoindendation on a sample soaked for 72h in saline solution.

D.15   KNN-c-12

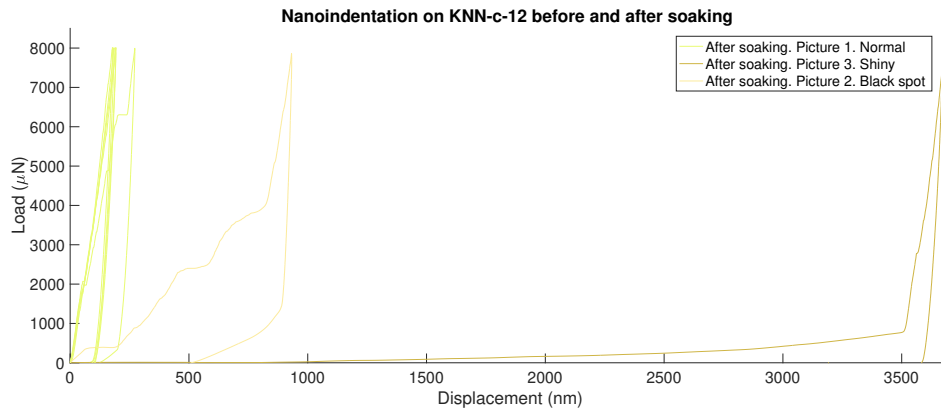Due to technical difficulties, nanoindentation could not be performed on this sample before soaking.

Figure 18: Nanoindendation on a sample soaked for 72h in saline solution.

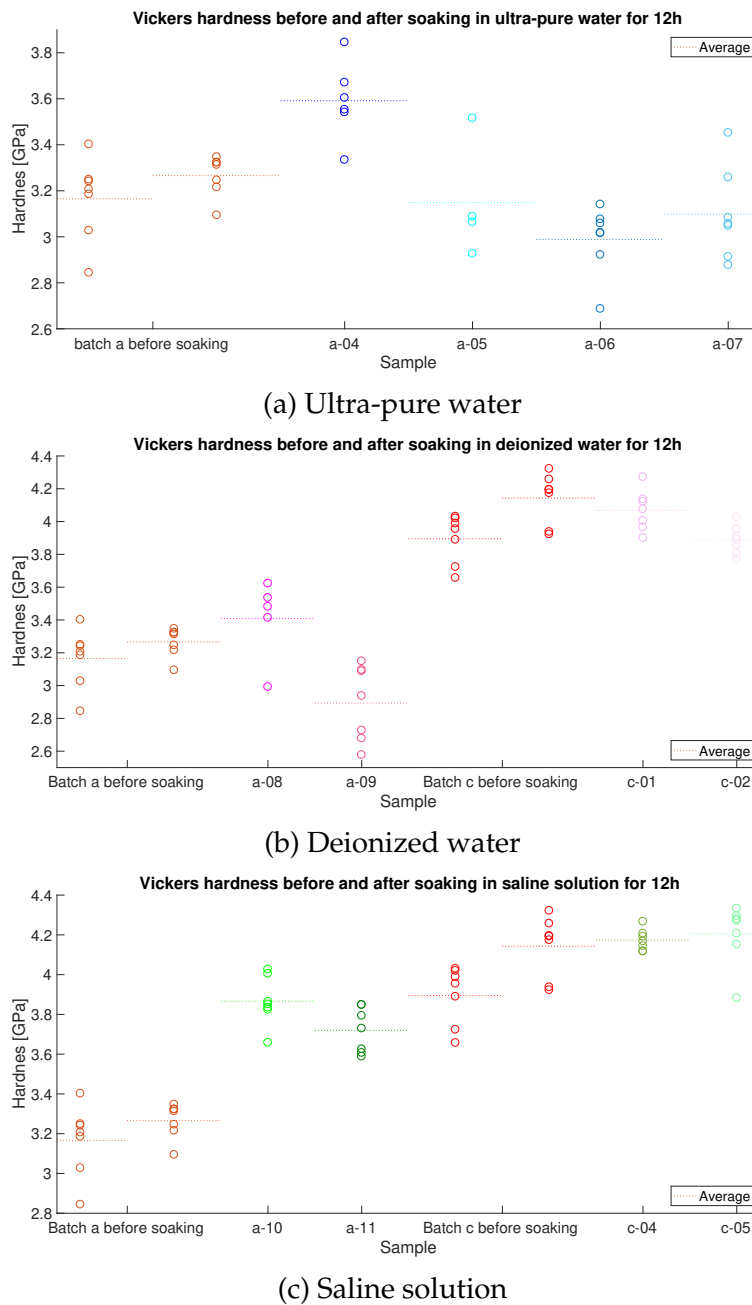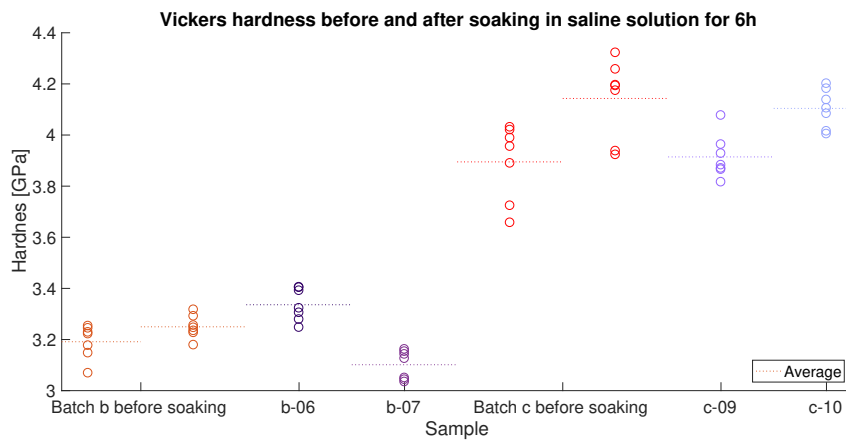# E Microindentation

E.1 Soaking 12h in different liquids

(a) Ultra-pure water

(b) Deionized water

(c) Saline solution

Figure 19: Vickers hardness obtained on different samples, before and after soaking for 12h in different solutions

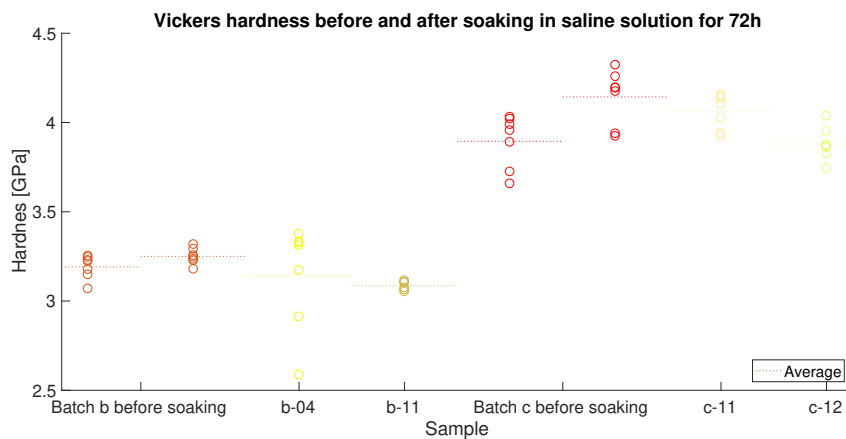NTNU | Norwegian University of Science and Technology

E.2 Soaking in saline solution for different times

(a) 6h in saline solution

(b) 24h in saline solution

(c) 72h in saline solution

Figure 20: Vickers hardness obtained on different samples, before and after soaking in saline solution for different times